DISSERTATION

CHARACTERISTICS OF SUMMERTIME MICROWAVE LAND EMISSIVITY OVER THE CONTERMINOUS UNITED STATES

Submitted by
Benjamin C. Ruston
Department of Atmospheric Science

In partial fulfillment of the requirements
for the Degree of Doctor of Philosophy
Colorado State University
Fort Collins, Colorado
Spring 2004

COLORADO STATE UNIVERSITY

December 10, 2003

WE HEREBY RECOMMEND THAT THE DISSERTATION PREPARED UNDER OUR SUPERVISION BY BENJAMIN C. RUSTON ENTITLED CHARACTERISTICS OF SUMMERTIME MICROWAVE LAND EMISSIVITY OVER THE CONTERMINOUS UNITED STATES BE ACCEPTED AS FULFILLING IN PART REQUIREMENTS FOR THE DEGREE OF DOCTOR OF PHILOSOPHY

Committee on Graduate Work

Andrew S Jones

Charles W Anderson

Thomas H Vonder Haar

Adviser

Department Head

ABSTRACT OF DISSERTATION

CHARACTERISTICS OF SUMMERTIME MICROWAVE LAND EMISSIVITY OVER THE CONTERMINOUS UNITED STATES

This study examines the microwave land emissivity, a key value that can be derived from microwave measurements. At microwave frequencies the atmosphere is semi-transparent. Consequently, a satellite radiance measurement contains a large fraction of energy from the Earth's surface. Microwave radiometers have been in space beginning in the early 1970s, and have shown great utility in retrieving atmospheric variables such as total precipitable water, cloud liquid water, and rain over the ocean where the emissivity is well known. These retrievals cannot be performed over land, due to the poor characterization of the underlying land surface; specifically the land surface temperature and surface emissivity. This research characterizes microwave surface emissivity and its associated error over the summertime Conterminous United States (CONUS) during 2000 – 2002 for use with various remote sensing applications and data assimilation systems. It is found that the microwave emissivity errors are dominated by the error in the land surface temperature. The microwave emissivity error is generally better than two percent within a natural summertime variability of five percent.

Benjamin C. Ruston
Department of Atmospheric Science
Colorado State University
Fort Collins, Colorado 80523
Spring 2004

ACKNOWLEDGMENTS

I would like to thank my advisor, Prof. Tom Vonder Haar, and committee members Profs. Graeme Stephens, Christian Kummerow, Charles Anderson, and Dr. Andrew Jones; their time and insight have been invaluable. I would also like to thank the Vonder Haar research group, John Forsythe, Dr. Stanley Kidder, Dr. Philip Gabriel and the Stephens group for help and mentorship in optimal estimation methods, and my family for their unending support. This research was supported by the DoD Center for Geosciences/Atmospheric Research at Colorado State University under Cooperative Agreements DAAL01-98-2-0078, DAAD19-01-2-0018 and DAAD19-02-2-0005 with the Army Research Laboratory, and by the National Oceanic and Atmospheric Association under grant NA17RJ1228.

Table of Contents

1. Introduction

Microwave radiation is emitted from the atmosphere and the surface. The atmospheric contribution is from gases, clouds, and precipitation particles. The atmospheric transmission has been derived and related to atmospheric parameters such as total precipitable water, cloud liquid water, and rain rate. To retrieve the atmospheric parameters from a satellite measurement the emission from the surface must be removed. The surface contribution varies depending on the water fraction, vegetation type and water content, and soil type and wetness. The microwave radiation emitted by ocean surfaces can be approximated using factors assumed spatially homogenous over the satellite footprint, namely the temperature, salinity, and wind speed. The highly spatially variant vegetation, soil, water bodies, agricultural areas, and urban areas complicate the modeling of land surface microwave emission. Atmospheric retrievals over land are further complicated by the strong microwave emission typical over land. This strong emission dominates the satellite measurement, leaving a smaller fraction from the atmosphere.

Due to the smaller atmospheric signal over land prior estimates of the atmospheric state are desirable for a robust atmospheric retrieval. A variational approach to an atmospheric retrieval utilizes probability distributions of all atmospheric parameters and surface emissivity. The land surface emissivity characterization necessary for a variational retrieval includes a typical value, its variability, and its error. If the characterization of the emissivity is robust a variational retrieval can provide an estimate of a new atmospheric state and its potential error. However, the microwave emissivity over land has not been well characterized. This dissertation addresses this problem by using an observational approach to retrieve the microwave land emissivity over the summertime Conterminous United States (CONUS). A variational retrieval is used to investigate the sensitivity of the atmospheric profile to the retrieved land emissivities. It is found that microwave land surface emissivity has the strongest impacts on temperature and moisture profiles near the surface. This chapter presents the reader with some basic physics used to describe the land emissivity problem. Examples of prior research are used to illustrate how microwave radiometry is used to retrieve atmospheric and surface parameters.

1.1 Background

Max Planck (1900) formulated Equation 1.1, describing the intensity radiated by a blackbody as a function of wavelength,

$$\beta_\lambda(T) = \frac{2hc^2\lambda^{-5}}{\exp\left(\frac{hc}{\lambda k_B T}\right) - 1} \; .$$

$$\begin{gathered} h = \text{Planck's Constant: } 6.626 \times 10^{-34}\ \text{J s} \\ c = \text{Speed of Light: } 2.9979 \times 10^{8}\ \text{m s}^{-1} \\ k_B = \text{Boltzmann constant: } 1.38 \times 10^{-23}\ \text{J K}^{-1} \end{gathered} \tag{1.1}$$

However, no surface radiates as a perfect blackbody. The spectral emissivity (ε_λ) is a measure of the radiance emitted by a body compared to a blackbody for a given wavelength. The emissivity ranges from 0 to near 1 for all surfaces (ground and cloud). It is the emissivity that then determines the final amount of radiation, $L_\lambda(T)$, emanating from a body as shown in Equation 1.2,

$$L_\lambda(T) = \varepsilon_\lambda \beta_\lambda(T) \; . \tag{1.2}$$

Though the emissivity, ε_λ, in Equation 1.2 is shown only as a function of wavelength, it is also dependent on temperature and viewing geometry. For the land surface temperatures typical of Earth, this temperature dependence is very small. The emissivity also varies with the zenith and azimuth angle. In our study, only the zenith dependence will be directly addressed. A strong regional dependence on azimuth angle will add to the variability of the microwave emissivity of that region.

The surface emissivity may be used to simulate the brightness temperatures derived from microwave satellite observations. A cloud free atmosphere is assumed to be non-scattering, and only gaseous absorption/emission is considered. A simplified expression for plane-parallel microwave radiative transfer includes three terms: the emission from the surface, the emission upward from the atmosphere, and the downward atmospheric emission reflected by the surface and transmitted through the atmosphere,

$$T_B = \varepsilon T_S e^{-\tau_A} + (1-\varepsilon)e^{-\tau_A} T_D + T_U . \tag{1.3}$$

In Equation 1.3, the brightness temperature measured by the satellite, T_B, is given by the emissivity of the surface, ε, multiplied by the surface temperature, T_S, which is then multiplied by the atmospheric transmittance, $e^{-\tau_A}$. Due to the conservation of energy, the sum of the transmissivity, reflectivity, and emissivity of the surface must be equal to unity. If the transmission of microwave radiation at the surface is neglected, the surface reflectivity is given by 1 - ε. The second term on the right hand side is the downwelling atmospheric emission reflected off the surface and retransmitted through the atmosphere. The final term is the upwelling atmospheric emission. This equation demonstrates that the microwave brightness temperature contains imbedded information from the atmospheric temperature profile, the atmospheric moisture profile (which largely determines τ_A), and the surface temperature.

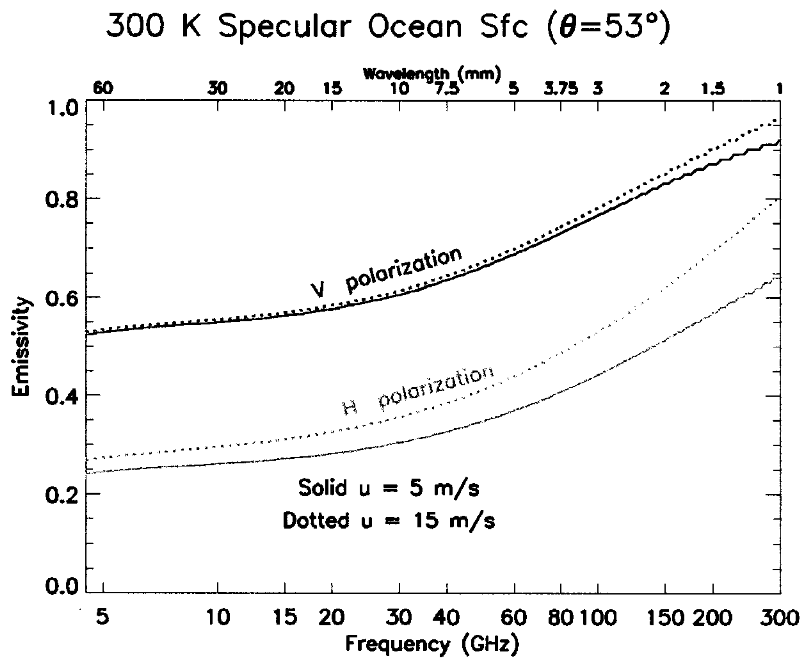

Figure 1.1: The emissivity of an ocean surface, with temperature of 300 K, salinity of 35 ppmv, and wind speeds of 5 and 15 meters per second. Both horizontal and vertical polarizations are shown for a zenith angle of 53°.

Efforts to use Equation 1.3 in retrievals begin with the modeling of the ocean emissivity. The ocean emissivity is typically characterized using three parameters: temperature, salinity, and wind speed (Stogryn, 1967 and Hollinger, 1971). These three ocean parameters are generally assumed horizontally homogenous for a satellite footprint. Shown in figure 1.1 is the emissivity modeled from an ocean surface with temperature of 300 K, salinity of 35 ppmv, and wind speeds of 5 and 15 m/s. Notice the ocean emissivity rises with frequency and the polarization difference reduces with wind speed, most dramatically at higher frequencies. A typical land emissivity value is 0.95 for this range of frequencies. The lower emissivity typical of the ocean surfaces reduces the amount of surface radiation received by the satellite while increasing the fractional amount from the atmosphere. Microwave radiometers originally were designed primarily for use over the ocean, because of the ease in modeling the ocean emission and the larger atmospheric contribution to the total emission.

The contrast between ocean and atmospheric emission is great, with atmospheric emission (not atmospheric scattering) typically raising the satellite radiance and lowering the polarization difference. The amount of increase in the satellite radiance is related to the amount of water vapor and cloud liquid water in the atmospheric column. Figure 1.2 shows the atmospheric transmission as a function of frequency. There are two absorption features due to water vapor centered at 22 and 183 GHz, and two due to oxygen centered at 60 and 118 GHz. The atmospheric transmission decreases with increasing frequency due to an increased sensitivity to atmospheric water vapor. Atmospheric water vapor is concentrated in the lower atmosphere and is an isotropic (unpolarized) emitter. Non-precipitating cloud liquid water droplets typically are a few microns in size while the wavelength of microwave radiation is a few millimeters to a few centimeters. These non-precipitating liquid cloud drops thus have radii much smaller than incident microwave radiation, and absorption processes dominate those of scattering. An addition of small liquid cloud drops increases the atmospheric emission above that of water vapor alone, and further obscures the polarization difference from the surface. The interested reader is referred to chapters five and seven in *The Remote Sensing of the Lower Atmosphere* (Stephens, 1994).

The simplest relation of atmospheric transmission, $e^{-\tau_A}$, to total precipitable water and cloud liquid water assumes a boundary layer temperature equal to the surface temperature, a frequency dependent water vapor extinction per unit mass, and a frequency and cloud temperature dependent liquid water extinction per unit mass

(Staelin, 1976; Grody, 1976). Other methods use non-linear regression equations of microwave satellite brightness temperatures against validation data to determine total precipitable water (Alishouse, 1990a) and cloud liquid water (Alishouse, 1990b). Further methods have been introduced which use the reduction in polarization difference for the retrieval of total precipitable water (Tjemkes, 1991) and cloud liquid water (Greenwald, 1993). However, due to the difficult interpretation of the highly spatially and temporally varying land surface emissivity these retrievals have been limited to ocean regions.

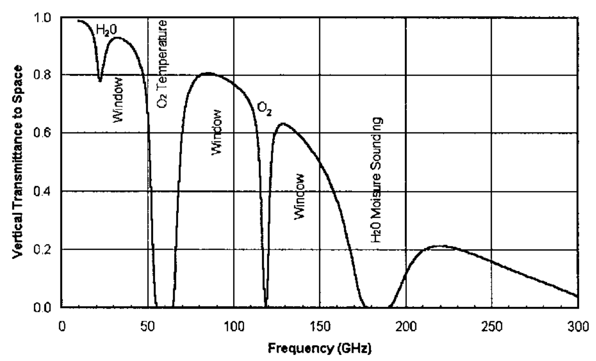

Figure 1.2: The vertical transmittance to space using the 15°N annual atmosphere and the model of Liebe (1992) provided by Dr. Stanley Kidder (http://amsu.cira.colostate.edu/spectrum.html).

1.2 Statement of Problem and Related Research

The microwave land emissivity is sensitive to vegetation type and water content (Ulaby, 1985), soil type, and water content (Njoku, 1982; Schmugge et al., 1986; Choudhury, 1988). Schmugge (1986) reports that at 1.4 GHz the emissivity of soil can vary from 0.95 to 0.6, roughly a 30% change. In addition, microwave land emissivities show characteristic signatures resulting from the volumetric scattering by the vegetative cover (Neale, 1990). Bare ground typically exhibits polarized emission, while scattering by vegetation reduces this polarization difference. As a result of its sensitivity to soil, vegetation, and water, the microwave land emissivity is typically highly variable on small spatial scales and the effective land emissivity over a 10 – 50 km area (typical of a microwave satellite footprint) is difficult to model.

The microwave land emissivity is important for accurate retrievals of both surface and atmospheric parameters over land areas. The atmospheric retrievals are dependent on the ability to extract the atmospheric signal from total upwelling radiance, which is dominated by the strong contribution from the surface emission. If the surface emissivity is known to sufficient accuracy, then the land surface temperature can be retrieved. Also the surface contribution to the total upwelling radiation may be removed, allowing retrievals of the atmospheric parameters.

Retrievals of microwave surface emissivity have been increasing in complexity in recent years. Regression equations have been developed but these don't properly correct for atmospheric attenuation. More robust methods use atmospheric profiles (Felde and Pickle, 1995) and can include land surface temperature retrievals from satellite infrared data (Prigent et al., 1997; Jones and Vonder Haar, 1997), but these studies have been limited spatially and temporally. Further, errors in these microwave emissivity retrievals have rarely been translated into errors in atmospheric parameters.

One study which related microwave land emissivity errors to those in cloud liquid water was that of Greenwald et al., 1999. The Greenwald cloud liquid water retrieval uses the polarization difference of the SSM/I 85.5 GHz channels. Shown in Figure 1.3 are six-day running means and standard deviations of the 85.5 GHz land emissivity polarization difference over the Atmospheric Radiation Measurement (ARM) program central facility. Greenwald uses the values in Figure 1.3 to assign uncertainties in his study, finding cloud liquid water errors from about 0.11 to 0.14 kg m^{-2} for emissivity polarization differences $\Delta\varepsilon \geq 0.015$. Figure 1.4 contains the six-day running means and standard deviations polarization differences from 85.5 GHz emissivities retrieved in the present study for the nearest neighbor to the ARM central facility on a one-half degree grid from SSM/I observation from 2001. In calculating the cloud liquid water errors Greenwald states, "a parameter of special importance is the uncertainty in the surface emissivity." The Greenwald algorithm depends on accurate knowledge of the surface emissivity, and a polarization difference of at least 0.015, so the depolarization of the surface radiation by the cloud liquid water is detectable.

The dominant error source in the retrieval of microwave land emissivity is the land surface temperature. The use of infrared data to retrieve the land surface temperature is attractive because of the stability of the infrared land emissivity (Wan, 1999). The infrared emissivity of water and lush vegetation is similar, and a value of 0.98 is often used. Both Prigent et al. (1997) and Jones and Vonder Haar (1997) retrieve the land surface temperature by setting the infrared land emissivity to a fixed value for the entire domain. However, the infrared surface emissivity is dependent on the vegetation and soil in a region, and can vary temporally as well. In general bare ground, and senescent vegetation have lower infrared emissivity (approaching 0.90). In this study, maps of infrared surface emissivity have been generated by indexing a spectral emissivity library to a vegetation and soil database following recent work by Snyder et al. (1998), Wilber et al. (1999), and Francis (2003). In doing this, it is assumed that over the CONUS summertime season (June, July, and August) the vegetation cover and lushness is not changing dramatically. The infrared emissivity atlas lowers the error in the land surface temperature retrieval subsequently lowering the largest error source in the computation of the microwave land emissivity.

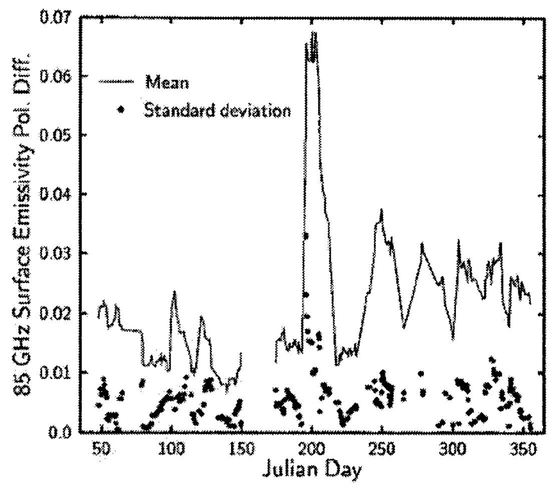

Figure 1.3: Time series of six-day running means and standard deviations for instantaneous 85.5 GHz surface emissivity polarization difference observations at the Atmospheric Radiation Measurement (ARM) programme Central Facility site for 1994 (from Greenwald et al. 1999).

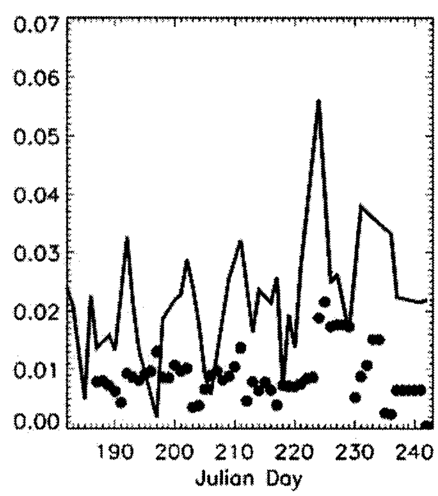

Figure 1.4: Time series of 2001 SSM/I 85.5 GHz emissivity polarization difference retrieved directly using SSM/I brightness temperatures, RUC-2 weather model atmospheric profiles, and GOES retrieved land surface temperature. The microwave emissivities from the nearest neighbor to the ARM Central Facility on a half-degree grid are used to calculate the six-day running mean (solid line) and standard deviation (dots) from Julian day 180 – 245 from 2001.

Forward models for microwave land emissivity have been developed (Weng, 2001) which simulate the sensitivity of the microwave land emissivity to vegetation type and water content; soil type and water content; scattering by snow, desert, and vegetation; and reflection and transmission at the surface-air interface. These models are heavily parameterized, often relying on frequency dependent empirical equations. For example, Choudhury et al. (1979) related surface reflectivity to roughness parameters, which is the formulation used by Weng (2001). The present study is a significant first step in acquiring the observational knowledge necessary to validate these model-based empirical relationships, allowing future work to continue into more complex weather and terrain regimes.

This dissertation retrieves the emissivity for the summertime season over the Conterminous United States (CONUS) and provides estimates of its error. These values provide a characterization of emissivity necessary for probabilistic retrieval systems that seek to retrieve atmospheric parameters over land. In addition, these emissivity values could be compared with land emissivity model estimates to calibrate and validate these emissivity models.

1.3 Research Description

The primary objective of this research is to quantify the means and variability of the microwave land emissivity over the summertime Conterminous United States (CONUS). Microwave land emissivity retrievals are performed for two different satellite sensors, the Department of Defense Satellite Meteorology Program (DMSP) Special Sensor Microwave Imager (SSM/I), and National Oceanic and Atmospheric Association (NOAA) Advanced Microwave Sounding Unit (AMSU). These instruments cover frequencies ranging from 10 – 183 GHz, at resolutions from 7 – 60 km. The sources of radiance measured by the instruments come from the earth's surface, clouds, and oxygen and water vapor gases. The microwave land emissivities retrieved from the large field-of-view of these sensors will be an aggregate or effective emissivity of the pixel which may contain a mixture of forest, shrubs, crop or grass lands, water bodies, urban areas, bare soil, etc.

To retrieve the microwave emissivity from the observations, the atmospheric absorption and land surface temperature must be known. A weather model is used to provide estimates of atmospheric temperature and moisture profiles. These profiles are used with an infrared radiative transfer model to simulate radiances from the GOES satellite in the longwave window (10 – 12 μm) region. The infrared surface emissivity is set to a fixed value, unique for each grid point. The land surface temperature is adjusted so the simulated upwelling radiance matches that recorded by the GOES instrument. To find the microwave emissivity, the land surface temperature is set to the retrieved value and the microwave emissivity is adjusted so the simulated microwave brightness temperature matches the satellite observation (SSM/I or AMSU).

The mean and variance of the microwave emissivity over the summertime CONUS region will be examined. These emissivity statistics are assumed azimuthally independent, and are grouped by vegetation classes. It is shown that the mean emissivity has a strong dependence on density of vegetative cover. The microwave land emissivity should not have a strong dependence on time of day or the satellite used to retrieve the emissivity values. To test the independence of the microwave emissivity to diurnal effects the mean ascending and descending emissivities are compared. To check for individual satellite biases, the mean emissivities from each individual satellite are compared to the satellite composite mean. The resolution of the instruments (7-60 km) is coarse and includes considerable sub-pixel variability. This study focuses on the effective microwave emissivity on a one-half degree grid. Analyses are limited to clear-sky areas, due to the lack of accurate cloud liquid water and ice information, and the decrease in surface contribution to the satellite radiance signal due to cloud attenuation effects.

The microwave emissivities retrieved are used to compile statistics for variational retrievals. These retrievals use probability distributions of the microwave emissivities, emissivity cross-correlations, and estimates of emissivity error. An optimal estimation retrieval of microwave emissivity will use the low frequency channels to retrieve the emissivity at 85.5 GHz. In addition, retrieved microwave emissivities are implemented into a one-dimensional variational retrieval of temperature and moisture. In this framework, the retrieved microwave emissivity will be used to find the sensitivity of the temperature and moisture fields to microwave land emissivity.

1.4 Scope and Sequence

Chapter 1 introduces the microwave emissivity variable, and discusses the potential for atmospheric retrievals using microwave satellite data. Atmospheric retrievals have been performed over ocean areas with success; however, the highly temporal and spatial variability of the land areas has left it largely uncharacterized. This dissertation addresses this problem by presenting a retrieval of microwave land emissivity over a large domain (Conterminous United States) and long time period (June – August of 2000 – 2002). The retrieved microwave emissivities are then used to populate statistics needed for a probabilistic retrieval of atmospheric parameters, and test the sensitivity of the atmospheric parameters to the microwave emissivity. A characterization of microwave land emissivity is essential to atmospheric retrievals over land, and is the focus of this dissertation.

In completing this study, profiles of temperature and moisture from a numerical weather model are used to model the infrared and microwave transmission through the atmosphere. A cloud-screening procedure is implemented so a non-scattering atmosphere may be assumed. An infrared surface emissivity atlas is generated using a spectral library and a database of soils and vegetation. This infrared emissivity atlas is subsequently used in a retrieval of the land surface temperature. The microwave land emissivity is then calculated using the retrieved land surface temperatures. The means and covariance of microwave emissivity are used in an optimal estimator of microwave emissivity. Lastly, the retrieved microwave emissivities are implemented into a one-dimensional variational retrieval of temperature and moisture.

Chapter 2 defines the data sets used and the time period over which the data are analyzed. Both infrared and microwave satellite data are used. The satellite channels are defined spectrally, along with their noise characteristics. Numerical weather models are used to provide atmospheric profiles of temperature and moisture, and the model errors are presented. Infrared Thermometer (IRT) measurements from the Atmospheric Radiation Measurement (ARM) program Southern Great Plains (SGP) site are used to validate the retrieved land surface temperatures. Retrievals of a cloud mask and land surface temperature are obtained from the Moderate Resolution Imaging Spectroradiometer (MODIS) and compared to the cloud mask and land surface temperature retrieved in this study. The times and spatial resolution of these MODIS level 2 products is detailed, and references to the algorithm theoretical basis documents are provided. The resolution and origin of the vegetation and soil databases used in this study are given. To create the infrared emissivity atlas a spectral reflectance library containing samples of terrestrial materials is used. The nature of the samples and spectral resolution of the measurements are given in chapter 2.

Chapter 3 presents the methodology used to complete the microwave land emissivity retrieval. An elements of the microwave emissivity retrieval is a cloud-screening procedure using infrared data. A plane-parallel radiative transfer model is used to make calculations of infrared and microwave radiances. The land surface temperature retrieval is presented, along with an iterative (direct) retrieval of microwave emissivity. Chapter 3 provides an error budget of the microwave land emissivity retrieveal, which concludes that the largest source of error in these retrievals is the estimation of the land surface temperature. Consequently, a strong emphasis is placed on the accurate retrieval of this single parameter. Lastly, chapter 3 presents an optimal estimation approach to retrieve the microwave land emissivity.

Chapter 4 compares results from the infrared cloud mask and the land surface temperature retrieval with independent data. The cloud mask will be validated using level 2 products from the Moderate Resolution Imaging Spectroradiometer (MODIS). The land surface temperature will be validated using a downward looking Infrared Thermometer (IRT) based at the ARM-SGP site, and the MODIS level 2 land surface temperature product.

Chapter 5 presents the microwave emissivity results. The mean, and standard deviation of the microwave emissivity from the SSM/I sensor is examined over the summertime CONUS region. Histograms of the emissivities categorized by surface type are presented. The results of the microwave emissivity optimal estimator are presented, focusing on the retrieval of 85 GHz emissivity. The 85 GHz emissivity is retrieved using all SSM/I channels, and using only the low frequency (≥37 GHz) data. Microwave emissivity is retrieved for the AMSU-A sensor over the over the Atmospheric Radiation Measurement (ARM) program Southern Great Plains (SGP) site. A one-dimensional variational retrieval is used to examine the sensitivity of temperature and moisture profiles to the retrieved AMSU microwave emissivity.

Chapter 6 presents conclusions and suggested future research. Conclusions will cover the principles governing the range of variability seen in emissivity. A discussion of the potential errors in the cloud mask and land surface temperature is provided as well as the ranges of precision that may be expected in the microwave emissivity due to uncertain effects of the terrain of the region. The effect of azimuth angle will be discussed, and how this effect can be addressed in future research. Lastly, we contemplate future work that can add to our knowledge of the Earth's microwave land emissivity, which include global observational retrievals, and calibration and validation of microwave land emissivity models.

2. Data

The study is limited to the summer months (June, July, and August) over the Conterminous United States (CONUS) region for the years 2000, 2001, and 2002. The effective radiating depth in snow changes as a function of frequency, and the age and properties of the snowpack. The single infrared land surface temperature retrieved would be unrepresentative of these different effective radiating surfaces. Consequently, the summer season was selected to avoid areas of snow cover. The temporal range of the study is chosen to examine the emissivities on daily and monthly time scales. Radiance measurements were obtained from three Defense Meteorological Satellite Program (DMSP) Special Sensor Microwave Imagers (SSM/I), two National Oceanic and Atmospheric Association (NOAA) Advanced Microwave Sounding Units (AMSU), and two NOAA Geostationary Operational Environmental Satellites (GOES). Complementing the radiance measurements, the Department of Defense (DoD) Naval Operational Global Atmospheric Prediction System (NOGAPS) and NOAA Rapid Update Cycle (RUC) model analyses provide coincident coverage with profiles of temperature and moisture. RUC data is used for the entire time period and spatial domain, while the global NOGAPS analyses are obtained for July and August of 2000-2002. The RUC analysis are every three hours, while the NOGAPS analysis are every six hours both beginning at 00 UTC.

2.1 Satellite Data

2.1.1 SSMI Instrument

On board the Defense Meteorological Satellite Program (DMSP) satellites F-13, 14, and 15 is the Special Scanner Microwave Imager (SSMI) instrument. The SSM/I is a conically scanning radiometer and measures discrete frequencies and polarizations with 7 channels. The viewing angle of the instrument is 45° corresponding to a local zenith of 53.1°. The SSM/I channels are: 19.35V, 19.35H, 22.235V, 37.0V, 37.0H, 85.5V, and 85.5H GHz. The ground resolution of the instrument is limited by the ability of the antenna to focus the incoming radiation on the detector. Ulaby (1982) states that the far-field condition is satisfied when distance of the observation point (R) is greater than or equal to twice the ratio of the square of the longest dimension of the antenna (d) and the wavelength (λ),

$$R \geq 2\frac{d^2}{\lambda}. \tag{2.1}$$

When the far-field condition is satified, Fraunhoffer diffraction, after Joseph von Fraunhoffer (1787-1826), is the limiting factor. At this limit the instrument Field-of-View (FOV) is proportional to the ratio of the wavelength and the antenna diameter,

$$FOV \propto \frac{\lambda}{d}. \tag{2.2a}$$

Using a constant wave propagation speed (the speed of light, c), this relation can also be expressed in terms of frequency (ν),

$$\lambda = \frac{c}{\nu} \tag{2.2b}$$

$$FOV \propto \frac{1}{\nu d}. \tag{2.2c}$$

At 19 GHz, the effective field of view is approximately 60 km, while at 85 GHz it improves to 15 km. Shown in Table 2.1 are characteristics of the SSM/I instruments.

Table 2.1: Characteristics of the SSM/I instrument (Adapted from Hollinger et al. 1990).

Channel	Frequency (GHz)	Polarization	EFOV (km)	NEΔT (K)	Accuracy (K)
1	19.35	V	69 × 43	0.45	1.5
2	19.35	H	69 × 43	0.42	1.5
3	22.235	V	60 × 40	0.73	1.5
4	37.0	V	37 × 28	0.37	1.5
5	37.0	H	37 × 28	0.38	1.5
6	85.5	V	15 × 13	0.69	1.5
7	85.5	H	15 × 13	0.73	1.5

SSM/I data is analyzed from June through August of 2000 – 2002. The F-13, F-14, F-15 satellites all covered the this period. The data from the SSM/I orbits is truncated to the CONUS spatial domain. Satellite antenna temperature are obtained from the Satellite Active Archive (SAA) and converted to brightness temperatures using the Wentz calibration scheme (Wentz, 1988). The satellite brightness temperature field is re-sampled to one-half degree resolution (~50 km).

2.1.2 AMSU Instrument

The Advanced Microwave Sounding Unit (AMSU) flies aboard the National Oceanic and Atmospheric Association (NOAA) satellites 15, 16, and 17. AMSU is a cross-track scanning radiometer and measures at 20 discrete frequencies. Characteristics of the AMSU-A channels are shown in Table 2.2. The polarization received by the AMSU instrument varies with scan angle due to a rotating mirror, which reflects into a fixed feed horn. Grody et al. (2001) propose a mixing formula, which neglects cross-polarization terms, to combine horizontal (ε_H) and vertical (ε_V) components of emissivity at a given scan angle θ_s and local zenith angle θ,

$$\varepsilon = \varepsilon_V(\theta)\cos^2\theta_s + \varepsilon_H(\theta)\sin^2\theta_s. \quad (2.3)$$

This equation is appropriate for those channels with vertical nadir polarization. If the nadir polarization is horizontal, $\varepsilon_H(\theta)$ should be multipliled by the $\cos^2(\theta_s)$ term, and $\varepsilon_V(\theta)$ by $\sin^2(\theta_s)$. The AMSU consists of two instruments named AMSU-A and AMSU-B. The range of lower frequency and resolution channels on AMSU-A is from 23.8 – 89.0 GHz. The range of higher frequency and resolution channels on AMSU-B is from 89.0 – 183 GHz. AMSU-B data will not be used in this study.

Table 2.2: Characteristics of AMSU-A channels adapted from Grody et al. (2001).

Channel	Frequency (GHz)	# of Bands	NEΔT (K)	Nadir Polarization	Beamwidth (deg) 3 dB Measured
1	23.8	1	0.3	V	3.5
2	31.4	1	0.3	V	3.4
3	50.3	1	0.4	V	3.7
4	52.8	1	0.25	V	3.7
5	53.596±0.115	2	0.25	H	3.7
6	54.4	1	0.25	H	3.6
7	54.9	1	0.25	V	3.6
8	55.5	1	0.25	H	3.6
9	57.2	1	0.25	H	3.5
10	57.29±.217	2	0.4	H	3.5
11	57.29±.322±.048	4	0.4	H	3.5
12	57.29±.322±.022	4	0.6	H	3.5
13	57.29±.322±.010	4	0.8	H	3.5
14	57.29±.322±.0045	4	1.2	H	3.5
15	89.0	1	0.5	V	3.5

The AMSU-A does not have a nadir view angle and has 15 discrete scanning angles from 1.7 – 48.3° to each side of nadir, corresponding to local zenith angles of 1.9 – 57.6°. The AMSU-A instrument has 12 of 15 channels located throughout the oxygen absorption maxima centered at 60 GHz, and the AMSU-A is designed primarily as a temperature sounding instrument. AMSU-B has three channels centered about the water vapor absorption feature located at 183.3 GHz, and is designed to be primarily a water vapor sounding instrument.

Table 2.3: Resolution of AMSU-A instrument as a function of scan position using a 3.5° beamwidth.

Scan Position	Scan Angle*	Distance of Subpoint from Nadir		Along-Track Beam Size	Cross-Track Beam Size	Viewing Angle
	deg	deg	km	km	km	deg
1	-48.3	9.3	1033	84	157	57.6
2	-45.0	8.1	898	77	129	53.1
3	-41.7	7.1	785	72	109	48.7
4	-38.3	6.2	688	68	95	44.5
5	-35.0	5.4	603	64	84	40.4
6	-31.7	4.7	527	61	76	36.4
7	-28.3	4.1	458	59	70	32.5
8	-25.0	3.5	394	57	65	28.5
9	-21.7	3.0	334	55	61	24.7
10	-18.3	2.5	278	54	58	20.8
11	-15.0	2.0	224	53	55	17.0
12	-11.7	1.5	172	52	54	13.2
13	-8.3	1.1	122	52	52	9.4
14	-5.0	0.7	73	51	51	5.7
15	-1.7	0.2	24	51	51	1.9
16	1.7	0.2	24	51	51	1.9
17	5.0	0.7	73	51	51	5.7
18	8.3	1.1	122	52	52	9.4
19	11.7	1.5	172	52	54	13.2
20	15.0	2.0	224	53	55	17.0
21	18.3	2.5	278	54	58	20.8
22	21.7	3.0	334	55	61	24.7
23	25.0	3.5	394	57	65	28.5
24	28.3	4.1	458	59	70	32.5
25	31.7	4.7	527	61	76	36.4
26	35.0	5.4	603	64	84	40.4
27	38.3	6.2	688	68	95	44.5
28	41.7	7.1	785	72	109	48.7
29	45.0	8.1	898	77	129	53.1
30	48.3	9.3	1033	84	157	57.6

* Negative numbers indicate left of track facing in the direction of satellite motion.

AMSU-A data is analyzed specifically over the ARM-SGP site in northern Oklahoma. NOAA-15 data was obtained for July and August of 2000 – 2002, and NOAA-16 data for July and August 2001 – 2002. The AMSU data was collected from NOAA Satellite

Active Archive and the NOAA derived calibration coefficients were used to convert the count to brightness temperatures (Kidwell, 2000). The AMSU-A instrument contains two antenna systems, AMSU-A1 (channels 3 – 15) and AMSU-A2 (channels 1 and 2). This allows a nearly contant 3 dB measured beamwidth of ~3.5° (the nominal specification is 3.3° for all AMSU-A channels), ground footprints are calculated using a 3.5° beamwidth and shown in Table 2.3.

2.1.3 GOES instrument

The Geostationary Operational Environmental Satellite (GOES) imager is a geostationary orbiting satellite with channels in the visible and infrared portion of the electromagnetic spectrum. GOES channels 2 and 4 with spectral response functions centered at 3.9 and 10.7 micrometers are used for cloud screening. The data from these channels is on a 4 km grid. For the time period of June through August of 2000 – 2002 the two operational GOES satellites were GOES-08 and GOES-10. GOES-8 is located over –75W longitude while GOES-10 is at –110W longitude. The scans used are the full disk scans which occur at 3 hour intervals beginning at 00:00 UTC for GOES-10, and 02:45 UTC for GOES-08. These scenes were chosen to match the three-hourly numerical model analyses.

The GOES data was obtained from CIRA archives and was converted to brightness temperatures using the NOAA calibration coefficients (Weinreb, 1997). Characteristics of the GOES satellites are shown in Table 2.4. Don Hilger of the Cooperative Institute for Research in the Atmosphere (CIRA) at Colorado State University calculated the radiance noise, using the pre-launch noise specifications from the manufacturer.

Table 2.4: Characteristics of GOES imager.

Channel	Central Wavelength (μm)	Resolution (km)	Radiance Noise [W/($m^2 \times sr \times \mu m$)]
1	0.65	1	3.4
2	3.9	4	0.053
3	6.7	8	0.14
4	10.6	4	0.59
5	12.0	4	0.61

2.2 Independent Infrared Comparison Data

2.2.1 Infrared Thermometer (IRT)

Infrared Thermometer (IRT) data were collected from the Atmospheric Radiation Measurement (ARM) program Southern Great Plains (SGP) site for July through August of 2000 – 2002. The location of the ARM-SGP site is shown in Figure 2.1. The IRT is a ground-based radiation pyrometer that provides measurements of the equivalent black body brightness temperature of the scene in its field of view. The IRT are mounted on 10 and 25 meter towers at the ARM-SGP site. The IRT measurements are from a 25-meter tower for July and August of 2000, a 10-meter tower for July and August of 2001, and both a 10 and 25-meter tower for July and August of 2002. The IRT operates within the spectral range of 9.6 to 11.5 μm, and retrieves temperature from 223 – 773 K with an accuracy of 0.5 K (the specifications of the Wintronics Inc. IRT instrument were obtained from ARM web site, www.arm.gov, on the IRT instrument page: http://www.arm.gov/docs/instruments/static/irt.html). The attenuation due to water vapor and carbon dioxide is neglected.

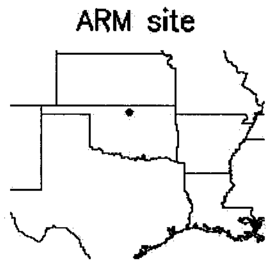

Figure 2.1: Location of the Atmospheric Radiation Measurement (ARM) program Southern Great Plains (SGP) site.

2.2.2 MODIS Level-2 Cloud-Mask

The 36 channel Moderate Resolution Imaging Spectroradiometer (MODIS) is used to generate a cloud-mask at 0.25 and 1 km resolutions (Ackerman et al., 2002). The 1 km resolution cloud mask is used for this study. There are 12 operational tests employed in the MODIS cloud mask algorithm. The land surface determines which of the twelve tests are used to determine cloud cover and are shown in Figure 2.2. Seven different tests are applied during the daylight hours and employ both thermal and reflectance based tests. Five tests are applied at nighttime when only thermal tests may be used. The MODIS cloud mask includes new spectral techniques and incorporates many of the existing techniques to provide arguably the most proficient cloud mask currently available. Additional details on the MODIS cloud mask may be found in the MOD35 Algorithm Theoretical Basis Document (ATBD) of Ackerman et al. (2002).

The MODIS cloud mask data with at least partial CONUS coverage was obtained for a selection of days in August of 2001 and 2002. MODIS flies aboard National Aeronautics and Space Administration (NASA) Earth Observing System (EOS) AM and PM platforms. EOS-PM (Aqua) was just becoming operational in August of 2002. The MODIS-Aqua cloud mask (version 3) was obtained for August 14, 21, and 28th of 2002. The EOS-AM (Terra) platform became operational in 1999. The MODIS-Terra cloud mask (version 4) was obtained for August 1, 8, 14, 21, and 28th of 2001; and August 1-4, 8, 14, and 21st of 2002.

	Daytime Ocean	Nighttime Ocean	Daytime Land	Nighttime Land	Daytime Snow/ice	Nighttime Snow/ice	Daytime Coastline	Nighttime Coastline	Daytime Desert	Nighttime Desert
BT_{11} (Bit 13)	✓	✓								
$BT_{13.9}$ (Bit 14)	✓	✓	✓	✓	✓	✓	✓	✓	✓	✓
$BT_{6.7}$ & BT_{11} - $BT_{6.7}$ (Bit 15)	✓	✓	✓	✓	✓	✓	✓	✓	✓	O
$R_{1.38}$ (Bit 16)	✓		✓		✓		✓		✓	
$BT_{3.7}$ - BT_{12} (Bit 17)				✓		✓				✓
$BT_{8.6}$ - BT_{11} & BT_{11} - BT_{12} (Bit 18)	✓	✓	✓	✓			✓	✓	✓	✓
BT_{11} - $BT_{3.9}$ (Bit 19)	✓	✓	✓	✓	✓	✓	✓	✓	✓	✓
$R_{0.66}$ or $R_{0.87}$ (Bit 20)	✓		✓		✓		✓		✓	
$R_{0.87}/R_{0.66}$ (Bit 21)	✓		✓				✓			
$BT_{7.3}$ - BT_{11} (Bit 23)				O				O		O
Temporal Consistency (Bit 24)	O	O								O
Spatial Variability (Bit 25)	✓	✓								

Figure 2.2: Chart showing which of the 12 spectral tests are used for each land surface type. Check marks indicate an implemented test while the circle indicates that the test is not yet fully test on the MODIS data (Ackerman, 2002).

2.2.3 MODIS Level-2 Land Surface Temperature (LST)

The MODIS derived Land Surface Temperature (LST) product is produced as a daily daytime and nighttime 5 km global land product (Wan, 1999). A physics-based day/night algorithm (Wan and Li, 1997) retrieves the surface infrared emissivity and temperature from a pair of daytime and nighttime MODIS data in seven infrared bands (bands 20, 22, 23, 29, and 31-33). The algorithm depends on view angle, atmospheric column water vapor and surface air temperature, and includes input from the MODIS retrieved atmospheric temperature and water vapor profile product (Ma et al., 2002). Fourteen unknown variables exist in the retrieval method: seven infrared band emissivities, day/night surface temperature, day/night atmospheric temperature at the surface level, day/night total precipitable water, and the anisotropic factor of solar bidirectional reflectance distribution function. These variables are used to form a set of 14 nonlinear equations, which are solved by a least-squares fit method (Wan and Li, 1997). Additional information on the LST algorithm may be found in the MOD11 Algorithm Theoretical Basis Document (ATBD) of Wan (1999).

The MODIS 5 km daily LST is a tiled product on a sinusoidal projection. Tiles of the MODIS-Terra version 3 LST product were obtained over the CONUS region for July through August of 2001 and 2002.

2.3 Numerical Weather Model Analysis

2.3.1 The Rapid Update Cycle (RUC) Model

The Rapid Update Cycle (RUC) (Benjamin et al., 1998) model employs a hybrid isentropic-sigma vertical coordinate, where the vertical grid is isentropic except at the ground where a sigma (terrain following) coordinate is used. The RUC version covering the study time period, version 2, utilizes a conic projection with 40 km grid spacing. The RUC-2 model coverage includes the contiguous U.S. and extends about 500 km off each coastline; as well as, south to 20N and north to 55N (see Figure 2.3). All model computations are performed with six 'native' or analysis variables, which are pressure, the Montgomery stream function, virtual potential temperature, condensation pressure, and the horizontal wind components relative to the grid (u and v). The variables examined in this study are profiles of relative humidity, and temperature. These profiles are computed from the native variables and interpolated to an isobaric grid with 25 hPa spacing by the National Centers for Environmental Prediction (NCEP).

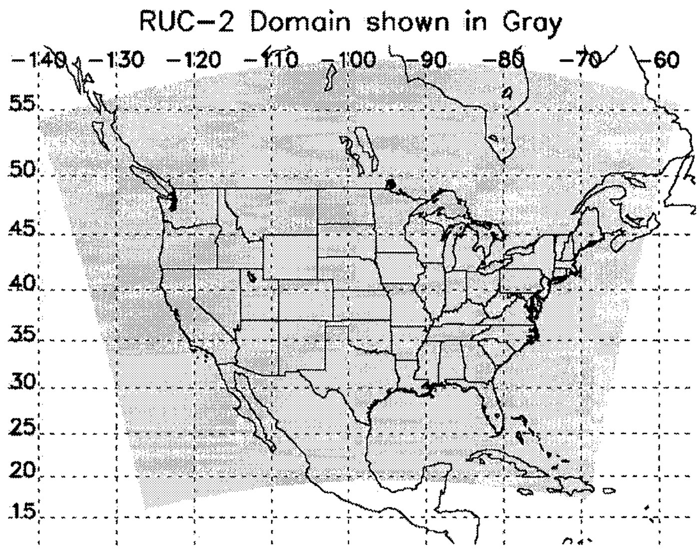

Figure 2.3 RUC-2 domain.

Mixing ratio, w, is calculated from the model temperature and relative humidity fields. Using an empirically fit function, the saturation vapor pressure, e_s, is calculated as a function of temperature (T) in degrees Celsius,

$$e_s = 6.1365e^{\frac{17.502(T)}{240.97+T}} . \tag{2.4}$$

Vapor pressure is then calculated using a percentage value of relative humidity,

$$e_v = \frac{rh}{100} \times e_s . \tag{2.5}$$

Lastly, the mixing ratio, w, is found in g/kg from the vapor pressure and pressure level, p, in hPa,

$$w = 1000 \times \frac{0.622e_v}{p - e_v} . \tag{2.6}$$

Observational data ingested by the RUC-2 model is converted to the RUC-2 analysis variables (see previous section for a description of analysis variables) and interpolated to a background grid. Radiosonde data is incorporated twice daily at 00 and 12 UTC. Winds, temperature, and pressure altitude from aircraft are obtained from ACARS (ARINC [Aeronautical Radio, Inc.], Communications, Addressing, and Reporting System). Wind observations from 27-30 profilers (mostly from the Wind Profiler Demonstration Network), the Doppler Radar VAD (Velocity Azimuth Display) product, and GOES high-density gradient winds are ingested into the RUC-2 model. The ingested GOES winds are over the ocean only, and use the visible and 10.7 μm channels on the GOES imager. Precipitable water estimates from both the SSM/I and GOES satellites are also used in the analyses (Benjamin, 1998).

2.3.2 Navy Operational Global Atmospheric Prediction System (NOGAPS) Model

The Navy Operational Global Atmospheric Prediction System (NOGAPS) (Hogan and Rosmond, 1991) is the primary Numerical Weather Prediction (NWP) system providing global weather guidance for all branches of the Department of Defense (DoD). The NOGAPS system is an operational global spectral forecast model run four times each day performing forecasts to 144 hours. All research and development of NOGAPS is undertaken at the Marine Meteorology Division of the Naval Research Laboratory (NRL) in Monterey, CA. This model includes the NRL Atmospheric Variational Data Assimilation System (NAVDAS) (Daley and Barker, 2001), a newly operational three-dimensional variational data assimilation suite for generating atmospheric state estimates. NAVDAS is formulated in observation space, and includes forward operators for assimilation of AMSU data.

NOGAPS analysis fields were obtained for July and August of 2001, on a vertical pressure coordinate system at 1-degree resolution. Variables used in this study are isobaric profiles of relative humidity, and temperature. The model analyses are reported every 6 hours beginning at 00 UTC. These analyses are coarse temporally and spatially, but in the 1DVAR retrieval used later in this study, the NAVDAS system interpolates the model fields spatially and temporally to the satellite observation points.

2.4 Vegetation and Soil Databases

2.4.1 Vegetation Index

The vegetation classification was derived from the global 1-km Advanced Very High Resolution Radiometer (AVHRR) at the University of Maryland (Hansen et al., 2000). The Hansen et al. (2000) dataset is derived from 1992-1993 1 km AVHRR data using a hierarchical tree structure to classify the land into 12 vegetation categories. The approach involves a hierarchy of pair-wise class trees where a logic based on vegetation form was applied until all classes were depicted. 41 multi-temporal AVHRR metrics were used to predict class membership. Minimum annual red reflectance, peak annual Normalized Difference Vegetation Index (NDVI), and minimum channel 3 (3.55 – 3.93 μm) brightness temperature were among the most used metrics. Depictions of forests, woodlands, and mechanized agriculture are in good agreement with other sources of information; however, low biomass agriculture and high-latitude broadleaf forest are not.

The vegetation field includes a percent of each vegetation type in the 1 km cell. Shown in Figure 2.4 is the fractional vegetation cover, which is divided among the 14 land cover classifications. The data obtained are the background fields for the North American Land Data Assimilation System (NLDAS) and are provided as percent of each vegetation type on a 1/8th degree grid over the CONUS. Table 2.5 lists the fourteen classes from the University of Maryland (UMd) land cover layer dataset, along with a broad 4-category classification, which is displayed in Figure 2.5.

Table 2.5: The 14 ground cover types defined by Hansen (2000) in the AVHRR derived database.

Category	Hansen Classification	4-Category Classification
1	Water and Goode's Interrupted Space	
2	Evergreen Needleleaf Forest	Forest
3	Evergreen Broadleaf Forest	Forest
4	Deciduous Needleleaf Forest	Forest
5	Deciduous Broadleaf Forest	Forest
6	Mixed Cover	Grassland
7	Woodland	Forest
8	Wooded Grassland	Grassland
9	Closed Shrubland	Grassland
10	Open Shrubland	Grassland
11	Grassland	Grassland
12	Cropland	Cropland
13	Bare Ground	Bare
14	Urban and Built-Up	

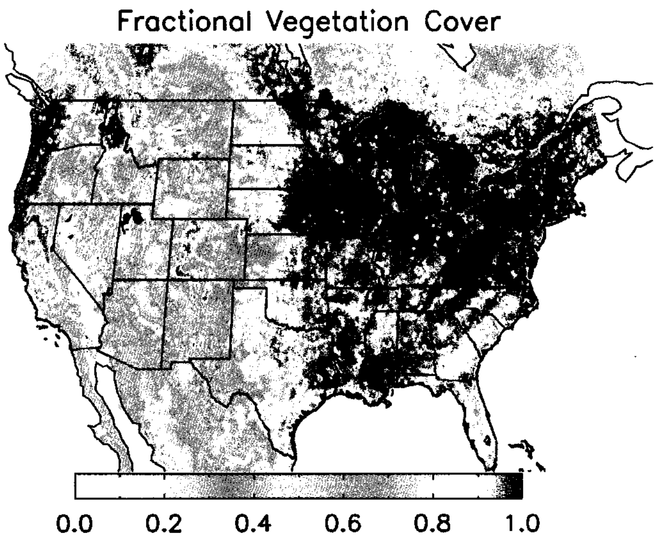

Figure 2.4: Fractional vegetation cover on 1/8th degree grid, based on the 1 km vegetation classification of Hansen (2000).

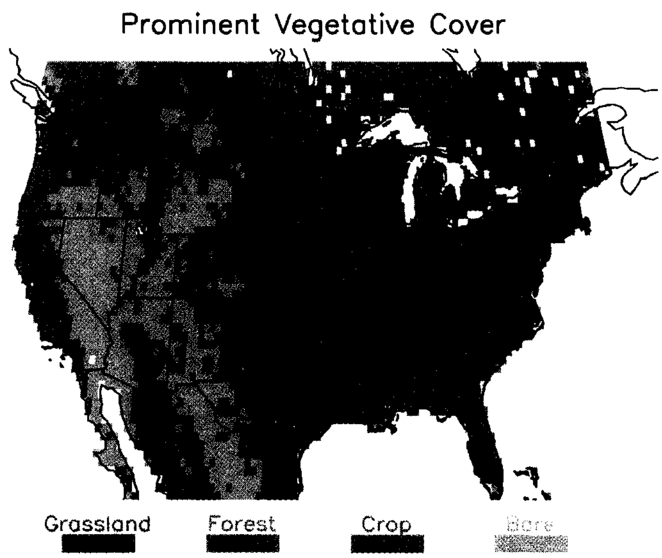

Figure 2.5: Prominent vegetation type in four broad categories adapted from the 1 km vegetation classification of Hansen (2000).

2.4.2 Soil Index

Miller and White (1998) created a 1 km soil texture classification for the Conterminous United States (CONUS-SOIL) from the State Soil Geographical (STATSGO) database developed by the U.S. Department of Agriculture-Natural Resources Conservation Service. The CONUS-SOIL database creates map coverages of soil properties including soil texture and rock fragment classes, depth-to-bed-rock, bulk density, porosity, rock fragment volume, available water capacity, and sand/silt/clay fractions. Interpolation procedures for the continuous and categorical variables describing these soil properties were developed and applied to the original STATSGO data.

Table 2.6: The 16 soil classifications defined in the CONUS-SOIL database of Miller and White (1998).

Category	Classification
1	Sand
2	Loamy sand
3	Sandy loam
4	Silt loam
5	Silt
6	Loam
7	Sandy clay loam
8	Silty clay loam
9	Clay loam
10	Sandy clay
11	Silty clay
12	Clay
13	Organic materials
14	Water
15	Bedrock
16	Other

In the CONUS-SOIL product, there are 16 soil texture classifications (shown in Table 2.6) and 11 soil layers. In this study only the top 5 cm layer is considered. The CONUS-SOIL product reports the frequency of each soil classification given as a percent for each 1 km cell. The data obtained for this study was a background field for the North American Land Data Assimilation System (NLDAS) and is presented as a percent of each soil type at 1/8th degree resolution (~12.5 km).

2.5 Spectral Reflectance Library

The John Hopkins University spectral reflectance library is used to aid in creation of an infrared surface emissivity look-up table. This library contains 41 soil samples, 4 vegetation samples, and 4 water samples covering the spectral range of 715 - 5000 cm^{-1} (2 – 14 micrometers) at approximately 4 cm^{-1} resolution and is based on the laboratory measurements of Salisbury and D'Aria (1992). Salisbury and D'Aria (1992) report that the reflectance measurements were made using an interferometer spectrometer with an integrating sphere coated with a diffusely reflecting gold surface. The entrance port was 10° off the vertical and the detector port was placed at an angle 90° to the principle plane of the sphere. Figure 2.6 shows reflectance measurements for 4 soil samples, 4 water samples, and 41 soil samples with class or subclass equal to sand, silt, soil or clay.

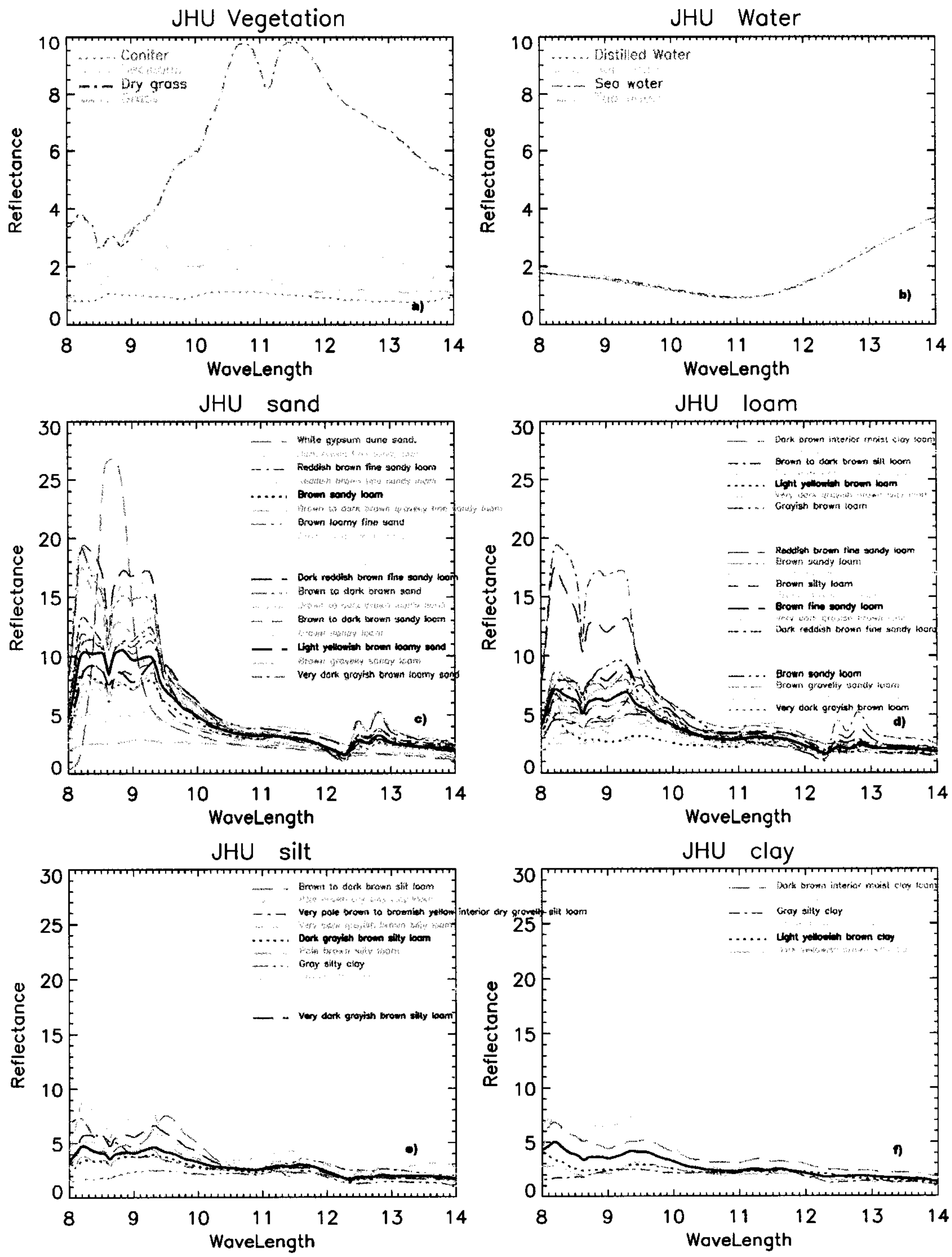

Figure 2.6: The directional hemispheric reflectance measurements from 4 vegetation, 4 water, and 41 soil samples in the John Hopkins spectral library (Salisbury and D'Aria, 1992); a) four vegetation samples b) four water samples c) soil samples with sand class or subclass, mean in black d) soil samples with loam class or subclass, mean in black e) soil samples with silt class or subclass, mean in black f) soil samples with clay class or subclass, mean in black.

3. Methodology

This chapter outlines the approaches to developing a cloud mask, and retrieving land surface temperature and microwave land emissivity. Infrared data from the GOES satellites is used to produce both the cloud mask and the retrieval of land surface temperature. The GOES cloud mask is an adaptation of an operational scheme developed by Jedlovec (2003). Both the land surface temperature retrieval and the microwave land emissivity calculation will use a plane-parallel radiative transfer model, with extinction coefficients in the infrared calculated using a correlated k-distribution formulated by Kratz (1995), and in the microwave using the millimeter wave propagation model of Liebe (1992). In the land surface temperature retrieval, the infrared land emissivity will be assigned to each grid point based on the soil and vegetation frequency and type, but will remain fixed for the study time period. The microwave land emissivity is retrieved both by a direct inversion (which assumes no model or instrument error), and an optimal estimation approach. The optimal estimation (or variational) approach includes information on the error characteristics of model analyses, satellite observations, and the radiative transfer model. The optimal estimation retrieval produces estimates of microwave emissivity and emissivity error.

3.1 Cloud Screening

A Bi-Spectral Threshold (BST) cloud detection methodology is employed. It is based on a procedure implemented at the Global Hydrology and Climate Center (GHCC) by

Jedlovec and Laws (2003) named the Bi-spectral Threshold and Height (BTH) method. The BTH method implemented at GHCC provides estimates of cloud height, but for this study only the cloud mask is needed. The cloud mask detection procedure will be referred to as Bi-Spectral Threshold (BST) cloud mask. During the daytime, greater solar reflectance or lower emission temperatures than the underlying surface can generally be used to identify mid and high level clouds at 3.9 and 10.7 μm. At nighttime, cold or warm anomalies of GOES $T_{B10.7\mu m}$ - $T_{B3.9\mu m}$ spectral differences may be used as an indicator of cloud.

GOES channel 2, centered at 3.9 μm, is more sensitive to sub-pixel warm areas in a scene than channel 4, centered at 10.7 μm. This sub-pixel sensitivity can be attributed to two factors: 1) the change in radiance with respect to temperature is greater at shorter wavelengths, and 2) diffraction at the GOES scan mirror is proportional to wavelength. The change in radiance with respect to change in scene temperature varies as T to a power inversely proportional to wavelength. Because of this fact, we would not expect the same radiance temperature from a planar surface of constant infrared emissivity unless it has a uniform temperature. If the temperature is non-uniform, the warmer areas will raise the scene radiance more in the 3.9 μm channel producing a warmer brightness temperature than that produced from the same scene by the 10.7 μm channel. In the absence of sunlight, this results in warmer clouds from the 3.9 μm channel. The $T_{B10.7}$ - $T_{B3.9}$ spectral difference can become even larger for extremely cold clouds because the GOES 3.9 μm channel saturates at 235 K, while the 10.7 μm channel retrieves temperatures down to ~190 K. The diffraction at the GOES scan mirror of diameter, D, is proportional to the ratio of the wavelength and diameter, λ/D. The GOES 3.9 and 10.7 μm channels share a common scan mirror; consequently, the energy focused on the detector from within a 4 km Field-Of-View (FOV) is 85% for the

3.9 μm channel, and 68% for the 10.7 μm channel. This difference in FOV serves to enhance the 3.9 μm channel sensitivity to sub-pixel warm spots.

The GOES imager channels 2 and 4, centered at 3.9 and 10.7 μm respectively, are used for cloud screening. The method employs two spatial tests, and two threshold tests to complete the cloud masking routine. The spatial tests use large pixel-to-adjacent pixel discontinuities to indicate the presence of clouds. The threshold tests use GOES $T_{B10.7\mu m}$ - $T_{B3.9\mu m}$ spectral differences, and are separated into daylight and nighttime hours. During daylight hours, the 3.9 μm channel has contributions from reflected solar radiation. Clouds typically reflect more solar radiation at 3.9 μm than the land. A monthly minimum background image is created to find the clear-sky land reflection at 3.9 μm, and is used to discriminate cloud over land. At nighttime, sufficiently thick mid and high level clouds will cause negative GOES $T_{B10.7\mu m}$ - $T_{B3.9\mu m}$ spectral differences. Clouds in temperature inversions (e.g., fog) are warmer than the underlying surface. At night, these inversion clouds will cause positive GOES $T_{B10.7\mu m}$ - $T_{B3.9\mu m}$ spectral differences.

Implementation of the BST cloud mask requires three background images for each hour of the day. In Jedlovec's implementation methodology three background images are prepared over 20-day intervals for each hour of the day. Present implementation prepares background images at 3-hourly intervals over a monthly time interval. The first background image is a warmest pixel image prepared from the $T_{B10.7}$. The other two background images are prepared from the $T_{B10.7}$ - $T_{B3.9}$ differences over the monthly interval. The first difference background is the warmest pixel when the $T_{B10.7}$ - $T_{B3.9}$ difference is negative, the second is the coldest pixel when the $T_{B10.7}$ - $T_{B3.9}$ difference is positive. These backgrounds are shown for 06 UTC (nighttime) and 18 UTC (daytime)

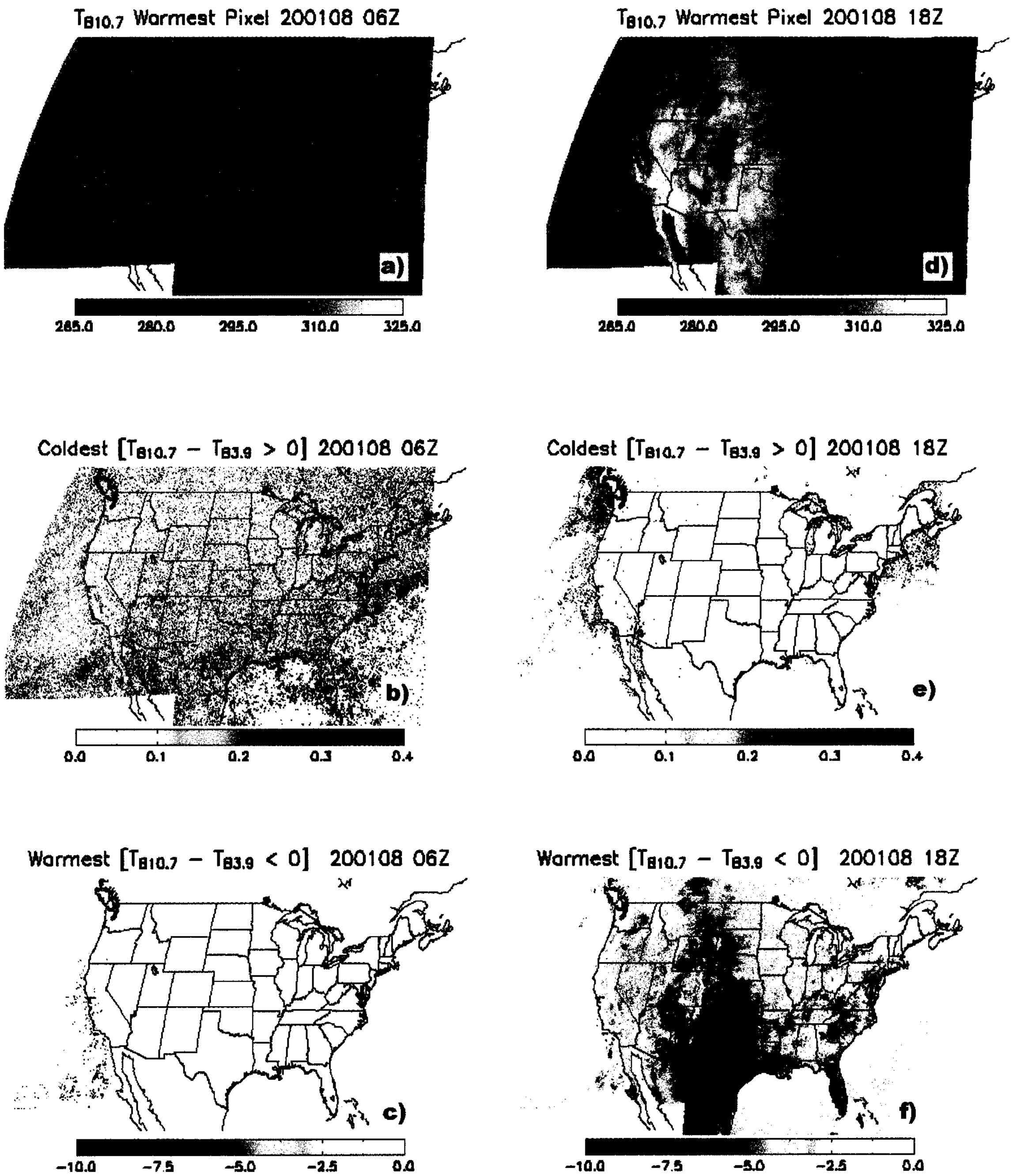

Figure 3.1: The background images for two hours of August 2001: a) 06 UTC warmest T_B(10.7 μm) pixel b) 06 UTC coldest positive difference T_B(10.7 μm) - T_B(3.9 μm) c) 06 UTC warmest negative difference T_B(10.7 μm) - T_B(3.9 μm) d) 18 UTC warmest T_B(10.7 μm) e) 18 UTC coldest positive difference T_B(10.7 μm) - T_B(3.9 μm) f) 18 UTC warmest negative difference T_B(10.7 μm) - T_B(3.9 μm).

from the month of August of 2001 in Figures 3.1a – 3.1f. The warmest $T_{B10.7}$ pixel images show that at night (06 UTC) the coldest temperatures are over the high mountains in Colorado, while the warmest temps are over the western plains. The coldest positive differences have values departing from zero primarily during the nighttime, while the warmest negative differences have values departing from zero during the daytime. When applying the technique, sufficiently thick clouds mid and high level clouds exhibit negative $T_{B10.7}$ - $T_{B3.9}$ values both day and night; while low inversion clouds will exhibit negative $T_{B10.7}$ - $T_{B3.9}$ values during the day, and positive $T_{B10.7}$ - $T_{B3.9}$ values at night.

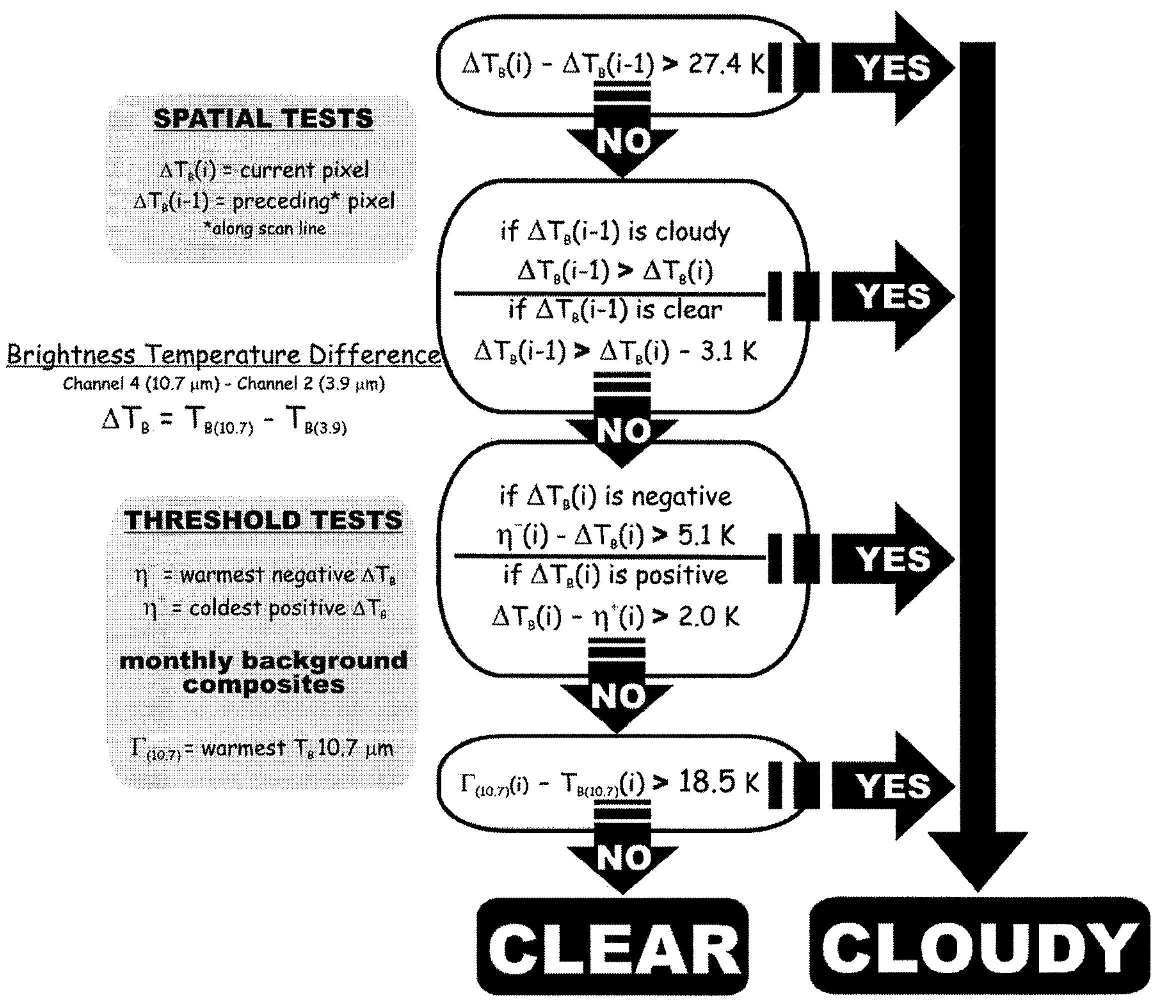

Figure 3.2: Flow chart describing the cloud mask logic (adapted from Jedlovec and Laws, 2003).

The testing procedure is outlined in a flow chart shown in Figure 3.2, and begins with two spatial tests. The first spatial test uses the $T_{B10.7}$ - $T_{B3.9}$ difference, and compares two adjacent pixels along a scan line. If the $T_{B10.7}$ - $T_{B3.9}$ difference for a pixel is 27.4K greater than that of the preceding pixel a cloud edge is detected and the pixel is marked cloudy. The second spatial test again compares the $T_{B10.7}$ - $T_{B3.9}$ difference for two adjacent pixels along a scan line. If the preceding pixel is cloudy with a $T_{B10.7}$ - $T_{B3.9}$ difference that is warmer than the current pixel $T_{B10.7}$ - $T_{B3.9}$ difference the current pixel is flagged as cloudy. If the preceding pixel is clear with a $T_{B10.7}$ - $T_{B3.9}$ difference that is 3.1 K warmer than the current pixel $T_{B10.7}$ - $T_{B3.9}$ difference, the current pixel is declared cloudy.

Following the spatial tests are two threshold tests, which employ the background images. The threshold tests account for the majority of the cloudy pixels flagged in the procedure. The first threshold test uses the $T_{B10.7}$ - $T_{B3.9}$ difference. If the $T_{B10.7}$ - $T_{B3.9}$ difference is negative, it will be marked as cloudy if it is 5.1 K colder than the warmest negative pixel in the background image. If the $T_{B10.7}$ - $T_{B3.9}$ difference for a pixel is positive, it will be marked as cloudy if it is 2.0 K warmer than the coldest positive pixel in the background image. Lastly, if the $T_{B10.7}$ is 18.5 K colder than the warmest pixel background image it is marked as cloudy. Figures 3.3a – 3.3f show brightness temperature images from August 01, 2001 and the resulting cloud mask. In the cloud mask, Figure 3.3c, the test that first flagged a cloudy pixel is indicated. The 06 UTC images are at nighttime, and cold temperatures in the 10.7 μm image easily identify thick mid and high level clouds. The 10.7μm – 3.9μm difference image is shown in Figure 3.3b, and many of these same thick clouds are identified by differences greater than – 5 K. Low water clouds are identified by the positive differences, and are seen off the coast

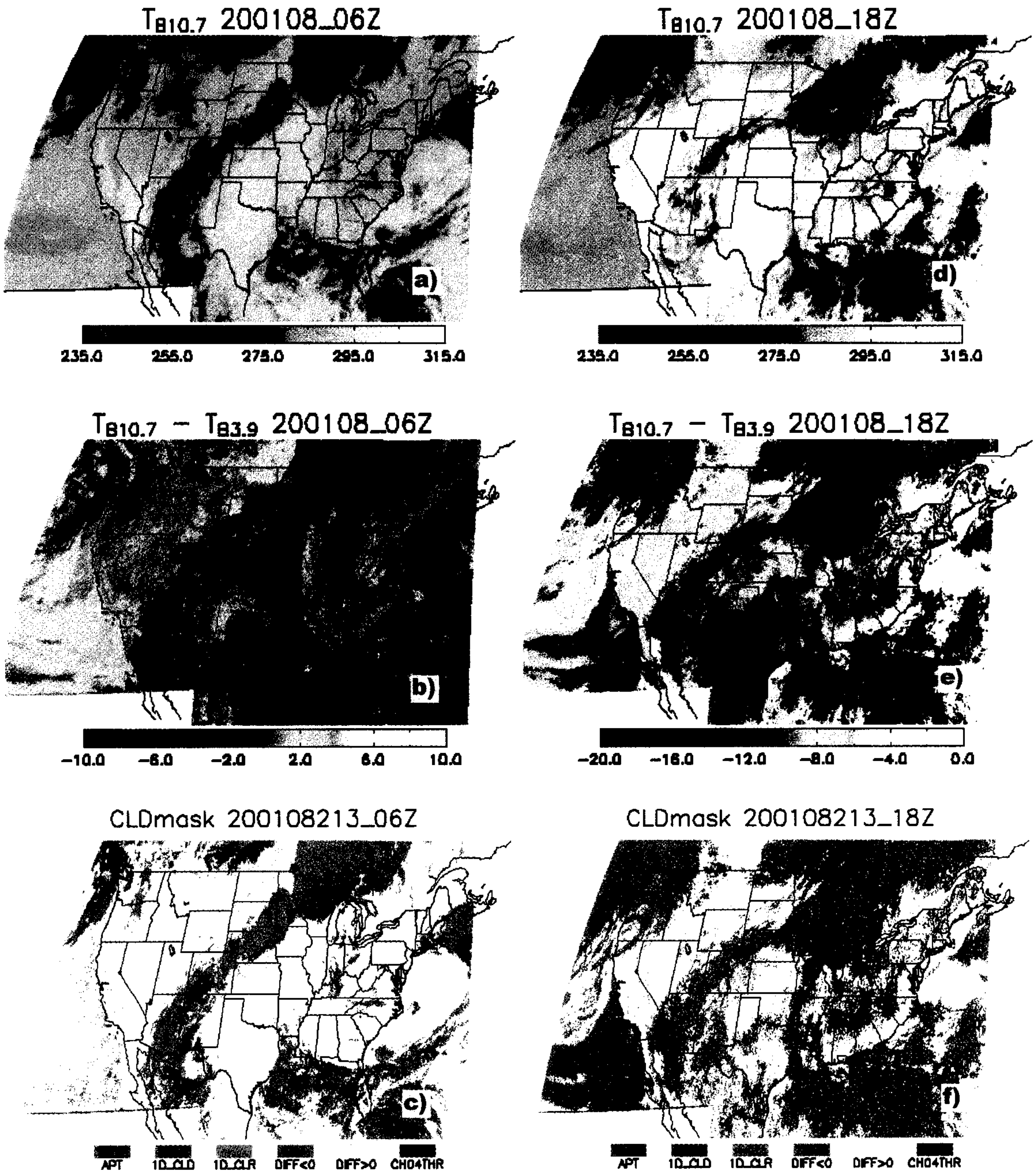

Figure 3.3: Images of brightness temperature and the cloud mask for two hours from August 01, 2001: a) 06 UTC T_B(10.7 μm) b) 06 UTC T_B(10.7 μm) - T_B(3.9 μm) difference c) 06 UTC cloud mask d) 18 UTC T_B(10.7 μm) e) 18 UTC T_B(10.7 μm) - T_B(3.9 μm) difference f) 18 UTC cloud mask.

of California, and in northern North Dakota, and western South Dakota. At night, the low water clouds are flagged in yellow by the positive difference test, and the high cold clouds are flagged by the negative difference test and the 10.7 μm threshold test. In the daytime, the negative difference test catches the majority of the clouds in the image. The cloud mask detects appreciably more cloud in parts Arkansas, Missouri, and Texas during the daytime, when the solar reflection by clouds contributes to the cloud detection scheme.

3.2 Forward Radiative Transfer Models

3.2.1 Radiative Transfer in an Emitting Atmosphere

In both the microwave and infrared spectrums, this study employs a monochromatic radiative transfer equation in an absorbing/emitting atmosphere. A thorough treatment of this problem is found in Chapter 7 of *An Introduction to Atmospheric Radiation* (Liou, 1980) and Chapter 7 of *Remote Sensing of the Lower Atmosphere* (Stephens, 1994).

The change in intensity of incident microwave or infrared radiation through a non-scattering atmospheric path (s) is proportional to the incoming intensity,

$$dL_\lambda(\text{extinction}) = -\sigma_{ext,\lambda}(s)L_\lambda ds = -\kappa_\lambda(s)L_\lambda ds \ . \tag{3.1}$$

The volume extinction coefficient, $\sigma_{ext,\lambda.}$, is a combination of absorption and scattering processes. In a cloud-cleared atmosphere, it is reasonable to assume there is no atmospheric scattering, leaving only the absorption coefficient, κ_λ. In addition to extinction, there is emission by an atmospheric layer. The lower atmosphere can be assumed to be in local thermodynamic equilibrium (Stephens, 1994), where the Planck function (a function of temperature and wavelength shown in Equation 1.1) may be used to describe the increase of radiation along the path.

$$dL_\lambda(\text{emission}) = \kappa_\lambda(s)\beta_\lambda ds \quad . \tag{3.2}$$

The sum of the extinction and emission give the net change along an atmospheric path.

The optical path, τ_λ, can be defined by the integral of the absorption coefficient, κ_λ (km^{-1}), through an atmospheric slant path from s′ to s″:

$$\tau_\lambda(s', s'') = \int_{s'}^{s''} \kappa_\lambda(s) ds . \tag{3.3}$$

Optical depth is defined with a vertical path (z), and is related to the slant path by dividing by the cosine of the zenith angle (μ)

$$ds = \frac{dz}{\mu} , \tag{3.4a}$$

$$\tau_\lambda(z', z'') = \int_{z'}^{z''} \kappa_\lambda(z) \frac{dz}{\mu} . \tag{3.4b}$$

The atmospheric transmission (Tr) is an exponential function of the optical depth τ_λ and is given by,

$$\mathrm{Tr}(z', z'') = e^{-\tau_\lambda(z', z'')} \quad . \tag{3.5}$$

At the surface boundary radiation can be transmitted, reflected, or absorbed; with the three processes summing to unity. It is assumed there is no transmission into the surface, leaving only reflection and absorption. According to Kirchhoff's Law the absorptance of a body is equal to its emittance. The emittance (ε) can then be used to derive the reflectance (R),

$$R = 1 - \varepsilon \tag{3.6}$$

Maintaining height (z) as the vertical coordinate, and using Equation 3.5 to define the slant path transmission between two heights, the upwelling Top Of the Atmosphere (TOA) spectral radiance, L_λ, can be expressed as

$$\begin{aligned} L_\lambda = \varepsilon_{\lambda,\mu}\beta_\lambda(T_{sfc})\,\mathrm{Tr}(0,\mathrm{TOA}) + \int_{z=0}^{\mathrm{TOA}} \beta_\lambda[T(z)]\frac{\partial \mathrm{Tr}(z,\mathrm{TOA})}{\partial z}\,dz + \\ (1-\varepsilon_{\lambda,\mu})\,\mathrm{Tr}(0,\mathrm{TOA})\int_{\mathrm{TOA}}^{z=0} \beta_\lambda[T(z)]\frac{\partial \mathrm{Tr}(0,z)}{\partial z}\,dz\ . \end{aligned} \tag{3.7}$$

The three terms defining the upwelling radiance, L_λ, are the contribution from the surface, the upwelling atmospheric radiation, and the downwelling atmospheric radiation reflected from the surface and transmitted through the atmosphere. Notice the limits in the atmospheric radiation terms switch for second and third terms, which define the upwelling and downwelling radiation respectively. The Planck function (Equation 1.1) defines the radiance emitted for a given temperature. The radiation from a particular level in atmosphere, $\beta_\lambda[T(z)]$, is transmitted either upward via Tr(z,TOA), or downward via Tr(0,z). The contribution by the surface, $\varepsilon_{\lambda,\mu}\beta_\lambda(T_{sfc})$, includes the spectral emissivity which is also a function of the cosine of the zenith angle (μ).

3.2.1.1 Discrete Atmospheric Transfer Model

The infrared and microwave radiative transfer is performed discretely in a stepwise manner from the top of the atmosphere, to the surface and back to space,

$$L^{\downarrow}(\mathrm{curr}) = L^{\downarrow}(\mathrm{prev})\mathrm{Tr}(\mathrm{curr}) + \beta[T(\mathrm{curr})][1-\mathrm{Tr}(\mathrm{curr})]\ , \tag{3.8a}$$

$$L^{\uparrow}(\mathrm{sfc}) = (1-\varepsilon)L^{\downarrow}(\mathrm{atm}) + \varepsilon\beta[T(\mathrm{sfc})]\ , \tag{3.8b}$$

$$L^{\uparrow}(\mathrm{curr}) = L^{\uparrow}(\mathrm{prev})\mathrm{Tr}(\mathrm{curr}) + \beta[T(\mathrm{curr})][1-\mathrm{Tr}(\mathrm{curr})]\ . \tag{3.8c}$$

Downwelling atmospheric radiance is treated iteratively summing the layers with equation 3.8a from the Top Of the Atmosphere (TOA) to the surface. The downwelling radiance at each layer, $L^{\downarrow}$(curr), is defined by the incident downwelling radiation multiplied by the layer transmission, $L^{\downarrow}$(prev)Tr(curr), which is then summed with the radiance energy of that layer, β[T(curr)], multiplied by the layer emission efficiency [1 - Tr(curr)]. At the surface interphase, the upwelling radiation from the surface, $L^{\uparrow}$(sfc), is a sum of the reflection of the downwelling atmospheric radiation, (1 - ε)$L^{\downarrow}$(atm), and the emission from the surface $\varepsilon\beta$[T(curr)]. Lastly, the incident upwelling radiation is transmitted through the atmospheric layers, $L^{\uparrow}$(prev)Tr(curr), and summed with the radiance contribution from each layer β[T(curr)][1 - Tr(curr)]. The infrared radiative transfer model was obtained from Dr. David Kratz, and validated using the MODerate resolution TRANsmittance (MODTRAN) model version 3.5. The microwave radiative transfer model was written in FORTRAN and was validated with two independent models developed by Drs. Andrew Jones and Darren McKague of the Cooperative Institute for Research in the Atmosphere (CIRA).

3.2.2 Microwave Atmospheric Extinction

Dry air attenuation, the water vapor continuum, and absorption lines due to oxygen and water vapor dominate the microwave extinction in the frequency range of 10 – 89 GHz. The absorption coefficients in the microwave are retrieved with the millimeter-wave propagation (MPM) model based on that of Liebe (1985), MPM85. The newer model used is MPM93, and includes improved water vapor continuum (Liebe, 1987; Liebe and Layton, 1987, and Liebe, 1989), water vapor absorption lines (Liebe, 1989), line mixing coefficients for dry air (Liebe et al. 1992), and an approximation for Zeeman (O_2) and Doppler (H_2O) line-broadening to cover heights up to 100 km (Hufford and

Liebe, 1989). The temperature and moisture profiles from the numerical weather model analysis, along with assumption of well-mixed oxygen are used in MPM93 to generate the extinction coefficients.

3.2.3 Infrared Atmospheric Extinction

The primary absorbing gases in the infrared spectral interval 9.8 – 11.5 μm (the width of GOES channel 4 spectral response) are ozone, carbon dioxide, and water vapor. The US standard atmosphere profile of ozone is used for all cases. Carbon dioxide is set to 370 ppmv at the surface, and falls off logarithmically to 360 ppmv by 100 hPa following the measurements of Schmidt and Khedim (1991). A correlated k-distribution model developed by Dave Kratz (1995) is used to calculate the extinctions coefficients for the gases at the infrared wavelengths. The correlated k-distribution methodology begins with a line-by-line model to resolve the absorption lines for a particular gas at a standard temperature and pressure. Over the spectral width of typical infrared sensors, many absorption coefficients share similar values. Computation efficiency is dramatically improved if the integration over wavenumber is transformed to an integration over the probability distribution function (k-distribution) of the absorption coefficient (Liou, 1992). To extend this method beyond the standard temperature and pressure, Lacis et al. (1979) proposed to correlate the probability distribution to any pressure and temperature encountered in the atmosphere. The correlated k-distribution of Kratz also includes a wavelength-dependant empirical formula of Roberts et al. (1976) to account for absorption by the water vapor continuum.

3.3 Land Surface Temperature Retrieval

The land surface temperature is the variable with the largest impact on the resulting microwave land emissivity. In addition, a single value that is representative of a one-half degree horizontal scale is difficult to determine. The RUC model reports a 2-meter shelter temperature and land surface temperature; however, the RUC land surface model was not fully operational for the time period of our study making the RUC land surface temperature unreliable over the time period of the study (values were often not reported, or the same value was reported repeatedly for several analysis times). To calculate a land surface temperature, GOES infrared brightness temperatures are matched to calculated brightness temperatures using RUC profiles of moisture and temperature in a plane parallel infrared radiative transfer scheme. The extinction coefficients in the infrared are approximated using a correlated k-distribution. A spectral reflectance library is indexed to a soil and vegetation database to create a map of infrared land emissivity, with static values unique to each grid point.

3.3.1 Infrared Emissivity Atlas

The infrared land emissivity is more stable over time than the microwave land emissivity (Wan, 1999). For the purposes of this study the infrared emissivity is assumed fixed over the time period. The infrared land emissivity is estimated by the soil and vegetation at a particular location. The John Hopkins University spectral library provides measurements of directional hemispheric spectral reflectance for a variety of soils and a few vegetation classifications. Neglecting infrared transmission into the soil and vegetation, the absorption and reflection must sum to one. Kirchoff's Law (Equation 3.1) is used to retrieve the emissivity from the directional hemispherical reflectance measurements.

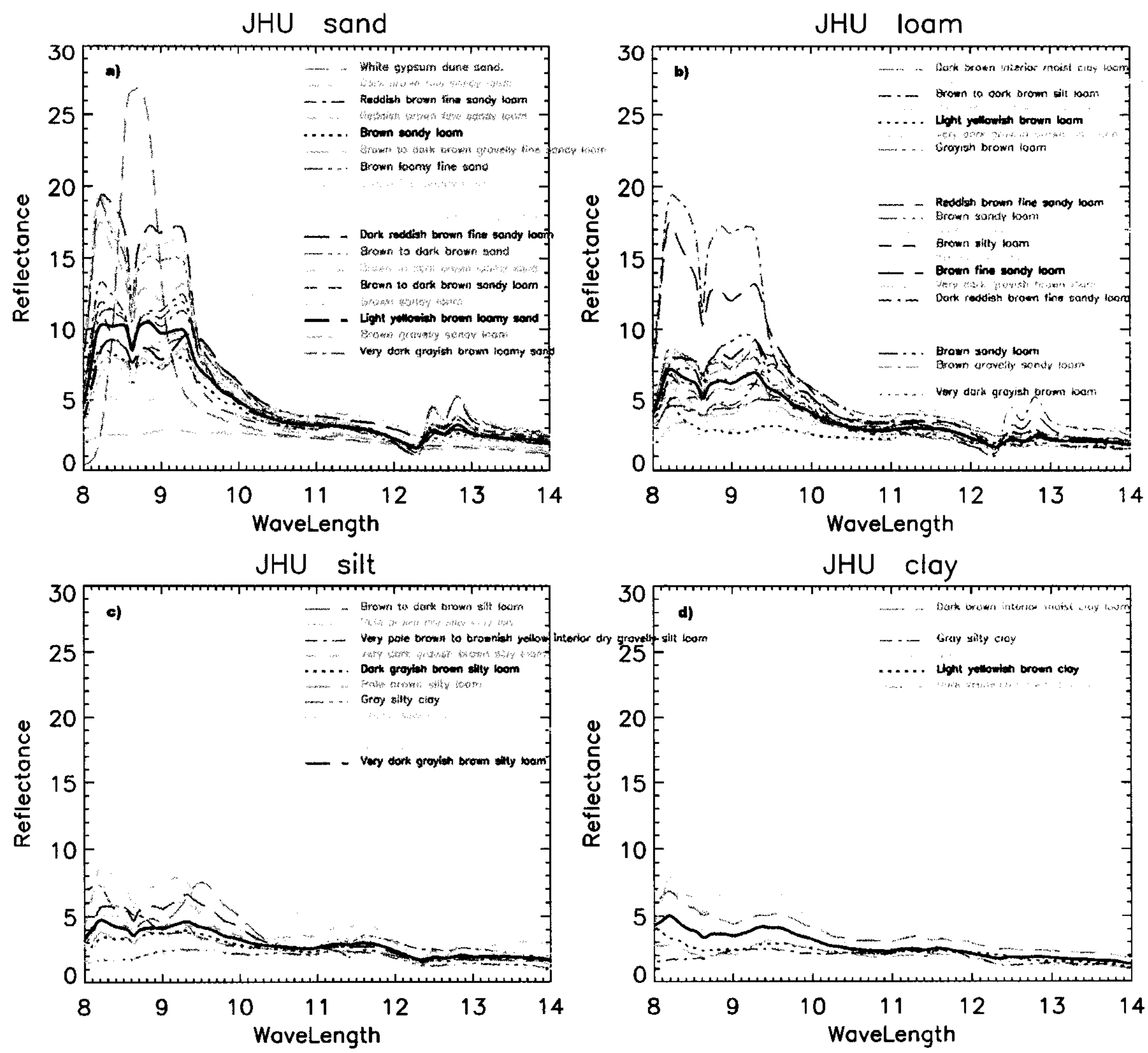

Figure 3.4: The spectral reflectances of 41 soil samples (Salisbury and D'Aria, 1992) grouped by sample class and subclass, with soil category means indicated by heavy black line. The range of the GOES 10.7 μm spectral response function is indicated by the shaded area. Soil categories shown are a) sand, b) loam, c) silt, and d) clay.

There are 41 total soil samples in the John Hopkins University reflectance library, which where grouped into four broad classifications: sand, loam, silt, and clay. The class or subclass, are used in the titles of the samples, and are the basis on which the 41 samples are grouped into the four categories. A sample can thus be in two different categories if it has both a class and a subclass. Figure 3.4a and 3.4b show reflectance measurements from the sand and loam samples. The most prominent features are the quartz reststrahlen doublet in the 8 – 10 μm range, and the alpha-quartz doublet centered about 12.6 μm. Figure 3.4c and 3.4d show reflectance measurements from the loam and silt samples, which exhibit a broad peak about 11.7 μm attributed to organic matter. A common assumption made to infrared emissivity is that soils exhibit graybody behavior (constant emissivity with wavelength) these samples show the silt and clay approach this behavior, but this assumption could not be used to describe the bulk of the soil samples.

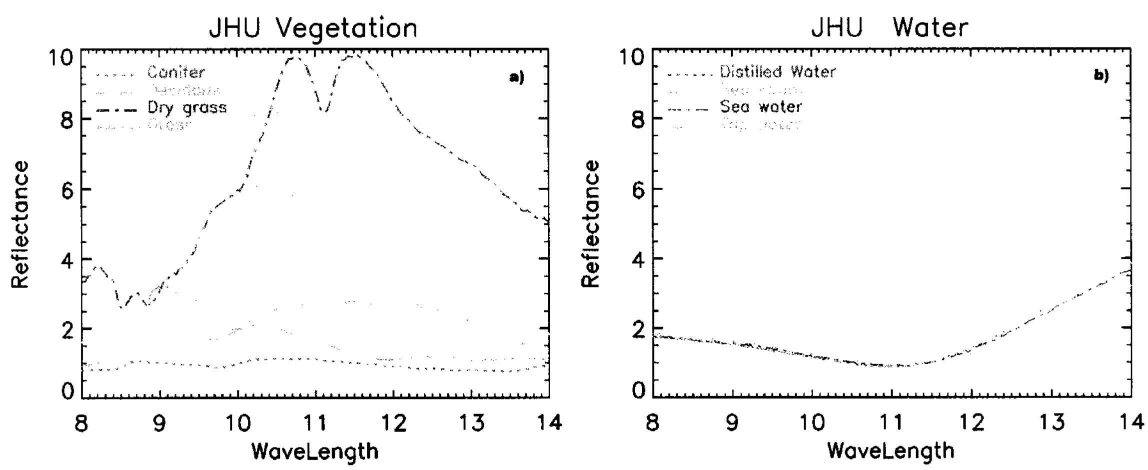

Figure 3.5: The spectral reflectances of a) 4 vegetation samples, and b) 4 water samples (Salisbury and D'Aria, 1992). The range of the GOES 10.7 μm spectral response function is indicated by the shaded area.

There are four different vegetation samples in the library: conifer, deciduous, grass, and dry grass. Figure 3.5a displays the vegetation samples, where the conifer is a near gray body, with reflectance values consistently between 1 and 2 percent. The dry grass sample shows a strong impact of senescence on a grass sample. This highlights the fact that for a short time period the infrared emissivity may be relatively stable, but seasonal effects would need to be taken into account for an infrared land emissivity look-up table that could be used year round. There are also four water types in the library; however, tap water is used for all water bodies. Figure 3.5b shows the reflectance measurements of the four water samples, the small variations between the different water types produce a small enough change in the integrated spectral reflectance, less than 1%, that the single spectrum is adequate.

Table 3.1: Soil reflectance spectrum from John Hopkins University library (Salisbury and D'Aria, 1992) used for each of the 16 soil classifications of Miller and White (1998).

Category	Classification	JHU spectrum
1	Sand	Sand Avg
2	Loamy sand	Sand Avg
3	Sandy loam	Sand Avg
4	Silt loam	Silt Avg
5	Silt	Silt Avg
6	Loam	Loam Avg
7	Sandy clay loam	Clay Avg
8	Silty clay loam	Clay Avg
9	Clay loam	Clay Avg
10	Sandy clay	Clay Avg
11	Silty clay	Clay Avg
12	Clay	Clay Avg
13	Organic materials	Avg (all soils)
14	Water	Tap Water
15	Bedrock	Avg (all soils)
16	Other	Avg (all soils)

This library is indexed to soils and vegetation over the CONUS using the soil and vegetation databases described in section 2.4. Table 3.1 describes which of the four averages (sand, silt, loam, or clay) are used for each soil type. Table 3.2 describes the procedure for matching the vegetation spectra to the vegetation database. The forest classifications are straightforward. The use of the dry grass vegetation sample is reserved for the driest vegetation classifications: closed shrubland, open shrubland, and grassland. The vegetation database identifies these three classifications in the western high plains, and to the west of the Rocky Mountains. Figure 3.6 shows the resulting infrared land emissivity look-up table normalized by the spectral response function of channel 4 (10.7 μm) from GOES-10 west of 105W, and GOES-08 east of 105W.

Table 3.2: Reflectance spectrum from John Hopkins University library (Salisbury and D'Aria, 1992) used for each of the 14 AVHRR derived vegetation classifications of Hansen et al. (2000).

Category	Classification	JHU spectrum
1	Water & Goode's Interrupted Space	Tap Water
2	Evergreen Needleleaf Forest	Conifer
3	Evergreen Broadleaf Forest	Conifer
4	Deciduous Needleleaf Forest	Deciduous
5	Deciduous Broadleaf Forest	Deciduous
6	Mixed Cover	1/3 Conifer; 1/3 Deciduous; 1/3 Grass
7	Woodland	1/2 Conifer; 1/2 Deciduous
8	Wooded Grassland	1/2 Grass; 1/4 Conifer; 1/4 Deciduous
9	Closed Shrubland	3/8 Dry Grass; 1/4 Conifer; 1/4 Deciduous; 1/8 Grass
10	Open Shrubland	5/8 Dry Grass; 1/8 Conifer; 1/8 Deciduous; 1/8 Grass
11	Grassland	7/8 Grass; 1/8 Dry Grass
12	Cropland	1/2 Deciduous; 1/2 Grass
13	Bare Ground	Weighted soil spectra using
14	Urban and Built-Up	Average (Soil, Conifer, Deciduous, Grass, Dry Grass)

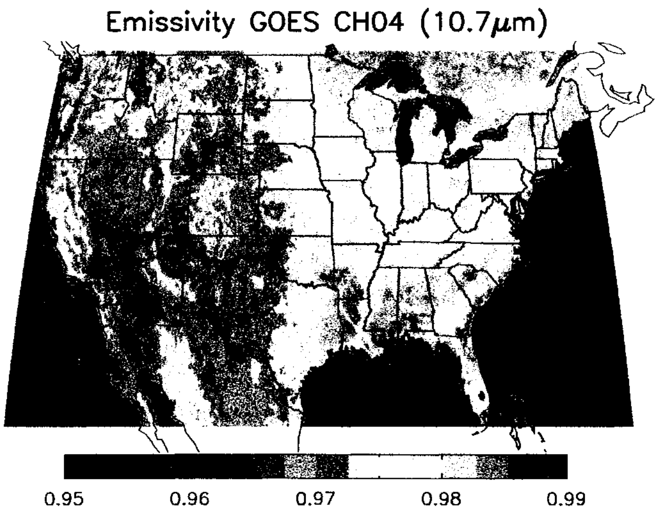

Figure 3.6: Infrared land emissivity look-up table normalized by the spectral response function of GOES-10 west of 105W, and GOES-08 east of 105W.

3.3.2 Iterative Approach

The GOES 10.7 μm channel will be used in the single-channel retrieval scheme. This "window" channel is the infrared channel on the GOES imager with the least gaseous atmospheric contamination. The channel is at 4 km resolution, and for each one-half degree box the cloud free $T_{B(10.7\mu m)}$ pixels are averaged. Radiative transfer calculations are performed at one wavenumber resolution from 870 – 1020 cm^{-1} (about 11.5 – 9.8 μm) to cover the spectral response of the GOES channel. RUC profiles interpolated to the one-half degree grid are used to generate the atmospheric absorption and re-emission due to carbon dioxide, water vapor, and ozone (section 3.2.3). When the radiance reaches the surface, the spectral reflectance indexed to the half-degree grid point is used to reflect the radiation, the contribution from the surface is added in and the radiation is propagated upwards through the atmosphere via Equations 3.6a-c. The spectral upwelling radiance is normalized by the spectral response function of the appropriate GOES instrument (GOES-08 east of 105W and GOES-10 west of 105W) and a brightness temperature is calculated using the channel center frequency, 10.7 μm, and the Planck function. The surface temperature is the single variable that is adjusted until the simulated brightness temperature is within 0.2 K of the average $T_{B(10.7\mu m)}$.

3.3.3 Estimation of Land Surface Temperature Error

Errors in the Land Surface Temperature (LST) affect the estimates of microwave emissivity. The infrared-based retrieval of LST is impacted by undetected cloud, and by changes in the vegetation. The undetected cloud lowers the infrared radiance and the estimate of LST, except in the case of inversion layer clouds. Changes in vegetation alter the infrared emissivity atlas (shown in Figure 3.6), with drier vegetation lowering the infrared emissivity, and more lush vegetation stabilizing the infrared emissivity at about

0.98. The impacts of 4% missed cloud cover, and changing vegetation on the LST are presented for use in emissivity error budget calculations.

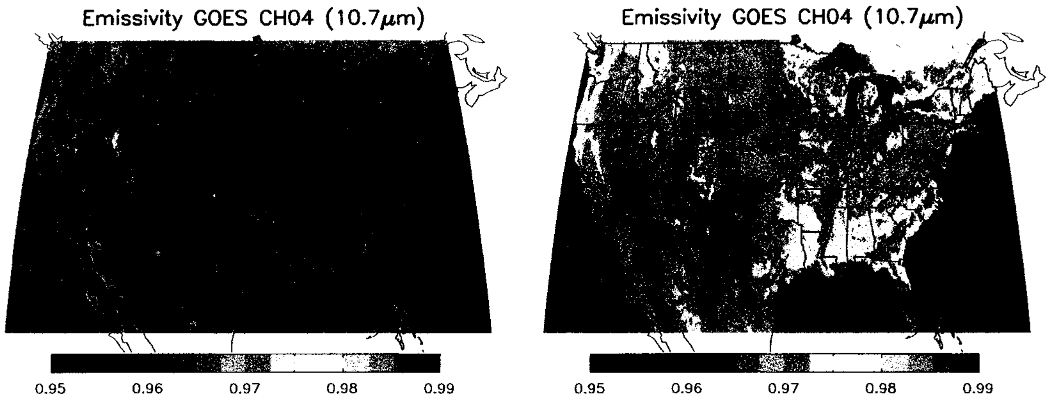

Figure 3.7: Infrared emissivity atlases simulating drier conditions by averaging dry grass into the vegetation indexed to a location. Two cases are shown: a) very dry, averaging 25% dry grass into the vegetation; b) dry, averaging 10% vegetation into the vegetation.

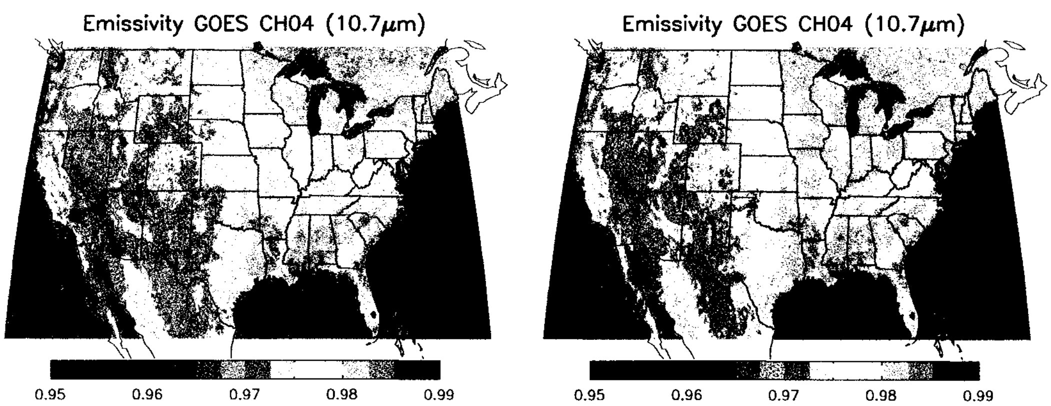

Figure 3.8: Infrared emissivity atlases simulating wetter conditions by averaging water and deciduous spectral signatures into the vegetation indexed to a location. Two cases are shown: a) lush, averaging 12.5% of both water and deciduous into the vegetation; b) very lush, averaging 25% of both water and deciduous into the vegetation.

In the mid-latitudes, non-coniferous vegetation undergoes a cycle of greening and senescence. This study chose a single season in part to avoid large changes in the vegetation. To ascertain impacts of very dry or very lush vegetation the allotment of spectral library signatures to vegetation type shown in Table 3.2 are altered in the following way. Dry conditions are simulated by averaging the spectral signature of dry grass with the spectral signature of the vegetation for a location. Very dry and dry cases are examined, with 25% and 10% dry grass added to the vegetation respectively. The new infrared emissivity atlas for these cases is shown in Figure 3.7. The impact of adding senescent vegetation is quite strong where the dry case (10% dry grass) lowers the infrared emissivity by about 0.5% and the very dry case (25% dry grass) lowers the infrared emissivity by 1% for most locations. Wet conditions are simulated by averaging the spectral signature of water and deciduous vegetation into the vegetation for a particular location. Lush and very lush cases are examined, with 12.5% water and 12.5% deciduous added to the lush case, and 25% water and 25% deciduous added to the very lush case. The infrared emissivity atlases for the lush cases are shown in Figure 3.8. The infrared emissivity tends to stabilize at a value of about 0.98 for the lush and very lush cases, lowering the infrared emissivity in heavily forested areas, and raising it in arid areas.

The LST was most dramatically impacted in the dry cases, while the lush cases had very small impacts. LST computed for the very dry case, which averaged 25% dry grass into the vegetation infrared emissivity signature had the largest difference compared to the LST computed using the original infrared emissivity atlas. The Root Mean Square (RMS) difference between the very dry and original LST was 0.5 K for about 60,000 LST retrieval cases.

Instead of simulating all possible impacts of cloud, the most dramatic cloud impact was chosen, which is due to cirrus cloud. Cirrus cloud is very cold and can be optically thin, which makes it difficult to detect. Cooper et al. (2003) made estimates of the infrared temperatures of clouds in relation to optical depth. A cloud temperature of 255 K represents an optically thick cloud (optical depth ≥ 2) at a temperature of 255 K, or a colder cloud (225 K) with optical depth of 0.5. The 255 K limit should be adequate as colder and/or thicker clouds with sufficient spatial coverage will be detected by the BST cloud mask. Comparisons of the Bi-Spectral Threshold (BST) cloud mask (used in the study) and the cloud mask product generated from the Moderate Resolution Imaging Spectroradiometer (MODIS) are presented in section 4.1 and reveal an average of 4% missed cloud by the BST cloud mask. This comparison did not specify the type of cloud missed. Low level or mid level water clouds would not have a radiative signature as cold as a cirrus cloud, but we will use the cirrus cloud to make an estimate of the worst-case scenario. To add the cloud into the LST retrieval the average brightness temperature used in the retrieval is assumed to come from 96% land, and 4% cloud signal. The average brightness temperature is adjusted upwards removing the cloud signal, and the LST is computed using the new "cloud free" brightness temperature. The RMS difference between the original and "cloud free" LST was 3 K, an impact six times greater than that due to changes in vegetation. Again this is a worst-case scenario with all missing cloud assumed to be cold cirrus, and the impact would lessen if the cloud were a low or mid level water cloud.

3.4 Microwave Emissivity Retrieval

3.4.1 Direct Inversion

The microwave brightness temperatures from the SSM/I sensor are interpolated to a one-half degree grid. Land surface temperatures calculated from GOES, using the approach described above, are supplied on the one-half degree grid at 3-hourly intervals. The land surface temperatures are then linearly interpolated to the time of the overpass of the particular satellite. The RUC profiles of temperature and moisture are also interpolated to the one-half degree grid. The closest 3-hourly analysis time to the satellite overpass time is used; consequently, a maximum temporal mismatch of atmospheric profile is 1.5 hours.

Microwave brightness temperatures from the AMSU sensor are not interpolated, but remain at their native resolution. The land surface temperatures calculated from GOES are interpolated in both space and time from the half-degree grid at 3-hourly intervals to the scan spot and overpass time of the AMSU sensor. The RUC nearest neighbor atmospheric profile, spatially and temporally, is chosen for the AMSU land emissivity calculation. These calculations of AMSU land emissivity are used along with a one-dimensional variational analysis and the NOGAPS model to retrieve profiles of temperature and moisture, as well as new estimates of microwave land emissivity.

In the direct inversion, the only variable that will be allowed to vary is the microwave land surface emissivity. The radiative transfer in the microwave spectrum is performed beginning with cold space and propagating to the surface as described in section 3.2. The radiances in the radiative transfer calculations are converted simply to temperature via the Rayleigh-Jeans approximation,

$$\begin{gathered}\beta_\lambda(T) = \frac{2ck_B}{\lambda^4} T \ , \\ \text{speed of light} = c = 3\times10^8 \, \mathrm{m\,s^{-1}} \, , \\ \text{Boltzman's constant} = k_B = 1.38\times10^{-23} \, \mathrm{J\,K^{-1}} \, ,\end{gathered} \tag{3.9}$$

which is an approximation to the Planck function appropriate at microwave frequencies. The Rayleigh-Jeans approximation shows that the microwave radiance at a particular wavelength is linearly proportional to temperature. The microwave land emissivity at each channel is iterated until the simulated brightness temperature matches that recorded by the microwave sensor. When the difference between simulated and satellite observed brightness temperatures is less than 0.5 K the emissivity estimate varies by less than 0.1% for frequencies less than 85 GHz and less than 0.25% for the

85 GHz frequencies. When the difference between simulated and observed is less than 0.25 K the emissivity estimate varies by less than 0.1% for all frequencies.

1.4.1.1 Error Budget

An error budget is created using uncorrelated errors in instrument noise, atmospheric transmission (error in profiles of temperature and moisture), and land surface temperature. In Chapter 7 of *Remote Sensing of the Lower Atmosphere*, Stephens (1994) presents a common simplification to the radiative transfer equation in the microwave spectrum. In this simplification, a non-scattering atmosphere is assumed and water vapor absorption is confined to the boundary layer:

$$T_B \approx \varepsilon T_S e^{-\tau_A} + (1-\varepsilon)(1-e^{-\tau_A})T_S e^{-\tau_A} + (1-e^{-\tau_A})T_S \quad . \tag{3.10}$$

The brightness temperature is computed using the microwave land surface emissivity (ε) and the land surface temperature T_S, transmitted through the atmosphere via $e^{-\tau_A}$. The lower atmosphere is approximated as isothermal, and the water vapor temperature is accordingly equal to the surface temperature. The second term is the reflection, 1 - ε, of downwelling atmospheric radiation retransmitted through the atmosphere via $e^{-\tau_A}$. The final term is the upwelling radiation from the atmosphere. To make a minimum estimate of uncorrelated error, Equation 3.10 is rearranged with respect to emissivity. The error contribution from brightness temperature (T_B) noise, atmospheric transmission, and land surface temperature can be made by taking the derivative of the emissivity with respect to each parameter (x_i), and multiplying the square of this derivative by the square of the parameter error (σ_{X_i}). The square root of the sum of these independent errors gives an estimate of emissivity error (σ_ε),

$$\sigma_\varepsilon \approx \left[\sum_{i=1}^{N} \left(\frac{\partial \varepsilon}{\partial x_i} \right)^2 \sigma_{x_i}^2 \right]^{\frac{1}{2}} . \qquad (3.11)$$

The observation (T_B) errors are taken from the instrument specifications, the transmission error is conservatively estimated at 20%, and the land surface temperature error is estimated at 5 K. This uncorrelated microwave emissivity error can be thought of as minimum estimate of error. The mean values used in this error budget analysis are shown in Table 3.3, and the resulting error budget as a percent of a mean value (0.95) in Table 3.4. The land surface temperature error dominates this estimate of error, and the values exceed 2% for all frequencies. The error is about 2.5 % for the 19 and 37 GHz frequencies, while it raises to 4 % for 22 GHz, and nearly 5 % for 85 GHz.

Table 3.3: Mean values of brightness temperature (T_B), transmission, land surface temperature (T_S), along with their errors used in the microwave land emissivity error budget analysis.

	19V	19H	22V	37V	37H	85V	85H
$\overline{T}_B$ (K)	285.1	278.2	284.0	281.8	276.3	283.5	280.5
$\overline{e^{-\tau_A}}$	0.878	0.878	0.698	0.854	0.854	0.642	0.642
$\overline{T}_S$ (K)	293.8	293.8	293.8	293.8	293.8	293.8	293.8
σ_{T_B} (K)	0.5	0.5	0.65	0.35	0.35	0.55	0.55
$\sigma_{e^{-\tau_A}}$	$0.2 \times (1 - e^{-\tau_A})$						
σ_{T_S} (K)	5						

Another estimate of error is performed using perturbations on 14,000 retrieval cases. In these cases the emissivity is retrieved, then errors are added to the model profiles of temperature and moisture (based on values supplied by Benjamin et al. [2003, in press]), and the emissivity is retrieved again. The atmospheric profiles are returned to an unaltered state, and the land surface temperature is then perturbed and the emissivity retrieved.

To create temperature profile perturbations, three random values are generated between –1 and 1. These are fixed to heights of 0, 4, and 8 km and multiplied by error terms of 4, 1.8, and 1 K respectively. These errors are then interpolated to the profile heights, and added to the profile. The moisture perturbations again utilize random values between –1 and 1. These are fixed to heights of 0, 1, and 2.5 km and multiplied by relative humidity errors of 10, 25, and 40 percent. These errors are then added to the profile. The random land surface temperature perturbation has values ranging from –5 to 5. The brightness temperature error from the previous analysis is used as an estimate of instrument error for this analysis. Table 3.5 shows the average emissivity differences expressed as percent values. The change in emissivity due to perturbed land surface temperature still dominates this analysis as well; however, both the transmission and land surface temperature contributions are less than in the previous error budget analysis. The coupling of the surface temperature to the atmosphere in the previous error budget accentuates the effect it has on the values in Table 3.4. It is important to remember however, that the emissivity differences shown in Table 3.5 are the mean values. The maximum differences due to temperature perturbation did grow to values of 5 % for the low frequencies and 7.5 % for the 85 GHz channels. Based on these analysis a conservative error estimate of 5 % can be made for all frequencies; while an optimistic estimate would have errors of less the 2 % at the frequencies less than 85 GHz.

Table 3.4: Estimate of microwave emissivity error in percent due to instrument noise (T_B), transmission, land surface temperature (T_S), and their uncorrelated combination total error. The estimate is made using a simplified radiative transfer equation (3.10), which assumes an isothermal profile.

	19V	19H	22V	37V	37H	85V	85H
T_B	0.233	0.233	0.478	0.172	0.172	0.478	0.478
$e^{-\tau_A}$	0.224	0.401	1.246	0.403	0.587	1.983	2.559
T_S	2.255	2.201	3.555	2.356	2.311	4.188	4.144
total error	2.278	2.249	3.797	2.397	2.389	4.659	4.894

Table 3.5 Average difference in calculated emissivity expressed as a percent value, due to perturbations of land surface temperature and model profiles of temperature and moisture for 14000 cases.

	19V	19H	22V	37V	37H	85V	85H
T_B	0.233	0.233	0.478	0.172	0.172	0.478	0.478
$e^{-\tau_A}$	0.100	0.158	0.330	0.138	0.189	0.696	0.876
T_S	1.242	1.204	1.505	1.255	1.232	1.698	1.674
total error	1.268	1.237	1.613	1.274	1.258	1.896	1.949

The procedure to estimate land surface temperature errors in section 3.3.3 was also used to find the impact of cloud and vegetation changes on the microwave emissivity. Table 3.4 and 3.5 show the 85H GHz channel has the largest total error, and this channel also exhibited the largest emissivity response due to changing vegetation and cirrus cloud. The response of the 85H GHz emissivity to changes in vegetation and cloud are shown in Figure 3.9a and Figure 3.9b respectively. Note the very dry case has the largest impact on the retrieved microwave emissivity, which is not surprising since it has the largest impact on the LST. The impact of cirrus cloud on the microwave emissivity is an order of magnitude greater than that due to vegetation changes. Also a mean emissivity change between 1 – 2 % is seen, which is consistent with the microwave emissivity error estimate due to land surface temperature shown in Table 3.5.

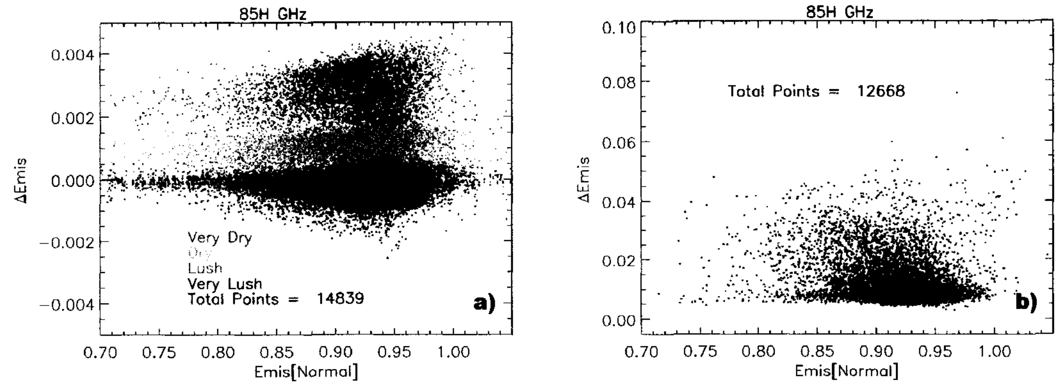

Figure 3.9: The change in 85H GHz microwave emissivity due to changes in vegetation and cirrus cloud contamination. Shown in Figure 3.9a is the emissivity change for ~15,000 cases due to vegetation ranging from very dry to very lush. Shown in Figure 3.9b is the emissivity change for ~13,000 cases due adding a 4% cirrus cloud radiating at 255 K.

3.4.2 Optimal Estimation

In this treatment of the optimal estimation problem, the 7 emissivity values, one for each of the SSM/I channels are retrieved for select case studies. A climatology from the direct retrival is used to compute the *a priori* (x_a) emissivities and their covariance S_a. In the initial iteration, the first guess emissivity is a directly retrieved value.

The observational error covariance, S_y, is the estimated noise at each of the seven frequencies, and includes error from satellite radiance noise, as well as, model errors. Multiple perturbations of the temperature profiles, moisture profiles, and emissivities are used to determine the forward radiative transfer model (F) sensitivity to errors in these parameters. A single control case assumes no vertical correlation in the temperature and moisture perturbations. The subsequent computation of S_y use vertically correlated perturbation profiles. To create vertically correlated perturbations, five random normalized perturbation values are generated at 0, 1, 4, 8, and 12 km. These normalized perturbations are interpolated to the profile heights, and multiplied by corresponding noise values. One hundred iterations are used to find the final observation error covariance values, S_y.

This optimal estimation retrieval is used to examine the ability to retrieve 85 GHz emissivity using the *a priori* knowledge, and correlation to the lower frequency channels. Retrievals are repeated for the same cases; excluding the 85 GHz channels from the observation vector, and from the observational error covariance S_y leaving five channels remaining in these parameters. The retrieval relies solely on the *a priori* data, and their cross correlations contained in S_a. This attempts to simulate conditions when the surface may be obscured at 85 GHz by cloud scattering; while the surface contribution at the lower frequencies lower frequencies remains adequate to retrieve their emissivity. Being able to infer the higher frequency emissivity, would allow a better quantification of the atmospheric scattering effects, and in turn better estimation of atmospheric quantities.

3.4.2.1 Optimal Estimation Procedure

The optimal estimation problem seeks to answer the question: what is the probability density function of our desired retrieval variable, x (for our case the microwave emissivity), given measurements y_{obs} (the microwave brightness temperatures).

The climatology of directly retrieved emissivities form an array of background values, x_{bkgnd}, with samples N. These background values are used to create the *a priori*, x_a (which is taken to be the mean value), and the covariance, S_a. The diagonal elements of S_a describe the variance for each frequency while the off diagonal elements are the covariances between the frequencies given by

$$S_a = \frac{1}{N}\left((x_{bkgnd} - x_a)(x_{bkgnd} - x_a)^T\right). \tag{3.12}$$

The probability density function P(x), gives the probability that the true value of x lies within dx of the estimated value $\hat{x}$. Rodgers (1976) proposed the assumption of Gaussian error statistics, which allows the probability density function P(x) to be written as

$$P(x) = \exp\left[-\frac{1}{2}(x - x_a)^T S_a^{-1}(x - x_a)\right] . \tag{3.13}$$

The probability density function P(y) is the probability a simulated measurement y lies within dy of the true measurement y_{obs}. The forward model, described in section 3.2, is used to create simulated observations in the microwave within uncertainty err_y,

$$y = F(x,b) + err_y . \tag{3.14}$$

The forward model (F) input includes emissivities, x, and the background fields, b (land surface temperature, and profiles of temperature and moisture). A conditional probability density function P(y|x), is the probability of an observation given a distribution of state variables. The conditional probability density function P(y|x), is found using this forward model and the measurement error covariance S_y,

$$P(y \mid x) = \exp\left[-\frac{1}{2}(y - F(x,b))^T S_y^{-1}(y - F(x,b))\right] . \tag{3.15}$$

Our desired quantity P(x|y), is the posterior pdf of the retrieval variable when the measurement is given. Bayes' theorem, named after Thomas Bayes (1702-1761), relates the posterior pdf desired, P(x|y), to the probabilities P(x), P(y), and the conditional probability P(y|x),

$$P(x \mid y) = \frac{P(y \mid x)P(x)}{P(y)} . \tag{3.16}$$

Equations 3.13 and 3.15 can now be inserted into Bayes' theorem, neglecting the normalization by P(y), to find P(x|y), the posterior pdf of the state when the measurement is given,

$$P(x \mid y) = \exp\left[-\frac{1}{2}\left[(y - F(x,b))^T S_y^{-1}(y - F(x,b)) + (x - x_a)^T S_a^{-1}(x - x_a)\right]\right]. \quad (3.17)$$

Equation 3.17 defines the posterior probability function, P(x|y), which is the probability of finding the desired variable x, with the given measurement, y. The desired retrieval variable, x, is the microwave emissivity at the seven SSM/I frequencies. The observations, y, are the satellite microwave brightness temperatures. The retrieval estimates of emissivity, $\hat{x}$, are taken to be where P(x|y) is a maximum. Rodgers (2000) refers to this state, $\hat{x}$, as the *maximum a posteriori* solution.

The Kernel (or Jacobian) matrix, **K**, defines the sensitivity of this forward model to perturbation in the parameter being retrieved,

$$K = \frac{\partial F}{\partial x} \, . \quad (3.18)$$

Employing the Kernel matrix we can recast the solution for $\hat{x}$ as:

$$\hat{x} = x_a + S_a K^T S_y^{-1}(y - F(x,b)) \, . \quad (3.19)$$

Following L'Ecuyer and Stephens (2002) a numerical implementation of Equation 3.19 can be used to find the zero slope of the P(x|y) distribution function (where the solution for $\hat{x}$ lies),

$$\hat{x}_{i+1} - \hat{x}_i = S_{\hat{x}}\left[K_i^T S_y^{-1}(y - F(x,b)) + S_a^{-1}(x_a - x_i^{-1})\right] . \quad (3.20a)$$

$$S_{\hat{x}} = \left(S_a^{-1} + K_i^T S_y^{-1} K_i\right)^{-1} \quad (3.20b)$$

Here $S_{\hat{x}}$ is the covariance matrix of the retrieved parameters, and will be one of the most important diagnostic parameters. In our problem the retrieved parameters, 7 emissivities, is equal to the observations, 7 brightness temperature observations. To test for convergence two tests will be applied. The first test compares the number of independent variables, n_x, against the covariance weighted difference between successive emissivity estimates.

$$(\hat{x}_{i+1} - \hat{x}_i)^T S_{\hat{x}}^{-1} (\hat{x}_{i+1} - \hat{x}_i) << n_x \tag{3.21}$$

The second test will test the number of independent observations, n_y, against the covariance weighted difference between successive simulated observations,

$$S_{\hat{y}} = S_y \left(\hat{K} S_a \hat{K}^T + S_y\right)^{-1} S_y \ , \tag{3.22}$$

$$\left[F(\hat{x}_{i+1}, b) - F(\hat{x}_{i+1}, b)\right]^T S_{\hat{y}}^{-1} \left[F(\hat{x}_{i+1}, b) - F(\hat{x}_{i+1}, b)\right] << n_y \ . \tag{3.23}$$

The test in Equation 3.21 is more appropriate when $n_x \leq n_y$, and the test in Equation 3.23 more appropriate when $n_y \leq n_x$ (Rodgers, 2000). In our problem we have no reason to believe n_x or n_y will dominate the other, so both convergence criterion will be used.

3.4.2.2 Optimal Estimation Diagnostics

Four primary pieces of information will be used to diagnose the performance of the optimal estimation routine. The first of these is the covariance matrix of the retrieved parameters, $S_{\hat{x}}$, shown in Equation 3.20b. The diagonal elements give an estimate of the variance of the retrieved parameters. The $S_{\hat{x}}$ matrix includes errors from the *a priori*, model profiles, forward model, and measurements. The second diagnostic is used to determine the weighting of the *a priori* data in the final retrieval. This *a priori* weighting can be deduced using the averaging kernel, or **A** matrix, defined by

$$A = S_{\hat{x}} K_i^T S_y^{-1} K_i \ . \tag{3.24}$$

In Equation 3.24, the forward model sensitivity matrix, **K**, is used from the final interation of the retrieval. The third diagnostic is used to determine the contribution of the measurements in the final retrieval, and is defined by the matrix, $\mathbf{D}_y$,

$$D_y = S_{\hat{x}} K^T S_y^{-1} \ . \tag{3.25}$$

The fourth diagnostic is the χ^2 test, which is used to test the assumption of a Gaussian distribution of errors. Here the departures of the simulated brightness temperature from the observation are weighted by the error covariance of the observations, and the departures of the final estimate from the *a priori* is weighted by the *a priori* error covariance,

$$\chi^2 = \left(F(\hat{x},b) - y\right)^T S_y^{-1} \left(F(\hat{x},b) - y\right) + \left(\hat{x} - x_a\right)^T S_a^{-1} \left(\hat{x} - x_a\right) \ . \tag{3.26}$$

When implementing the χ^2 test the degrees of freedom must be known, or at least estimated. The independent pieces of information in the measurements can be estimated using the observation and background covariances S_a and S_y. The elements whose natural variability is less than the measurement error have a signal to noise ratio of less than unity. Rodgers (2000) does this by transforming the forward model sensitivity matrix, **K**, to $\widetilde{K}$; he states, "the number of independent measurements made to better than measurement error ... are the number of singular values of $\widetilde{K}$ which are greater than about unity." This number of singular values greater than unity will be used as our estimate of the degrees of freedom, using Rodgers (2000) definition of $\widetilde{K}$,

$$\widetilde{K} = S_y^{-\frac{1}{2}} K S_a^{\frac{1}{2}} \ . \tag{3.27}$$

4 Independent Infrared Comparisons

Two National Oceanic and Atmospheric Association (NOAA) Geostationary Operational Environmental Satellites (GOES) are used to create a three-hourly cloud mask (described in Section 3.1), and a land surface temperature retrieval (described in Section 3.3). The cloud mask is based on a method developed by Jedlovec (2003) and uses the 3.9 and 10.7 μm channels on the GOES satellite. The method uses Bi-Spectral Threshold (BST) tests and is referred to as the BST method for the remainder of this section. Comparisons of the BST cloud mask are made with the cloud mask product generated from the Moderate Resolution Imaging Spectroradiometer (MODIS). The MODIS cloud mask product is swath data at 1 km resolution and is arguably the most studied and quality controlled cloud mask product available (Ackerman, 2002).

The Land Surface Temperature (LST) is retrieved using the GOES satellite window channel at 10.7 micrometers. The GOES LST is compared to both Infrared Thermometer (IRT) measurements made at the Atmospheric Radiation Measurement (ARM) program's Southern Great Plains (SGP) site, and to the operational MODIS 5-km day/night LST algorithm (Wan, 1999).

A concern in the cloud mask and LST retrieval is temporal mismatching. The GOES BST cloud mask and LST retrieval are generated from three-hourly GOES full-disk scans; however, the microwave satellite coverage of the CONUS varies temporally. The Special Sensor Microwave Imagers (SSM/I) instruments fly aboard three polar orbiting

Defense Meteorological Satellite Program (DMSP) satellites. These satellites (F-13, F-14, and F-15) have descending CONUS overpasses roughly between 11 – 19 UTC and ascending between 21 – 05 UTC, with the satellite covering the latitudinal extent of the CONUS sector in about 6 minutes. The MODIS instrument is also aboard a polar orbiting satellite, with an ascending node about an hour after that for DMSP F-15. This implies that the temporal matching of GOES and MODIS is not exact. When comparing the MODIS cloud mask and GOES BST cloud mask, the nearest temporal neighbor from GOES is used (a maximum temporal error of 1.5 hours). When comparing the GOES and MODIS LST retrievals, the GOES LST is interpolated to the overpass time of the MODIS instrument.

4.1 Comparison of Cloud Mask

The objective of the cloud mask in this study is to find cloud free areas. Though the categorization of the cloud types, cloud heights, and other quantitative cloud information is important, it is not a goal of this study. The highest quality microwave land emissivity estimates are made in the cloud free areas, where the retrieved surface temperatures and microwave brightness temperatures are least impacted by cloud absorption and scattering not accounted for in the retrieval procedure. To focus this comparison, samples are chosen where the BST cloud mask found no cloudy pixels in a half-degree box. The fraction of cloudy MODIS pixels to total MODIS pixels are reported for each BST cloud cleared half-degree point.

The MODIS cloud mask product was obtained for 15 days spanning August 2001 and 2002 resulting in 352 files, and nearly complete coverage of the CONUS. When the BST method determines a half-degree box cloud free, the average MODIS cloud fraction is 3.9%. Included in the MODIS cloud mask are a variety of quality flags. To be overly conservative, a MODIS cloud mask was created which contains cloudy, uncertain, and undetermined pixels. The MODIS cloud fraction in this conservative case rose to 7.9% for the BST cloud free half-degree points.

A spatial distribution of the average MODIS cloud fractions is created to determine if any regional biases are identifiable, and is shown in Figures 4.1 and 4.3. Figure 4.1 shows the average MODIS cloudy pixel fraction, while Figure 4.3 shows the MODIS cloudy, uncertain, and undetermined pixel fraction. Figure 4.2 shows the spatial distribution of the co-located samples of GOES BST and the MODIS cloud mask. These figures show there is an absence of samples in New Mexico, and in the southern Rocky Mountain area. In these regions, there are very few cloud free half degree grid points from which to make the comparison. The MODIS cloudy pixel average in Figure 4.1, exhibits values less the 0.1 over most of the domain, with a problem area located in the Southeastern US along the Gulf of Mexico. The two cloud masks compare very well in both Figure 4.1 and 4.3 along the US west coast, and from the Pacific Northwest through southern California. The conservative MODIS comparison (cloudy, uncertain, and undetermined pixels) has a high cloud fraction along the Southeastern US along the Gulf of Mexico. With the addition of uncertain or undetermined pixels, these coastal areas appear potentially contaminated. Knowledge of these areas will be helpful in analysis of final microwave emissivity results. Other areas of potential contamination include regions south of Lake Michigan and Erie, northern Minnesota, and the Atlantic coast from Pennsylvania southward.

The GOES derived BST cloud mask provides an adequate estimate of cloud free conditions. Problems with undetected cloud appear to be the greatest north of the Gulfs of Mexico and California. The microwave emissivity results in these areas should be interpreted using the knowledge that undetected cloud may have contaminated the results. A sampling problem exists predominantly along the southern Rocky Mountains (southern Colorado southward into Mexico). In these regions, a low number of cloud cleared scenes are available to retrieve the microwave emissivity, and the statistics in these regions may not be robust enough for all applications.

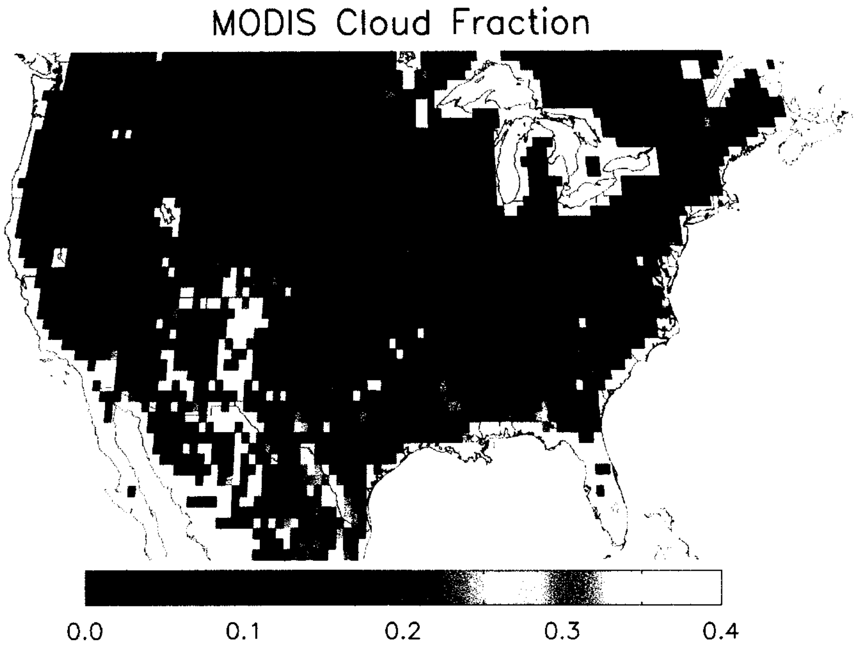

Figure 4.1: Average fraction of cloudy MODIS pixels in half-degree boxes determined cloud free by GOES based bi-spectral threshold (BST) technique adapted from that of Jedlovec (2003).

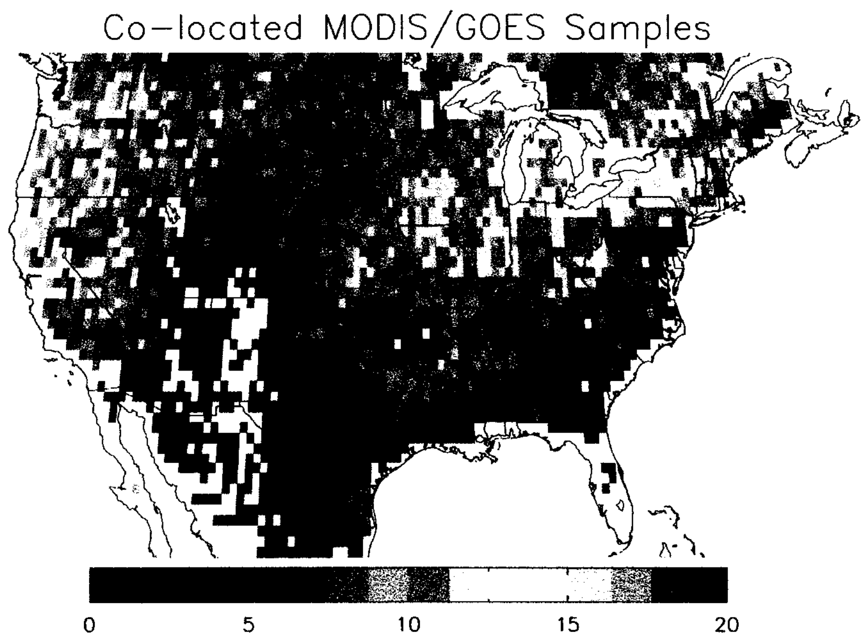

Figure 4.2: Number coincident cloud mask samples from MODIS and GOES.

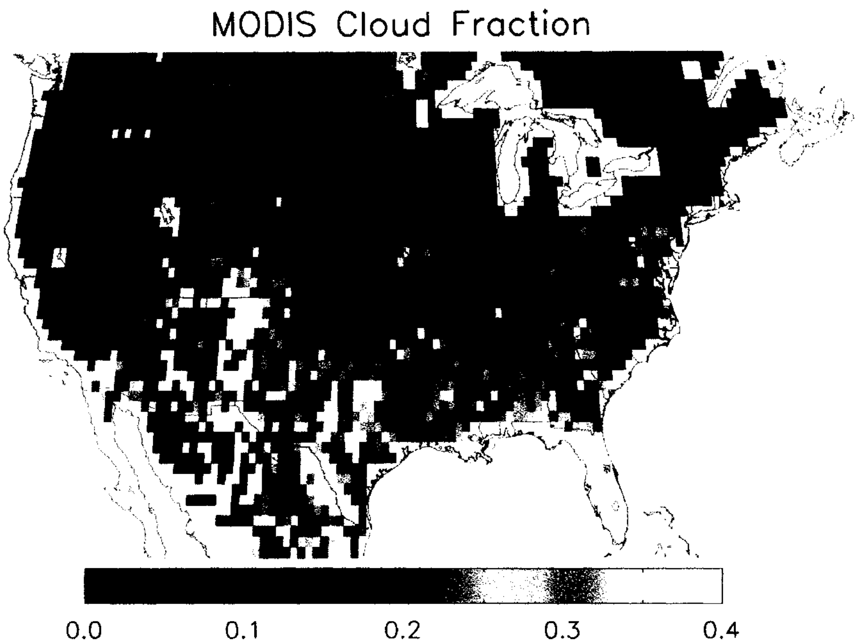

Figure 4.3: Average of MODIS pixels flagged cloudy, uncertain, or undetermined for half-degree boxes found cloud free by the GOES based bi-spectral threshold (BST) technique adapted from Jedlovec (2003).

4.2 Comparison of Retrieved Land Surface Temperature

The Land Surface Temperature (LST) is retrieved using the GOES satellite window channel at 10.7 micrometers. The GOES LST is compared to both Infrared Thermometer (IRT) measurements made at the Atmospheric Radiation Measurement (ARM) program's Southern Great Plains (SGP) site, and to the operational MODIS 5-km day/night LST algorithm (Wan, 1999).

Measurements of LST were made at the ARM-SGP site near Lamont, OK using a downward looking Infrared Thermometer (IRT). This instrument was deployed on 10 and 25 meter towers and takes measurements at 5-minute intervals. To make an estimate of a larger spatial mean the 5-minute IRT data is averaged into half-hour observations. The GOES LST is interpolated from the 3-hourly retrievals into half-hour observations and compared with the ARM-SGP IRT measurements.

The MODIS land surface temperature group has developed two LST algorithms, a generalized split-window algorithm (Wan and Dozier, 1996) and a day/night algorithm (Wan and Li, 1997). The MODIS land surface temperatures acquired are those produced using the day/night algorithm, and are reported on 5 km grid. The MODIS LST product has been validated over a combination of inland lake and vegetation sites (Wan et al., 2002). The MODIS LST product provides an independent estimate that can be objectively examined for systematic errant behavior in the retrieved GOES LST.

The ARM-SGP thermometer is compared to both the GOES and MODIS LST products. Shown in Figures 4.4a and 4.4b are differences between the GOES retrieved LST or the MODIS LST product and the LST from the 10-meter and 25-meter tower IRT respectively. Half-hour averages of LST from the IRT are subtracted from the GOES LST interpolated to half-hour times. While, the LST from the IRT is interpolated to the MODIS LST time, and this difference is plotted at the MODIS overpass time. The bias relative to the 10-meter IRT is smaller for both the GOES and MODIS LST. Also a slight diurnal signal is seen in the difference plot for the 25-meter tower. The IRT temperature is retrieved neglecting atmospheric attenuation, the diurnal signal suggests the GOES and MODIS LST are corrected for the atmosphere, which didn't affect the 10-meter temperature as greatly as it did the 25-meter. Afternoon convection prohibits retrieval of GOES LST due to cloud cover. A sampling minima occurs in the retrieved GOES LST centered at 18 UTC, 2 pm local time, this is also the time where the widest scatter is seen in the differences of GOES LST and IRT temperatures. The LST differences from MODIS show a smaller bias while a variability that is similar to that from the GOES LST; this is consistent for both the 10 and 25-meter towers.

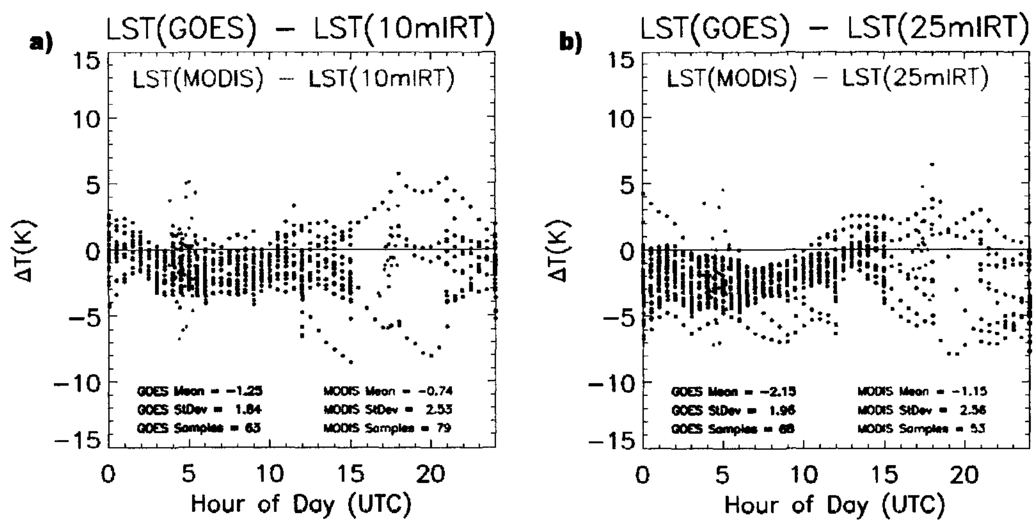

Figure 4.4: Differences of MODIS and GOES retrieved Land Surface Temperature (LST) and ARM_SGP Infrared Thermometer (IRT) mounted at a) 10-meters and b) 25-meters.

The MODIS LST product was obtained for July and August of 2001 and 2002. This product is retrieved twice a day over the majority of the globe (points of latitude greater than ~30°). The MODIS day/night LST product was obtained at 5 km resolution and is averaged to a half-degree grid. Figures 4.5 and 4.6 compare the averaged MODIS LST to the GOES retrieved LST in scatter plots for points over the CONUS. In these figures, the solid line represents the 1:1 line, and differences of 5 and 10 K about the 1:1 line are shown with dotted lines. The nighttime points are plotted in black and the daytime in blue. The bias shown is based on the $LST_{MODIS} - LST_{GOES}$ difference. Figure 4.5 shows MODIS LST that appear erroneously low for July and August in the CONUS region. Included in the MODIS LST data are a variety of quality flags. In Figure 4.6, the MODIS LST are screened using the "other" quality flag (rather than "good" quality) and the cirrus or sub-pixel cloud flag. These two flags effectively remove the low MODIS LST; however, the number of points in the daytime exceeding the GOES LST by more then 10 K increases, and both the daytime and nighttime biases shift. The MODIS LST becomes

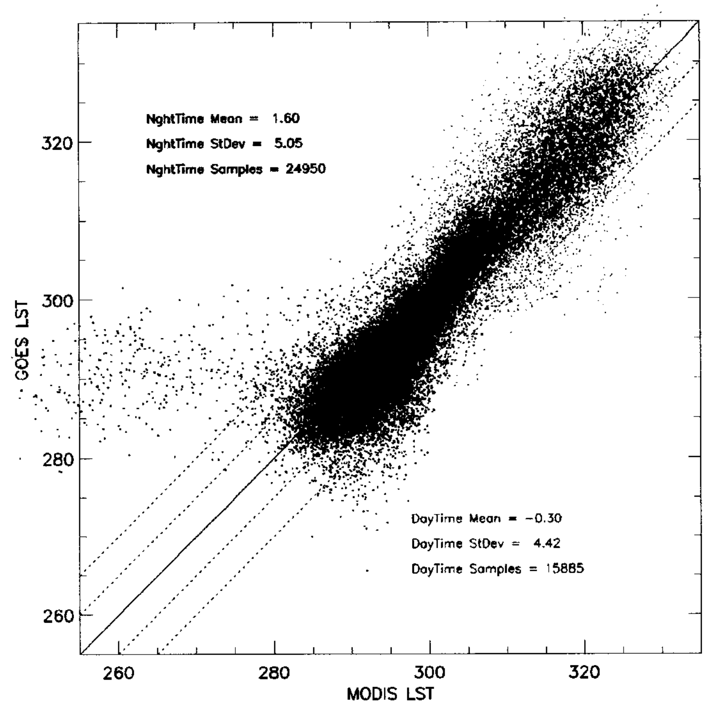

Figure 4.5: MODIS and GOES Land Surface Temperature (LST) for July and August, 2001 – 2002 over the CONUS domain. Nighttime points are shown in black, while daytime in blue.

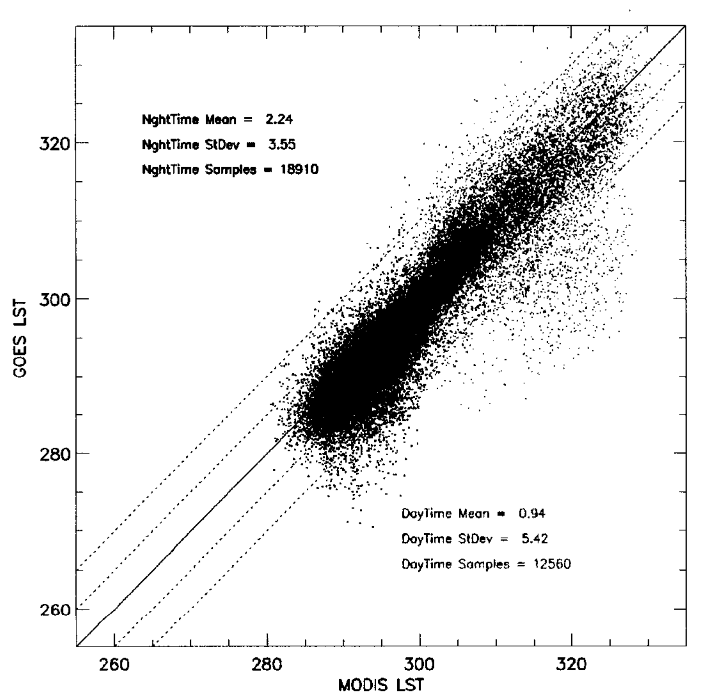

Figure 4.6: MODIS and GOES Land Surface Temperature (LST) for July and August, 2001 – 2002 over the CONUS domain. MODIS LST are screened using "other" quality flag, and cirrus or sub-pixel cloud flag. Nighttime points are shown in black, while daytime in blue.

about 0.5 K warmer for the nighttime, and about 1 K warmer for the daytime. These two plots show the majority of the comparison points lie in the ± 5 K range.

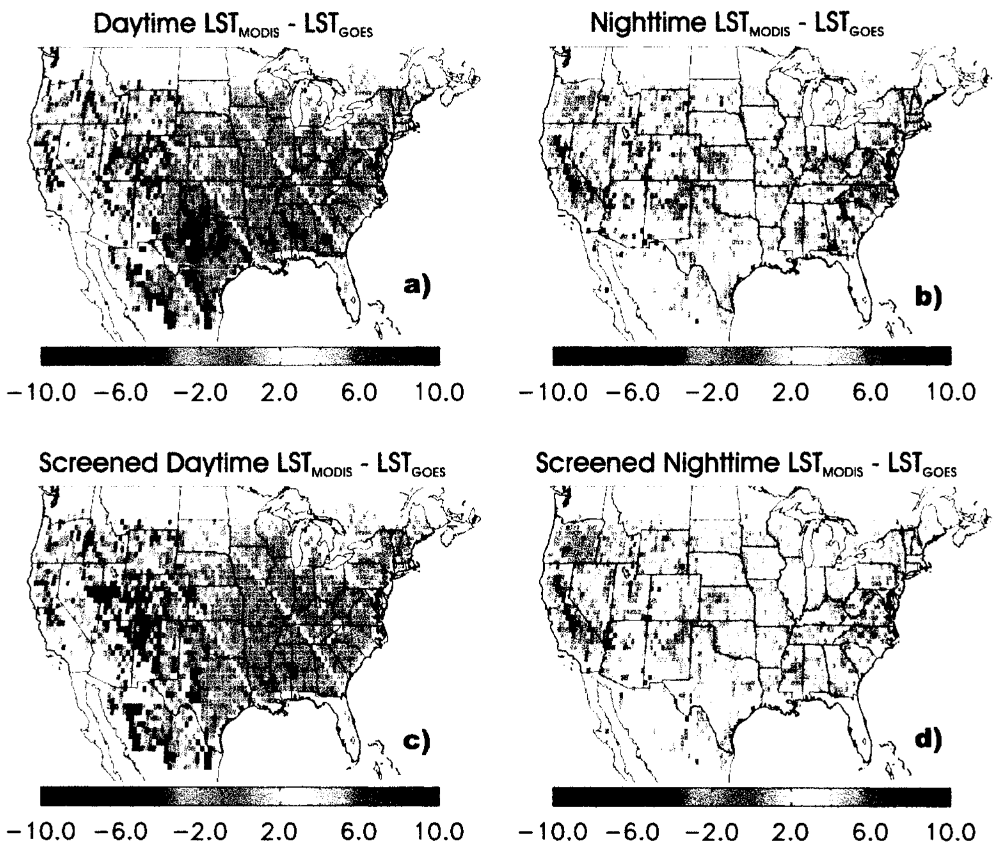

Figure 4.7: Spatial distribution of average values of LST$_{MODIS}$ - LST$_{GOES}$ values from July and August 2001 – 2002. Figures 4.7a and 4.7b use the MODIS LST with no quality control. Figures 4.7c and 4.7d use MODIS LST with the quality assurance flags corresponding to "other" quality and cirrus or sub-pixel cloud to perform "screening" on the MODIS LST data.

Spatial distributions of the average difference between the two LST data reveal that the large positive differences (warmer MODIS LST) are confined regionally. The land to the east of the Rocky Mountains have biases predominantly within a ± 5 K range. During the daytime the western plains and Great Lake states have colder GOES retrieved LST and positive differences, while the most dominant negative differences are in Southeastern US along the Gulf of Mexico and the Pacific Northwest. This could suggest inadequate correction for water vapor attenuation in the MODIS LST. At nighttime the GOES LST are consistently colder than those in the MODIS LST product, with an exception along the southern Pacific and Atlantic coasts.

Wan et al. (2002) validated both the MODIS generalized split-window, and day/night LST algorithms, focusing primarily on the split-window algorithm. To reiterate, the comparisons presented involved the day/night MODIS LST algorithm. Wan et al. (2002) found that in six rigorously cloud cleared cases over a silt playa in Railroad Valley, NV, the split-window algorithm produced LST that were a few degrees Kelvin lower than the in situ measured LST. This was attributed to an over estimation of infrared emissivity in semi-arid and arid regions. Wan et al. (2002) estimated that this over estimation of infrared emissivity lowered the resulting split-window LST by ~2.3 K. Further, Wan et al. (2002) computed the differences of day/night LST and split-window LST over the North American Continent between 20N and 50N for July 21, 2001. They found LST differences ranging from –1.96 to 8.24 K for the daytime, and –3.36 to 6.84 K for the nighttime, which are also roughly consistent with the comparisons of GOES LST and MODIS day/night LST presented above. Wan et al. (2002) maintain that the infrared surface emissivity in the split-window algorithm (which is classification-based, Snyder et al. [1998]) are overestimated in arid and semi arid regions, based on the six Railroad Valley, NV cases, and visual inspection of the distribution of MODIS day/night and MODIS split-window LST. A map of the infrared emissivities retrieved from MODIS band 31 is shown in Figure 4.8. These values are averaged over July and August of 2001, and are simultaneously retrieved with the LST values. The emissivities in the semi-arid and arid western US, are indeed lower than those used in the GOES retrieval (see Figure 3.6); however, the very low emissivities north of the Gulf of Mexico suggest contamination in the MODIS results. These areas are heavily forested and would be expected to have emissivities much closer to one. The lack of identifiable surface features in the southeast US also suggests a masking of the surface.

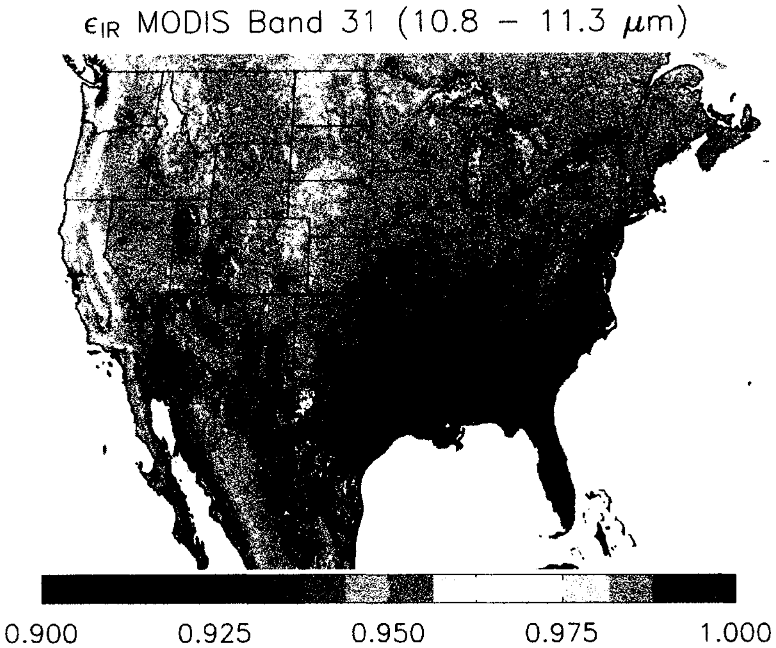

Figure 4.8: The emissivity retrieved from the MODIS day/night LST algorithm for MODIS band 31. Values are averaged over July and August of 2001.

The majority of the differences between GOES retrieved and MODIS day/night LST are constrained between $\pm$5 K. The spatial distribution of average differences show strong differences in the western US. Wan et al. (2002) found similar differences when comparing the MODIS split-window and day/night algorithms, which they attributed to an overestimation of the infrared emissivity in the split-window algorithm. When directly retrieving the microwave emissivity, an overestimation of infrared emissivity causes an overestimation of microwave emissivity as well. True validation data for satellite retrieved LST is scarce, and would help to calibrate the retrieval methods. Regrettably, the information needed to properly validate the classification-based infrared emissivity map, and the GOES retrieved LST is lacking. Interferometers with high spectral resolution can provide further LST comparison data, and improved methods for retrieving effective infrared emissivity. However, in this study it is inferred that incorrect infrared emissivities are bound to exist, and impact the retrieved microwave emissivities through the retrieval of LST.

5 Microwave Emissivity Results

This chapter examines the microwave emissivity results both overall and binned by parameters such as vegetative class. The analysis begins with a direct retrieval of microwave emissivity. This is followed by an optimal estimation of microwave emissivity at the SSM/I channel frequencies and polarizations. The direct retrieval results are used to populate variance statistics for the optimal estimation retrieval. Categorization of the data by vegetation type and fractional cover has proven to be a strong discriminator between different behaviors in the mean and variance of the microwave land emissivity. Emissivities retrieved by optimal estimation are presented along with retrieval error, contribution functions, averaging kernels, and chi-squared statistic. The optimal estimation procedure is used to retrieve microwave emissivity only, and utilizes SSM/I data, RUC profiles of temperature and moisture, and GOES derived LST. Lastly, a one-dimensional variational (1DVAR) retrieval is performed using the NOGAPS model and AMSU data. A direct retrieval of AMSU emissivities is performed over a six-month time frame, and the results are used to compute statistics for the 1DVAR retrieval. The 1DVAR retrieval estimates microwave emissivity, land surface temperature, and profiles of temperature and moisture.

5.1 Direct Retrieval

The first question asked when approaching the microwave land emissivity problem is what are typical values for emissivity, and how much do they vary? To get some answer for this question a direct emissivity retrieval is undertaken where the microwave brightness temperatures, retrieved Land Surface Temperature (LST), and model atmospheric profiles are considered "perfect."

Microwave emissivities are directly retrieved from the SSM/I sensors aboard the DMSP F-13, F-14, and F-15 satellites, and are computed for June – August of 2000 – 2002 at one-half degree spatial resolution. The Bi-Spectral Threshold (BST) cloud mask is used to estimate 100% clear conditions in each one-half degree box. The LST was retrieved using the GOES satellites, and profiles of temperature and moisture are provided by the RUC model analysis.

The ascending nodes of the three DMSP satellites are 6:13, 8:19, and 9:31 pm local time for F-13, F-14, and F-15 respectively. The descending nodes are then 6:13, 8:19, and 9:31 am local time. In a general sense, the SSM/I sensors can be viewed as having ascending passes at sunset, and descending passes at sunrise. Figure 5.1a – 5.1f shows the mean microwave land emissivity values retrieved from all three SSM/I sensors, for the ascending passes averaged over June – August of 2000 – 2002. Figure 5.2a – 5.2f shows the means from the same sensors and time period, but for the descending passes. The standard deviations from the ascending and descending overpass from all three sensors over the nine month time period are presented in Figures 5.3a – 5.3f and 5.4a – 5.4f respectively.

Some general observations of the mean values in Figures 5.1 and 5.2 can be made. One of the most obvious is that at all frequencies the microwave land emissivity is greater for the vertical polarization than the horizontal, due to the fact that the ground reflects horizontally oriented light waves more efficiently. A second general observation applies to all polarizations and frequencies. The emissivity rises with elevation, due to

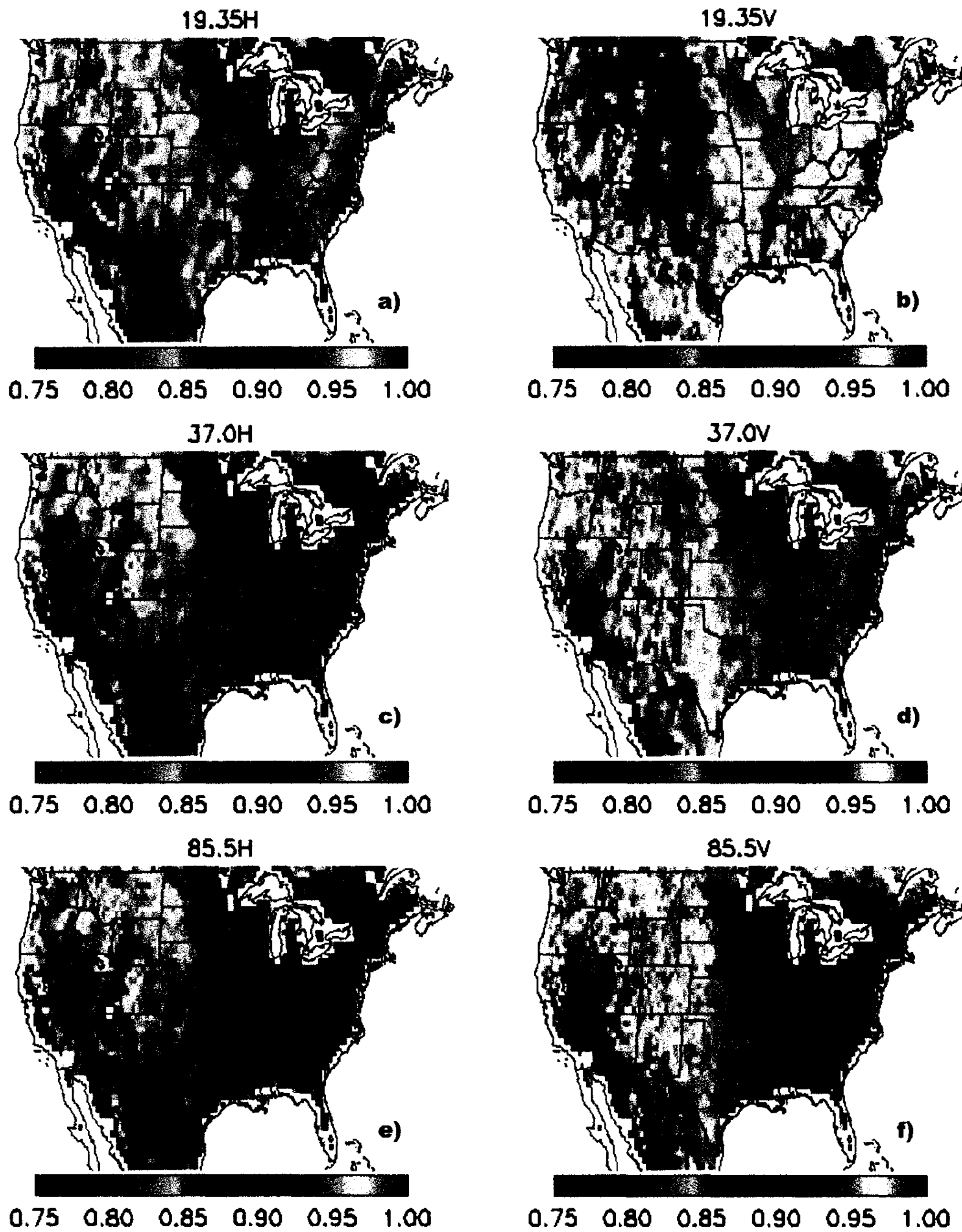

Figure 5.1: Ascending microwave land emissivity from SSM/I averaged over 9 months: June – August, 2000 – 2002, for six SSM/I channels: a) 19.35H, b) 19.35V, c) 37.0H, d) 37.0V, e) 85.5H, and f) 85.5V.

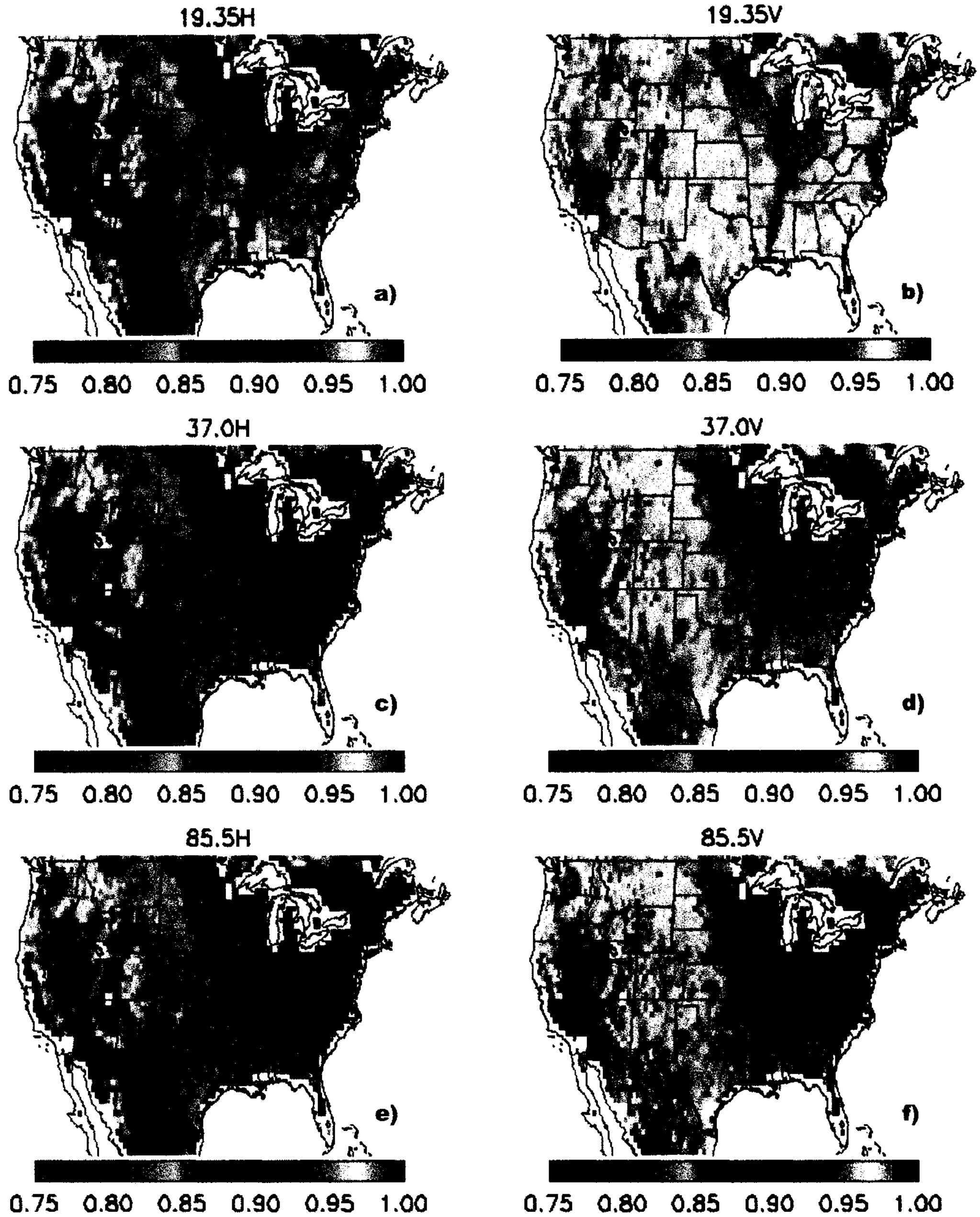

Figure 5.2: Descending microwave land emissivity from SSM/I averaged over 9 months: June – August, 2000 – 2002, for six SSM/I channels: a) 19.35H, b) 19.35V, c) 37.0H, d) 37.0V, e) 85.5H, and f) 85.5V.

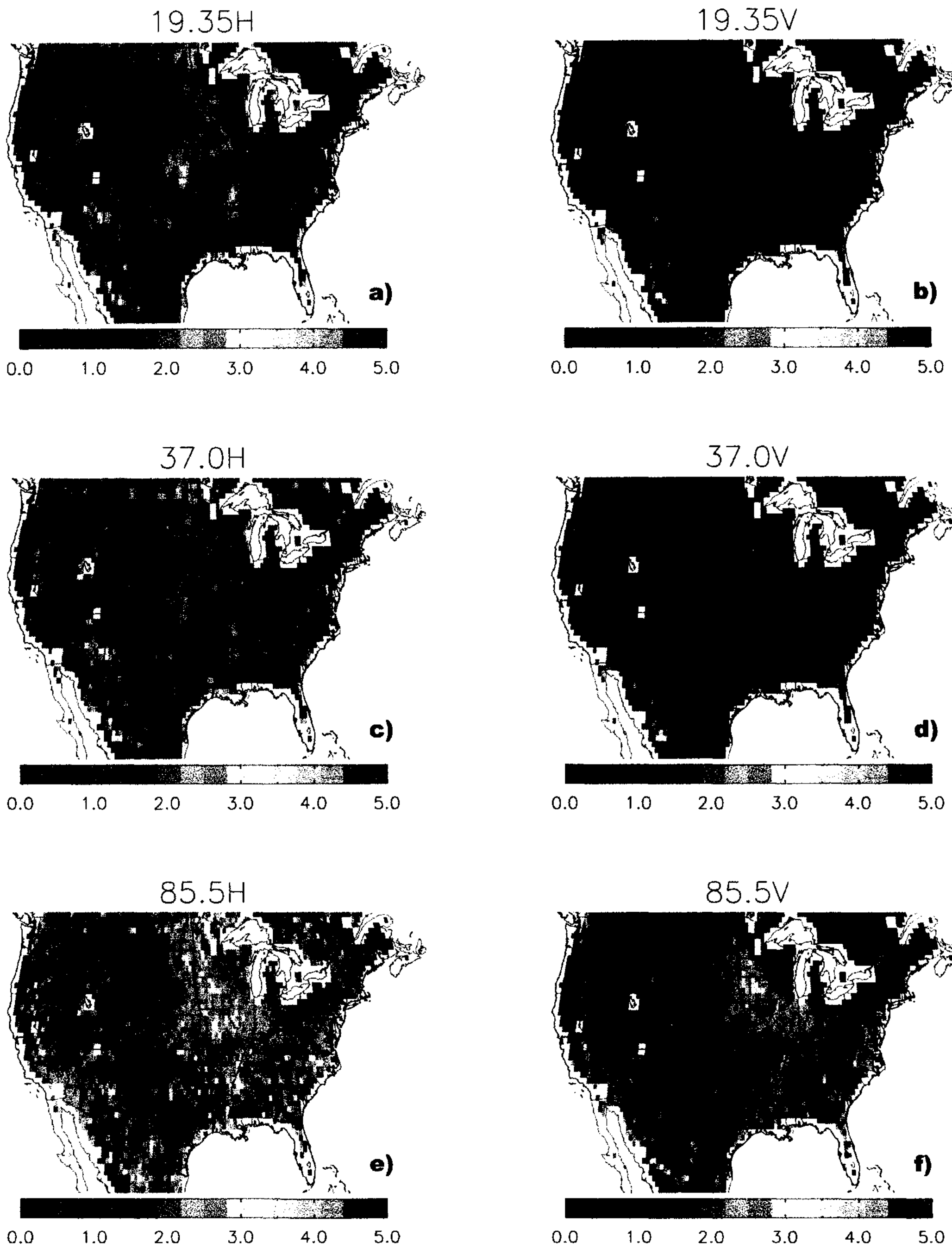

Figure 5.3: SSM/I ascending microwave land emissivity standard deviations normalized by the mean, and multiplied by 100, from June – August of 2000 – 2002 at six SSM/I channels: a) 19.35H, b) 19.35V, c) 37.0H, d) 37.0V, e) 85.5H, and f) 85.5V.

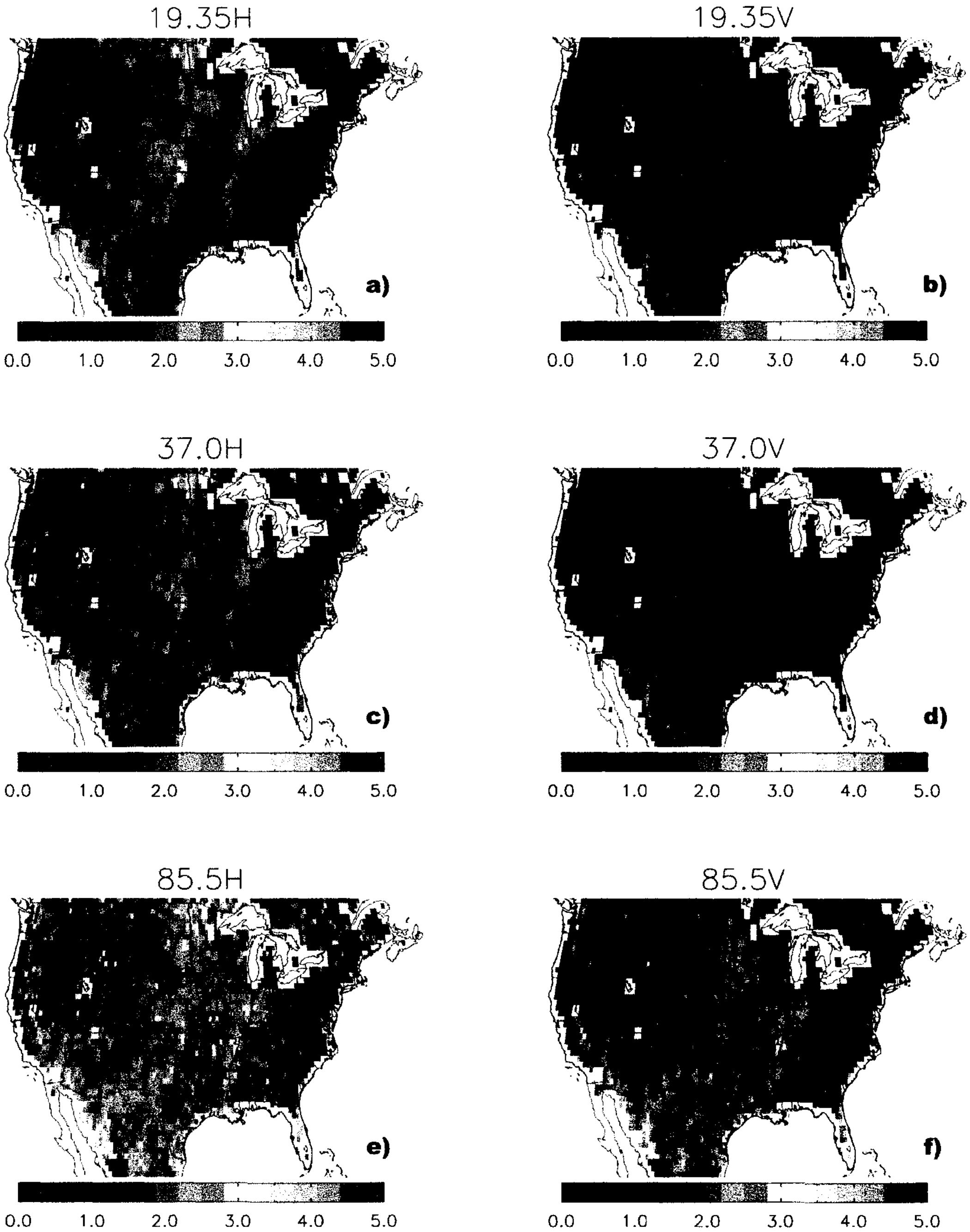

Figure 5.4: SSM/I descending microwave land emissivity standard deviation normalized by the mean values, multiplied by 100, from June – August of 2000 – 2002 at six SSM/I channels: a) 19.35H, b) 19.35V, c) 37.0H, d) 37.0V, e) 85.5H, and f) 85.5V.

soil and vegetation at higher terrain typically exhibiting lower soil moisture and plant water content. This rise can be seen from the Mississippi towards the Rocky Mountains, and from the California coast inland to the Sierra Nevadas; however, exceptions to this rise with elevation include deserts (highly scattering) and water bodies. In fact, the emissivities begin to recede due to the scattering by bare ground at some of the most complex high terrain, (e.g., central Colorado, the Absaroka Range in northwestern Wyoming, and the Salmon River Range north-east of Boise, ID). A decrease in the land emissivity is observed along the Mississippi and Missouri rivers, due to water effects, and higher soil and vegetation water content. Possible cloud contamination is seen north of the Gulf of California and Mexico, and to the west of Lakes Michigan and Superior. The 85 GHz channel is sensitive to ice scattering by thin cirrus clouds that may have been missed by the BST cloud mask. Also the distribution of inland water bodies is skewed to smaller fractional coverage in the half-degree grid. This makes the 85 GHz channels, with higher native resolution, more sensitive to these sub-pixel water bodies. Due to these effects, the 85 GHz emissivity means exhibit considerable spatial incoherence most predominantly in the states North of the Gulf of Mexico. Lastly, the emissivity means are often higher for the ascending (sunset) overpasses, most dramatically at vertical polarizations over elevated terrain.

The lower emissivity exhibited in the descending (sunrise) passes is attributed to the interpolation of the LST providing erroneously high LST values to the emissivity retrieval. The lower emissivity values could be viewed as possible response to surface dew; however, soundings obtained for Elko, Nevada and Albuquerque, New Mexico revealed few instances of nearly zero dew point depression. Overall, the emissivity was found to have no sensitivity to the dew point depression, and that dew is not an issue. Nocturnal inversions, common in the clear sky western US, were also examined for possible contamination of the emissivity results. For cases with nocturnal inversions, LST calculated from a sounding differed from those which used the RUC model by about 0.3 K, resulting in less then ~0.1% change in the microwave emissivity. The most extreme case occurred when the model had an inversion while the sounding did not. This produced a 1 K difference in the computed LST and a ~0.35 % change in microwave emissivity. Sunrise in the CONUS occurs most often between 12 and 15 UTC. After sunrise, especially in the western US, the LST can increase rapidly causing differences of greater than 10 K between 12 and 15 UTC. The linear interpolation of LST to the time of the satellite overpass raises the LST artificially before sunrise or too quickly after sunrise. A group of cases were evaluated over Albuquerque, NM where the mean ascending emissivity was 0.023 greater than the descending. Test cases were chosen where the satellite overpass was within an hour of sunrise. In these cases, when the surface temperature was adjusted to the pre-sunrise value, the descending emissivity was raised 0.021 on average. The retrieval when supplied with an overestimate of LST due to linear interpolation, produces a simulated microwave brightness temperature higher than observed by the satellite. To compensate the retrieval lowers the microwave surface emissivity. For the cases over Albuqueque, the interpolation errors in the LST are 6 K on average, and cause depressions in the microwave emissivity of ~2 %. The LST interpolation errors also give rise to differences in the individual satellite emissivity means. Each satellite produces a lower mean microwave emissivity in meridional regions where that satellite's ascending node is within an hour of sunrise. In summary, dew effects and nocturnal inversions where determined to have a low impact on the descending emissivity, while the interpolation of 3-hourly LST to the satellite time was determined to cause a decrease in microwave emissivity from ascending to descending overpasses.

The microwave land surface emissivity standard deviations in Figures 5.3 and 5.4 are predominantly less than 5% of the mean values, which are optimistically known to an accuracy of 2%, and conservatively to 5%. The emissivity standard deviations rise with frequency, and are typically higher at the horizontal polarizations where the spatial variability of land scattering is larger. Cloud contamination also contributes to greater standard deviations for the ascending overpasses. The highest values are seen for the ascending overpasses north of the Gulfs of California and Mexico, along the eastern US coast, and west of Lakes Michigan and Superior. The 85 GHz standard deviations for both ascending and descending passes exhibit considerable spatial incoherence, due to the skewed distribution of sub-pixel water bodies and greater sensitivity to cloud scattering.

Figures 5.5 – 5.7 show histograms of emissivities from 19, 37, and 85 GHz respectively. These histograms of the microwave land emissivities have several common features. The microwave emissivity is greater at the vertical polarization because the surface is a less efficient reflector of radiation in this polarized state. The increase in vegetative cover and its lushness increases scattering and minimizes the polarization difference between the channels. In heavily forested areas, the microwave emissivity polarization difference at 19 GHz is similar to that at 85 GHz. Bare ground areas show the vertically polarized emissivity value is about 0.04 greater than the horizontal at 19 GHz while this difference converges towards zero by 85 GHz. In bare ground areas the 19 GHz channels have a greater contribution from the ground, while as frequency increases very little ground cover is needed to effectively obscure the polarized signal from the ground. Lastly, the width of the histogram of emissivities is greater for the horizontal polarizations, because of the greater variability in the scattering efficiency of horizontal waves.

These histograms compare favorably with histograms published by Prigent et al. (1997) that are separated by vegetation classifications. Prigent et al. (1997) separated

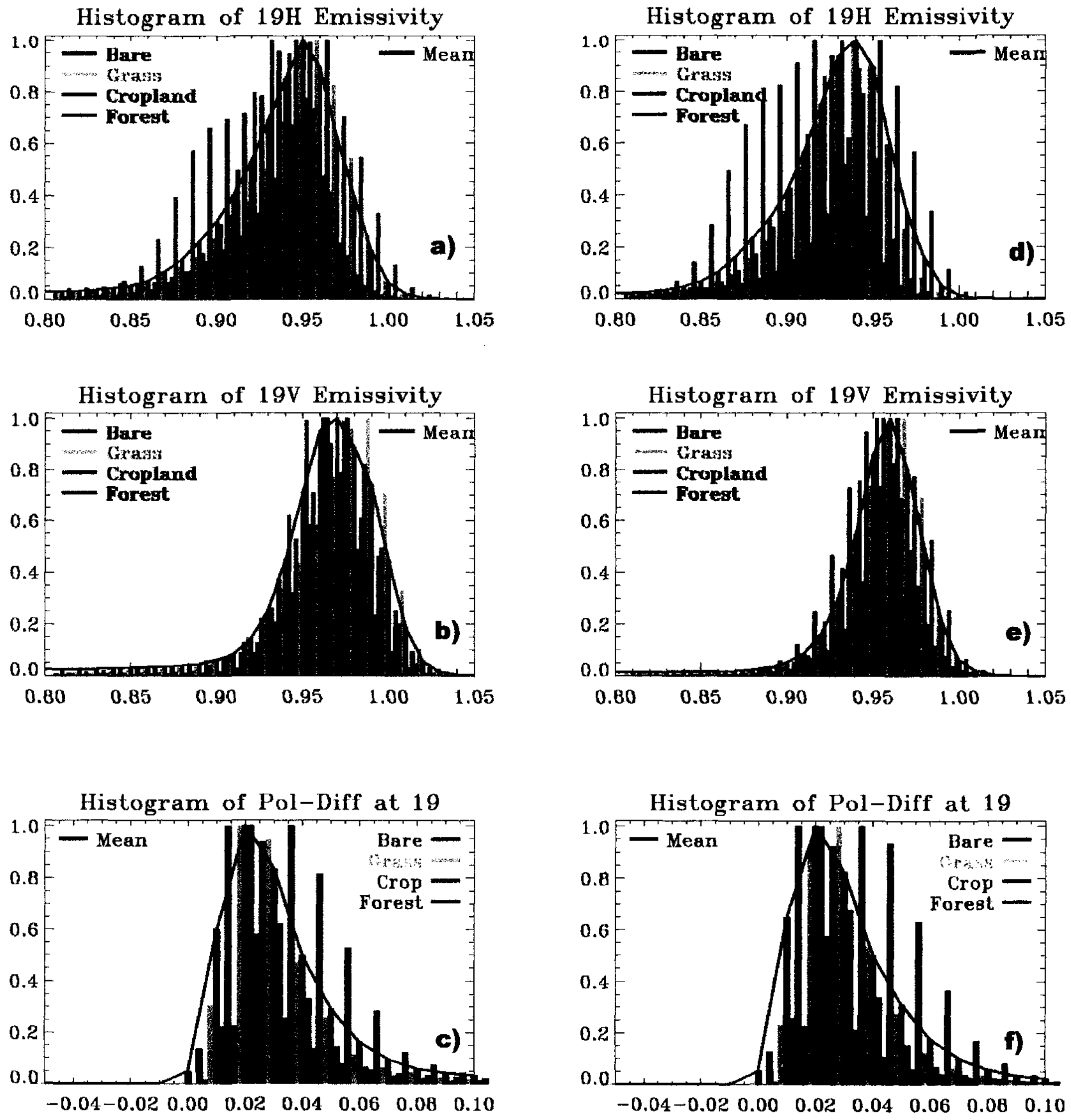

Figure 5.5: SSM/I 19 GHz microwave land emissivity histograms from the CONUS domain for 9 months: June – August, 2000 – 2002. Shown on the left are the ascending emissivity at: a) Horizontal, b) Vertical, and c) [Vertical – Horizontal]. Shown on the right are the descending emissivity at: d) Horizontal, e) Vertical, and f) [Vertical – Horizontal].

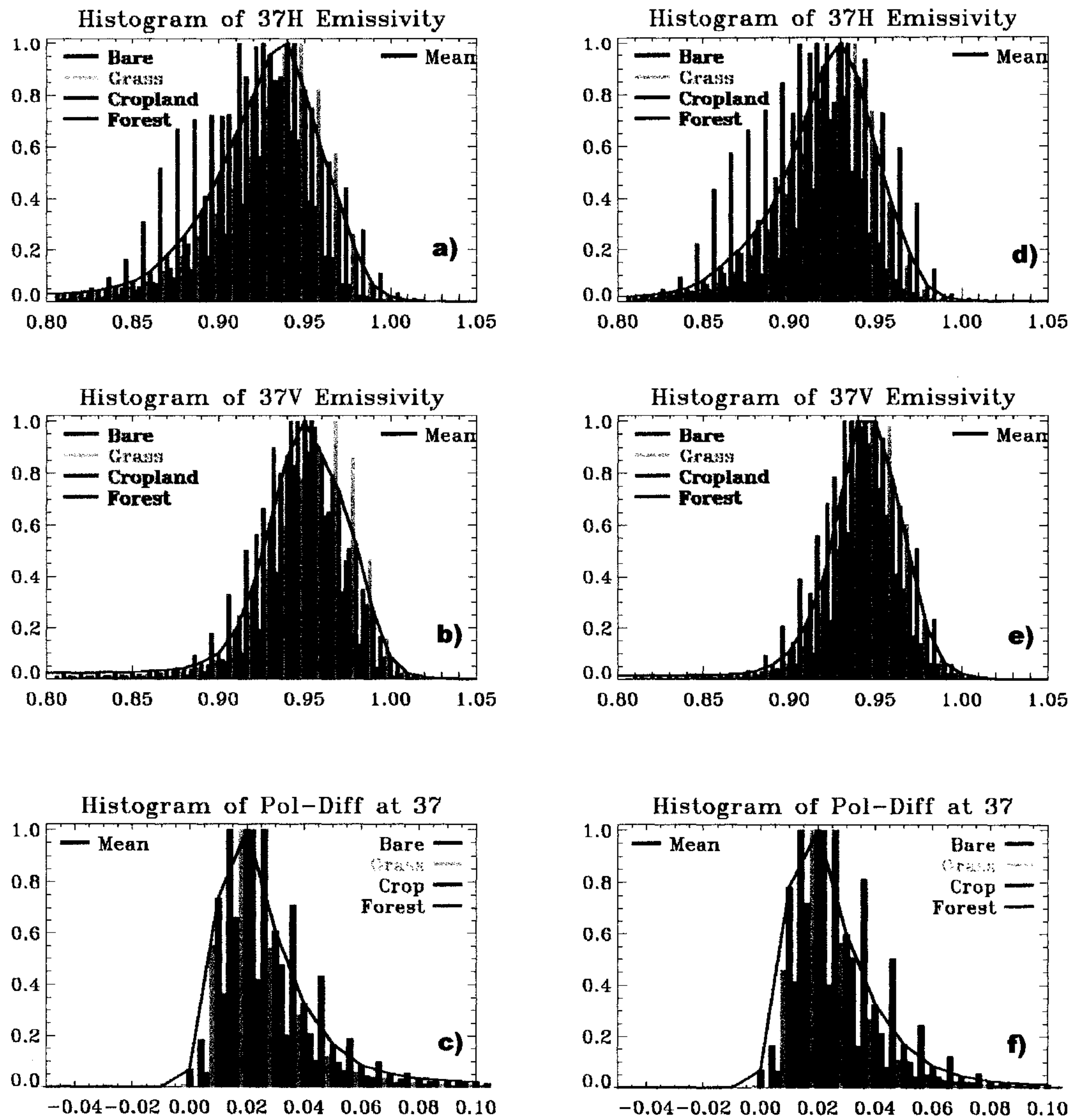

Figure 5.6: SSM/I 37 GHz microwave land emissivity histograms from the CONUS domain for 9 months: June – August, 2000 – 2002. Shown on the left are the ascending emissivity at: a) Horizontal, b) Vertical, and c) [Vertical – Horizontal]. Shown on the right are the descending emissivity at: d) Horizontal, e) Vertical, and f) [Vertical – Horizontal].

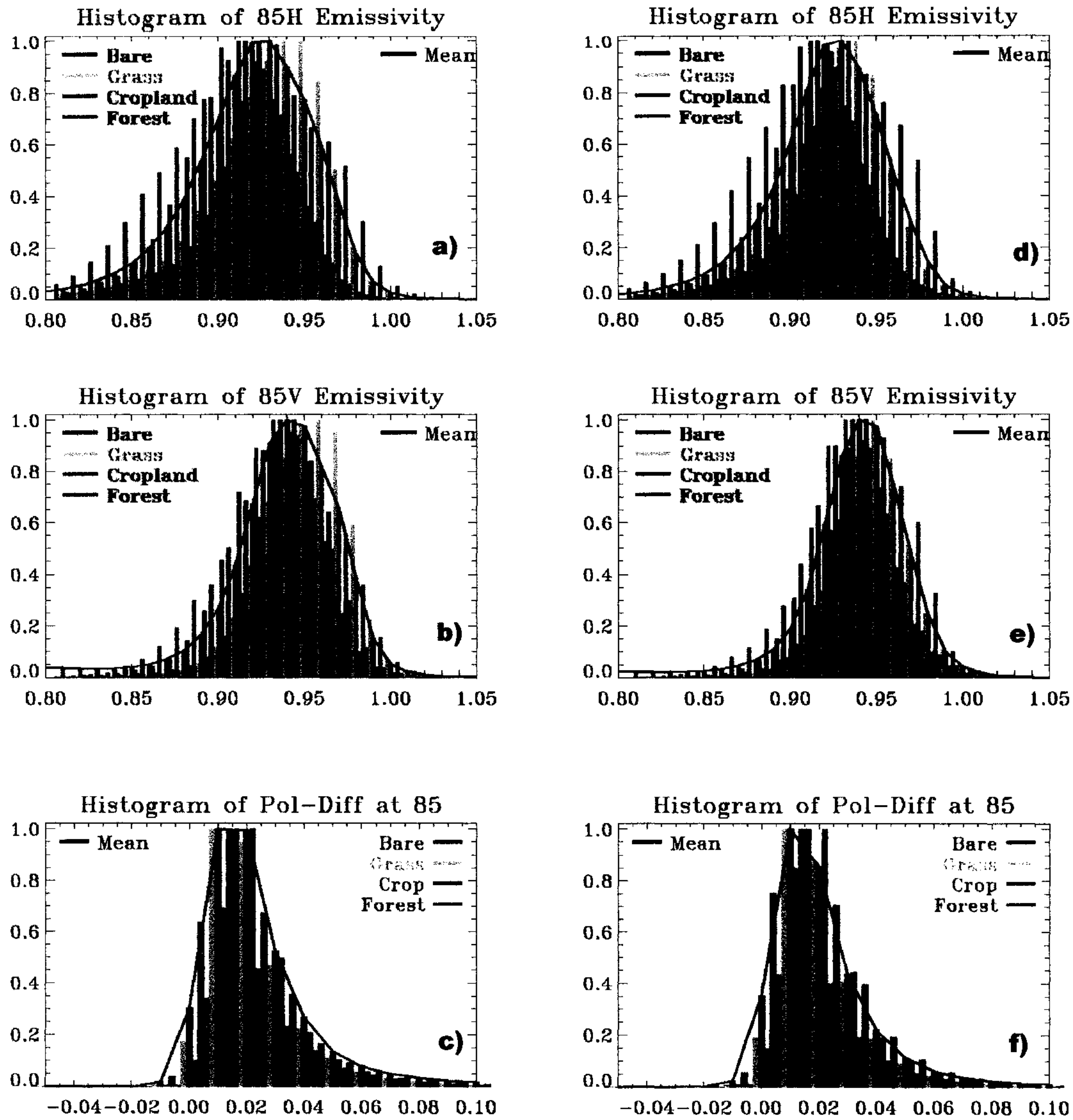

Figure 5.7: SSM/I 85 GHz microwave land emissivity histograms from the CONUS domain for 9 months: June – August, 2000 – 2002. Shown on the left are the ascending emissivity at: a) Horizontal, b) Vertical, and c) [Vertical – Horizontal]. Shown on the right are the descending emissivity at: d) Horizontal, e) Vertical, and f) [Vertical – Horizontal].

the emissivities into nine vegetation classifications, and the western US was dominated by the grassland, and shrubland classifications. Prigent et al. (1997) found that the horizontally polarized emissivities in these sparse vegetation types did not exhibit narrow distributions, and had rather long tails corresponding to relatively lower emissivities (<0.90). Shown in figure 5.5, are the histograms of directly retrieved 19 GHz emissivity for the bare ground classification. The structure described by Prigent et al. (1997) is seen in the horizontal polarizations for both ascending Figure 5.5a, and descending 5.5d emissivities. Further, the 19 GHz vertically polarized emissivities have a maximum value at 0.96 which also matches the maximum value retrieved by Prigent et al. (1997).

The polarization difference has a spectral trend related to both the vegetation and water fraction in a half-degree box. Figure 5.8 shows the polarization difference from the 9-month emissivity means, as a function of vegetation fraction for 19 and 85 GHz. The polarization difference decreases with increasing vegetation fraction resulting in a negative slope. The coefficient of determination (R^2) shows the percent of variance in the response variable described by the predictor variable. Table 5.1 shows the slope and R^2 for all three frequencies. Notice the correlation weakens, lower R^2, with increasing frequency. The increase in slope and decrease in R^2 with frequency is due to an increase in sensitivity to ground cover with frequency, which reduces the polarization difference. An opposite effect to the polarization difference is found with respect to water fraction. Water typically has lower emissivity and greater polarization difference than a land surface. The polarization difference of water is nearly constant with frequency; however, the smaller footprint at 85 GHz results in greater sensitivity to sub-pixel water bodies because of their distribution. In Figure 5.9, the distribution of water fraction is skewed to lower fractional coverage. This result of the skewed distribution is that the water bodies affect the higher resolution 85 GHz channels more strongly than

Table 5.1: Least square regression of predictor variable, vegetation fraction, to response variable, emissivity polarization difference. The slope and coefficient of determination (R^2) are shown for each frequency.

	Slope	R^2
19 GHz	-0.0438	0.281
37 GHz	-0.0336	0.225
85 GHz	-0.0280	0.160

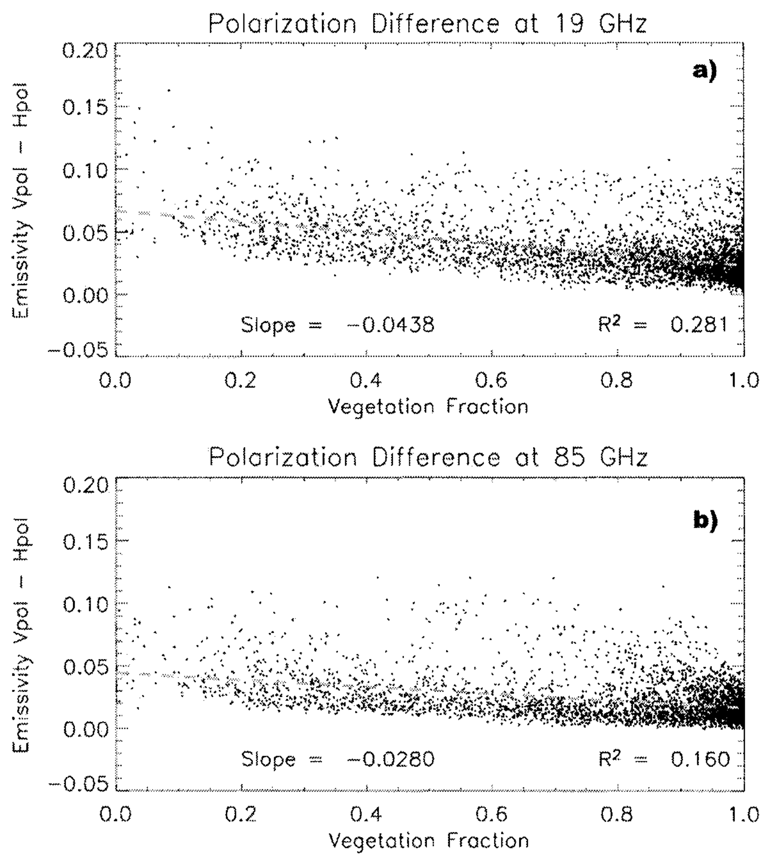

Figure 5.8: Scatter plot of polarization difference (from the 9-month emissivity means) as a function of vegetation fraction for a) 19 GHz and b) 85 GHz. The slope and coefficient of determination (R^2) from a linear least-squares regression are shown.

Table 5.2: Least square regression of predictor variable, water fraction, to response variable, emissivity polarization difference. The slope and coefficient of determination (R^2) are shown for each frequency.

	Slope	R^2
19 GHz	0.0848	0.025
37 GHz	0.1335	0.082
85 GHz	0.2878	0.326

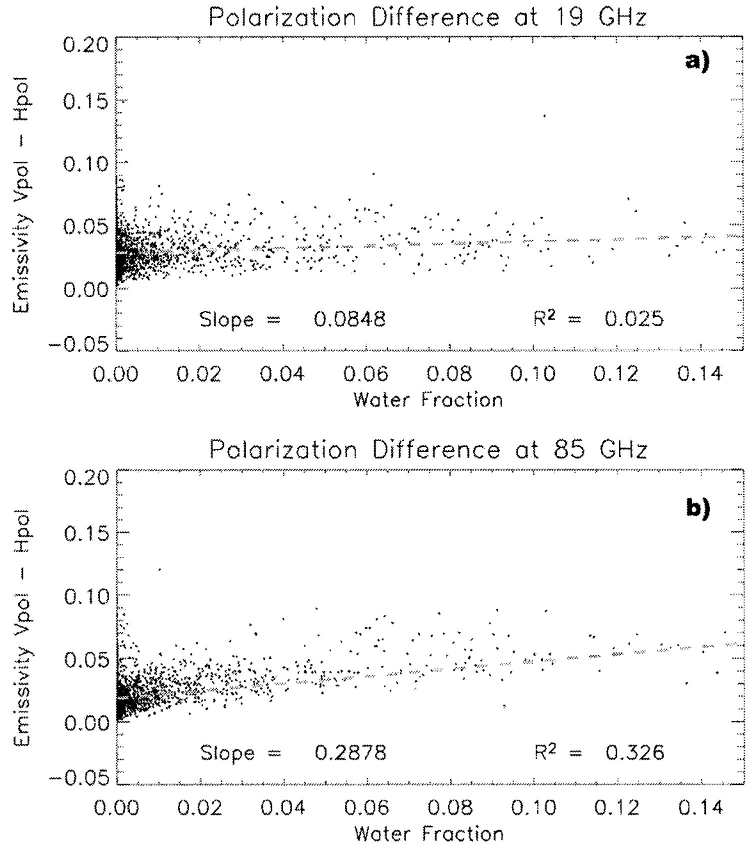

Figure 5.9: Scatter plot of polarization difference (from the 9-month emissivity means) as a function of water fraction for a) 19 GHz and b) 85 GHz. The slope and coefficient of determination (R^2) from a linear least-squares regression are shown.

the lower frequency channels. The slope and R^2 from a least square linear regression of emissivity polarization difference to water fraction is given in Table 5.2, while Figure 5.9 shows scatter plots of mean microwave emissivity polarization difference versus water fraction. Table 5.2 and Figure 5.9 show that the slope and R^2 both increase with increasing frequency, and that the water fraction has a varying effect on the emissivity polarization difference.

5.2 Optimal Estimation

The optimal estimation approach is performed over five case study regions using the SSM/I sensor data. The optimal estimation approach is used to test the robustness of the directly retrieved emissivity, by allowing the microwave emissivity answer to vary due to errors in the land surface temperatures (LST), model profiles of temperature and moisture, and the forward radiative transfer model. The optimal estimation of microwave emissivity is also used to retrieve the 85 GHz emissivities using only observations from the lower frequencies. This is to simulate situations where scattering by the atmosphere obscures the surface relative to the 85 GHz, while lower frequency surface radiation still strong transmits through the atmosphere. If the 85 GHz emissivity can be estimated using lower frequencies, the atmospheric scattering can be more effectively related to atmospheric quantities.

Five areas were chosen for study of their unique features. A region in the southeastern US, by Tuscaloosa, AL, is selected because of potential cloud effects in the direct retrieval. A case in southern Minnesota by Fairmont is chosen for the high variability in the 85 GHz emissivity. The ARM-SGP site was chosen because of the ancillary data, and general researcher interest in this test-bed site. Two sites were chosen to investigate the large day/night changes in emissivity: Elko, Nevada and Albuquerque, New Mexico.

The "observations" in the optimal estimation include the satellite brightness temperatures, the profiles of temperature and moisture, and the infrared retrieved land surface temperature. The observation error covariance is derived with perturbations of the atmospheric profiles and land surface temperatures, described in section 3.4.2. Uncorrelated and correlated perturbations are examined with all seven SSM/I channels included in the retrieval. Only correlated perturbations are examined when five SSM/I channels are included in the retrieval. The Degrees of Freedom (DF) are expected to drop when only five channels are used rather than seven. But there is also a dramatic decrease in the number of independent measurements determined by $\widetilde{K}$ (detailed in section 3.4.2.2) when the perturbations of the atmospheric profiles are vertically correlated. A test using 143 cases from the ARM-SGP site for 2001, found that when the perturbations of the atmosphere are vertically uncorrelated the average degrees of freedom (DF) is ~5, while the average DF drop to ~3 for vertically correlated perturbations, and to ~2.2 for vertically correlated perturbations using only five frequencies SSMI frequencies (85 GHz observations excluded). In a cloud free scene, all the frequencies get considerable contribution from the surface, and have the strongest atmospheric contribution from the distribution of water vapor (greatest at 22 and 85 GHz). The degrees of freedom is raised by uncorrelated perturbations since the random changes of the water vapor profile make each channel look more unique in radiance space. The more realistic vertically correlated perturbations cause more subtle radiative differences, and a subsequent loss of independent signal. The lower degrees of freedom makes the chi-squared (χ^2) test much more sensitive. Rarely do the optimally estimated emissivities pass a 90% confidence level when the degrees of freedom is 3, and even more infrequently when it is less than this. The vertically correlated perturbations made to the atmospheric profiles are considered more representative of actual profile errors, and observation covariances are generated with vertically correlated perturbations for the remaining analysis in this section.

Table 5.3: Percent emissivity difference between directly retrieved (first guess) emissivity and Optimally Estimated (OE) emissivities for six case studies. All 7 SSMI channels are used in the OE procedure. The absolute values of the difference are converted to percentages by normalizing with an average emissivity value (0.95), and multiplying by 100.

7 CH	19V	19H	22V	37V	37H	85V	85H	Samples
ARM-SGP	0.165	0.136	0.223	0.167	0.166	0.397	0.435	277
Albuquerque	0.152	0.288	0.201	0.230	0.396	0.607	1.005	142
Elko	0.139	0.154	0.184	0.183	0.207	0.390	0.508	315
Fairmont	0.169	0.138	0.229	0.185	0.207	0.503	0.559	290
Tuscaloosa	0.194	0.149	0.344	0.230	0.220	0.880	1.017	158

Table 5.4: Percent emissivity difference between directly retrieved (first guess) emissivity and Optimally Estimated (OE) emissivities for six case studies. Only the first 5 SSMI channels are used in the OE procedure, excluding the 85 GHz channels. The absolute values of the difference are converted to percentages by normalizing with an average emissivity value (0.95), and multiplying by 100.

5 CH	19V	19H	22V	37V	37H	85V	85H	Samples
ARM-SGP	0.165	0.123	0.209	0.163	0.158	0.942	1.218	277
Albuquerque	0.183	0.309	0.228	0.226	0.288	0.604	0.789	142
Elko	0.143	0.168	0.182	0.169	0.185	0.536	0.633	315
Fairmont	0.168	0.128	0.220	0.184	0.195	1.162	1.186	290
Tuscaloosa	0.190	0.163	0.343	0.205	0.212	0.911	1.063	158

The optimal estimation emissivity retrieval closely reproduces the directly retrieved emissivities from which it was trained. Tables 5.3 and 5.4 show percent emissivity differences between the directly retrieved first guess emissivities and optimally estimated emissivities for optimal estimation using all seven (Table 5.3) and the first five

SSM/I channels (Table 5.4) which excludes the 85 GHz brightness temperature observations. The average percent difference for the 19 – 37 GHz channels is very similar, while the 85 GHz differences do not necessarily become smaller when all seven channels are included. In the seven-channel retrieval, the 85 GHz brightness temperatures are calculated and constrained to the observations by the observational error covariance. The observational error covariance allows extra variability of the final emissivity answer over the five-channel method, which relies solely on the frequency cross correlations. The extra variability allowed by the observational error covariance results in the seven-channel method having potentially larger differences from the first guess than the five-channel method. Figure 5.10 displays contribution functions from the optimal estimation procedure with and without the 85 GHz channels. When all seven channels are included, each channel has the greatest contribution to its own emissivity retrieval. In the absence of 85 GHz data, the sensitivity to emissivity at 85 GHz is spread relatively evenly throughout the remaining five channels. Table 5.5 shows the *a priori* emissivity correlations for the ARM-SGP site. The correlations between all channels are high; and fall off with spectral separation. In general, the horizontal polarizations are more strongly correlated with the horizontal polarization at another frequency. These inter channel correlations are extremely important to the five-channel retrieval, as they alone determine the ability to which the 85 GHz emissivity is retrieved.

Table 5.5: Correlations of the *a piori* emissivities from the ARM-SGP site.

	19V	19H	22V	37V	37H	85V	85H
19V	1.000	0.930	0.964	0.974	0.928	0.697	0.769
19H	0.930	1.000	0.879	0.893	0.981	0.602	0.779
22V	0.964	0.879	1.000	0.958	0.888	0.755	0.792
37V	0.974	0.893	0.958	1.000	0.924	0.768	0.813
37H	0.928	0.981	0.888	0.924	1.000	0.662	0.831
85V	0.697	0.602	0.755	0.768	0.662	1.000	0.893
85H	0.769	0.779	0.792	0.813	0.831	0.893	1.000

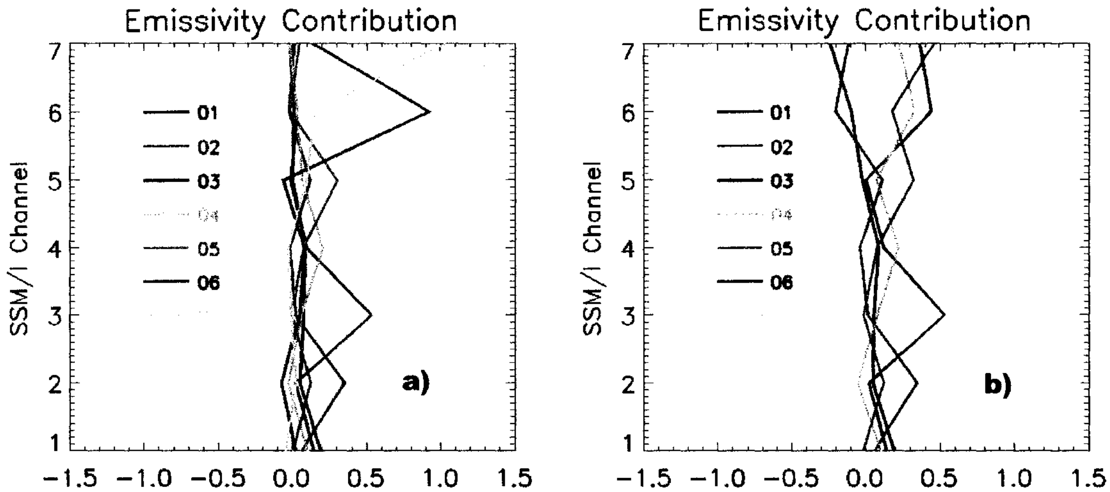

Figure 5.10: Contribution functions of each of the SSM/I brightness temperature observations to the retrieval of emissivity at each channel. The contribution functions are normalized by the mean emissivity from 143 cases, and multiplied by 100. The x-axis may be considered a percentage of emissivity. To the left: a) contribution of each of the seven SSM/I observations to emissivity at the seven SSM/I channels. To the right: b) contribution of each of the five SSM/I observations to emissivity at the seven SSM/I channels.

5.3 Atmospheric Profiling

In August of 2003, I had a unique opportunity to implement results of my research into an operational environment. Baker et al. (2001) developed an AMSU based one-dimensional variational (1DVAR) profiling algorithm, which has been used with success over ocean areas. This section presents results from a case study over the ARM-SGP site. GOES Land Surface Temperatures (LST) are used in the direct inversion approach to retrieve AMSU emissivities over the ARM-SGP site for July and August of 2000 – 2002. The directly retrieved emissivities are used as a first guess in the 1DVAR algorithm, while the six-month climatology provided *a priori* statistics.

NOAA-15 (launched in Oct. 1998) and NOAA-16 (launched in Feb. 2001) are used to retrieve emissivity estimates over the ARM-SGP site. The nearest neighboring half-degree LST values, retrieved from GOES, are interpolated spatially and temporally to the AMSU scan location. The nearest neighboring RUC model profiles of temperature and moisture are used to calculate the microwave extinction coefficients. No spatial interpolation was performed on the AMSU data. Shown in Figure 5.9 are histograms of the emissivities retrieved for channels 1, 2, 3, and 15 (23.8, 31.4, 50.3, and 89.0 GHz). These channels typically have transmissions of 0.5 or greater. At transmissions below 0.5 the signal-to-noise ratio becomes too low to practically use the direct retrieval to calculate emissivity. All four frequencies shown in Figure 5.11 show considerable stability over the region. A mean value of 0.96 could be used to make a spectrally invariant estimate of the emissivity for this location. A 3% emissivity standard deviation is used to describe the emissivity characteristics at the ARM-SGP site for all frequencies.

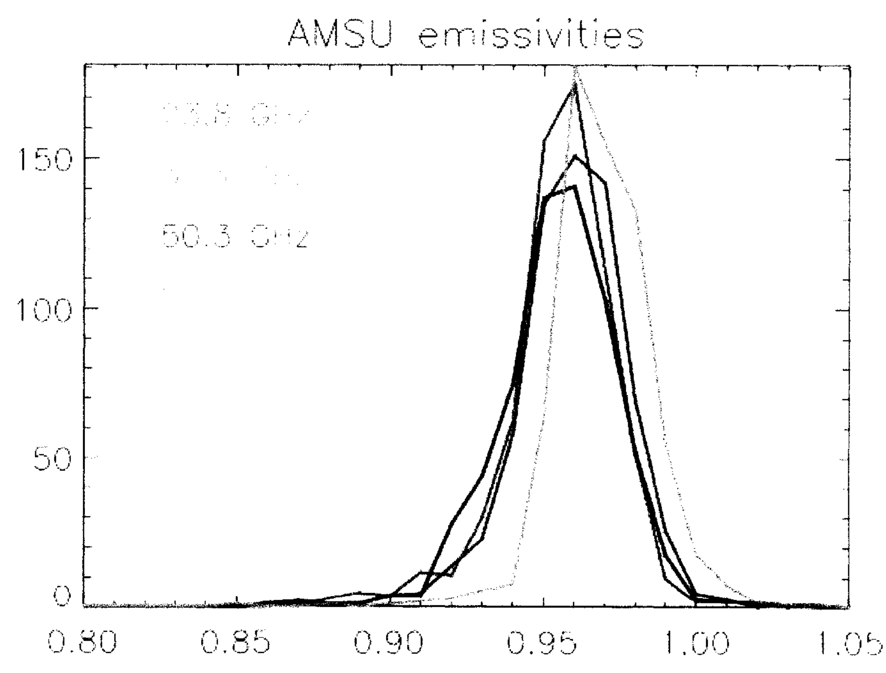

Figure 5.11: Histograms of retrieved AMSU emissivities over the ARM-SGP site from July and August, 2000 – 2002. Channels 1, 2, 3, and 15 (23.8, 31.4, 50.3, and 89.0 GHz) are shown respectively.

At 50.3 GHz, AMSU's channel 3 is on the wing of a strong complex of oxygen absorption, centered at approximately 60 GHz. Channels 4 – 14 (spanning the 52.8 – 57.29 GHz spectral range) proceed spectrally into the oxygen absorption feature, with subsequent sensitivity to shallower atmospheric columns. A typical atmospheric transmission for channel 4, at 52.8 GHz, is around 20%. As stated earlier this is too insensitive to the surface to accurately retrieve its emissivity. The surface emissivity retrieved for channel 3 (50.3 GHz) will be used as the first guess for channels 4 – 14.

Figure 5.12 displays the temperature and moisture contribution functions for each of the 15 AMSU channels as a function of height. This plot is created from the AMSU-A aboard NOAA-16 for July 13, 01:50 UTC; channels 11 and 14 were not functional at this time. The window channels, channels 1 – 3 and 15, show no perceptible temperature sensitivity to the atmospheric profile. The remaining channels are found sensitive to temperature at sequentially higher levels in the atmosphere. The window channels show moisture sensitivity at the lowest levels, though opposite in sign, and less dramatic than channels 4 – 6. This change highlights the difference the addition of low-level water vapor will have on the window channels versus the oxygen band channels. The increase in low-level water vapor will present a source of radiation above the window channel main source, the surface. While for the oxygen band channels, the increase in low-level water vapor will introduce a source of radiation below the height at which their oxygen sensitivity is a maximum.

A useful analysis tool to view the correlations of the parameters and the observational contribution is the averaging kernel or **A** matrix (Equation 3.24). This weights the contribution functions by the forward model sensitivity matrix, **K**. Values of -1 or 1 signify 100% contribution by the observations to the parameter retrieval; while values of 0 signify 100% contribution by the *a priori*. Figure 5.13 shows the mean

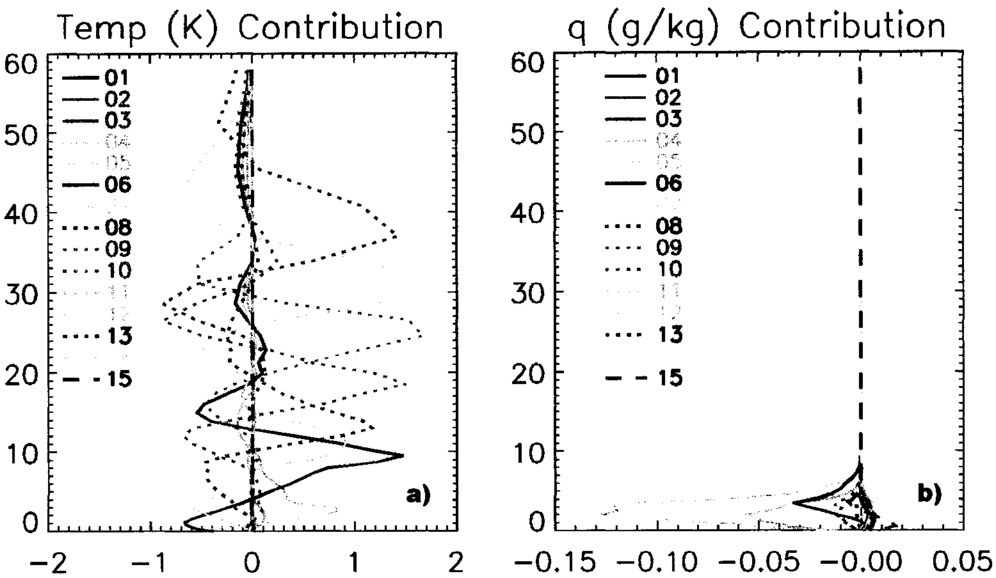

Figure 5.12: The a) temperature and b) moisture contribution functions for the 15 AMSU-A channels as a function of height. This plot is from AMSU-A aboard NOAA-16 on July 13, 01:50 UTC. Channels 11 and 14 were not operational on the NOAA-16 AMSU-A instrument for this time.

averaging kernel for 67 retrieval cases over the ARM-SGP site. If the measurements uniquely give information about each parameter a diagonal matrix with absolute value of unity would result. Off diagonal elements relate how the retrieval of one parameter impacts others. The matrix stacks the variables: temperature (43 levels), specific humidity (43 levels), and surface emissivity (15 channels) together. The profiles of temperature and moisture decrease in height with rising index. In regard to the atmospheric profiles, it can be noticed almost immediately that the AMSU-A observations give the most independent input to the retrieval of upper atmosphere temperatures. It has little effect to the moisture profile, with a slight maximum at the lower levels. In the upper right corner of Figure 5.13 are the observational contributions to the microwave emissivity. The **A** matrix is noted to be nearly diagonal for the window channels, with no information being added to the emissivity for channels 6 – 14. The non-symmetric appearance of the **A** matrix is expected, and tells a lot about the behavior of the data in the actual retrieval. The large values in the columns associated with the emissivity show that the emissivity has a significant impact on the retrieval of temperature and moisture, most considerably in the lowest levels. However, the inverse is not true in the row space. The averaging kernel matrix, in a not so subtle way, shows that an accurate estimate of emissivity with well defined characteristics will have a considerable impact on the temperature and moisture values retrieved. While the specific atmospheric temperature and moisture profiles do not have a large impact on the emissivity retrieval.

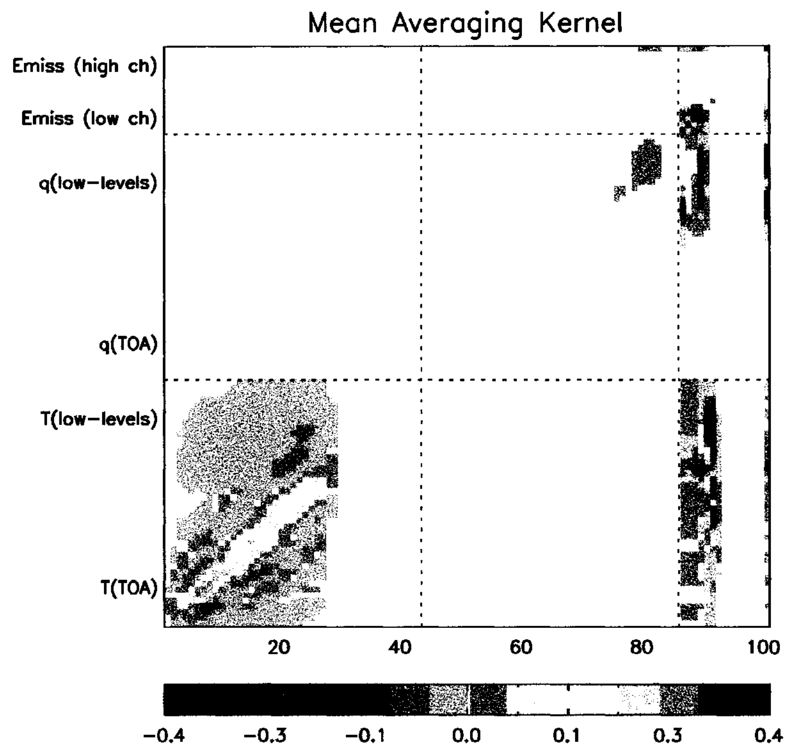

Figure 5.13: The mean averaging kernel for 67 temperature retrieval cases using AMSU-A and the NOGAPS model over the ARM-SGP site.

The information contained in the columns of the **A** matrix can be more closely examined by looking at a number of heights individually. Figure 5.14 shows 9 columns (of 43 total NOGAPS levels) that correspond to particular pressure levels in the model. The pressures are assigned heights using the US standard atmosphere. The information in the **A** matrix indicates the weighting of observational data. Full weighting of *a priori* data is represented by a zero value while values of ±1 indicate full weighting of observational data in the retrieval. In Figure 5.14a the temperature sensitivity of a particular height level is seen to peak near its actual level, with cross-correlations indicated by the vertical width of the peaks. In the lowest few kilometers of the atmosphere the temperature information is highly correlated to the information from upper levels. This indicates a difficulty in representing sharp inversions in this system. The specific humidity sensitivity shown in Figure 5.14b is dominated by the lowest few levels, which is not surprising since the majority of water vapor is in these levels, and the AMSU-A instruments is not designed as a moisture sounding instrument.

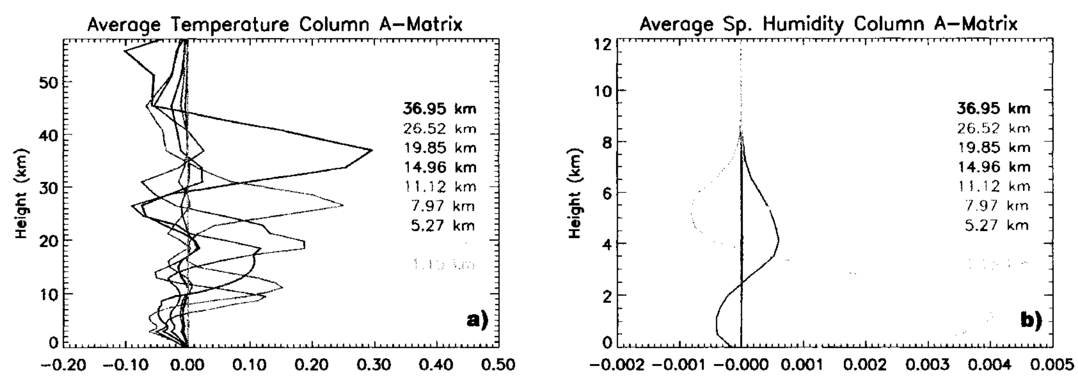

Figure 5.14: Individual columns of the mean averaging kernel for 67 temperature retrieval cases using AMSU-A and the NOGAPS model over the ARM-SGP site. Shown are a) temperature to temperature level correlations; and b) specific humidity to specific humidity correlations.

The correlation of the emissivity to the boundary layer temperature and specific humidity is shown in Figure 5.15. In this figure we present the first five AMSU-A channels and channel 15. The remaining AMSU channels (6 through 14) have virtually no direct sensitivity to the surface and their contribution to the temperature and moisture in the lower atmosphere is zero for all practical purposes. Figure 5.15a shows the correlation of the low-level temperature profile to the emissivity of channels 1 – 3 and 15 is similar in structure, with channel 15 having the strongest correlation due to its heightened sensitivity to moisture. Channels 4 and 5 show their strongest impacts on temperature above the surface at about 4 and 6.5 km respectively, and also have vertical correlation to temperature nearing the surface. In the specific humidity response to microwave emissivity shown in Figure 5.15b we again see channels 1 – 3 and 15 having similar structures, with channel 15 exhibiting the strongest signal. Channel 15 at 85.5 GHz has a much greater atmospheric attenuation than the other channels, and it is expected that the strongest moisture signal in this channel. Channels 4 and 5 display negative sensitivity, where to maintain a nearly constant outgoing radiance a raise in emissivity is compensated by drying of the atmosphere in the lowest few kilometers.

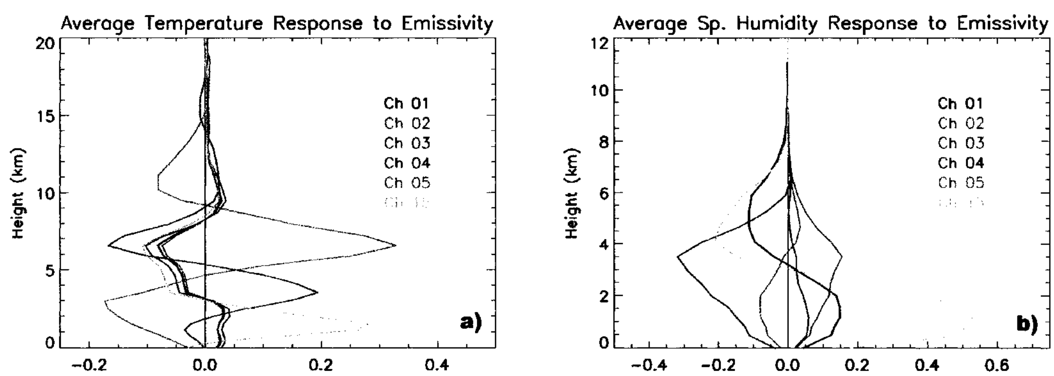

Figure 5.15: Individual columns of the mean averaging kernel for 67 temperature retrieval cases using AMSU-A and the NOGAPS model over the ARM-SGP site. Shown are a) emissivity to temperature level correlations; and b) emissivity to specific humidity correlations.

A metric used to test the Gaussian distribution of errors is the χ^2 test. To perform this test the degrees of freedom in the system must first be found. In the 81 cases studied, there were on average six singular values of $\tilde{K}$ (defined in Equation 3.27) greater than unity. The χ^2 statistic was calculated using Equation 3.25, and is a sum of the final estimate of forward model error weighted by the observation error covariance, and the difference between the retrieved parameter and the *a priori*, weighted the *a piori* error covariance. This test can indicate when the system is producing suspect results. To illustrate, two cases are chosen for comparison. The first is a control case using the NOGAPS default land surface temperature and a fixed emissivity of 0.90. The second uses the GOES retrieved LST and the directly retrieved AMSU emissivities. Figure 5.16 shows the initial simulated brightness temperature difference from observation. The control case produces differences that are an order of magnitude greater in the window channels. The contribution functions for these cases are very similar (not shown), analysis of the averaging kernel showed the control case was receiving greater impacts from the observations in both the temperature and moisture profiles. However, since the initial brightness temperature estimate was so far off, the 1DVAR procedure made adjustments wherever possible to match the AMSU observation. This may make some correct adjustments, but is relying on blind luck. The χ^2 statistics for the two cases show something is awry with the control case producing a value of 390.28; while the case using the retrieved LST and emissivities produced a value of 1.36. The large χ^2 value for the control case raises a red flag, implying that our retrieval errors are not consistent with our *a priori* and observation error assumptions. This result emphasizes the importance of accurate microwave land emissivity estimates and its characteristics for successful retrieval of low-level temperature and moisture fields.

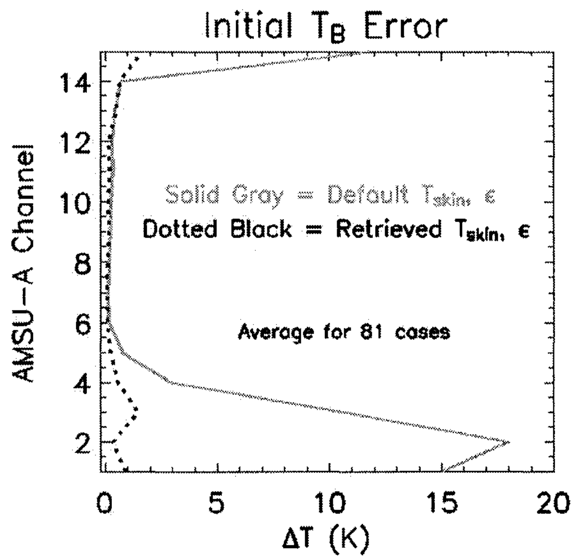

Figure 5.16: Initial brightness temperature error in two retrieval approaches implemented using the NRL 1DVAR routine. The gray line corresponds to retrievals which used NOGAPS land surface temperature and a fixed emissivity of 0.9; while the dotted black line corresponds to retrievals which included the GOES retrieved LST, and directly retrieved AMSU emissivities.

Of 81 retrieval cases performed, 67 had co-located radiosonde data that could be used for comparison. The Root Mean Square (RMS) difference of the retrieval was found for these 67 cases and is presented in Figure 5.16. In this figure three RMS values are shown. The first is from the original profile or *a priori*. The second is from the profiling retrieval which begins iterations using directly retrieved AMSU emissivities and GOES LST. The third RMS values are from the retrieval which begin iterations using a fixed AMSU emissivity of 0.90, and LST estimated by the NOGAPS analysis. The temperature RMS shown in Figure 5.17a shows that the retrieved profiles using the explicitly calculated AMSU emissivities has improved performance, in the lower 2 km, over the *a priori* and fixed emissivity cases. The specific humidity RMS shown in Figure 5.17b shows that the retrieval using the explicitly calculated AMSU emissivities does not alter greatly from the original *a priori* profile, while the fixed emissivity case because the simulated brightness temperatures have such a large error tries to correct for this by modifying the lower atmosphere moisture, and subsequently increases the RMS difference of the moisture profile.

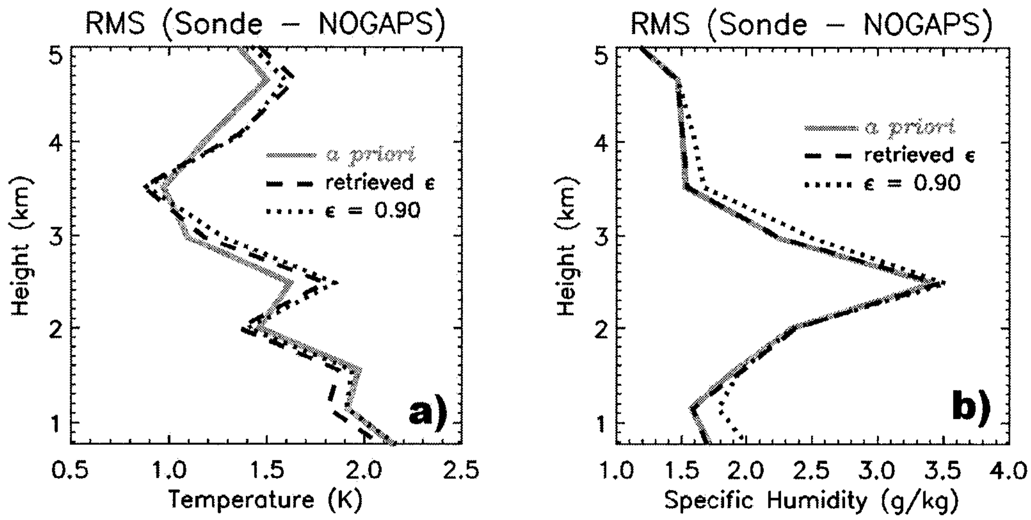

Figure 5.17: The Root Mean Square (RMS) difference between 67 NOGAPS profiles and profiles from co-located radiosondes. Three cases are shown: the original *a priori* data (gray); a case beginning with explicitly retrieved AMSU emissivity (black dashed), and a case beginning with fixed AMSU emissivity of 0.90 (black dotted). Shown are the RMS differences between radiosonde and NOGAPS profiles of a) temperature and b) specific humidity.

The adjustments made by the 1DVAR retrieval system to the original *a priori* profiles is shown in Figure 5.18. Here the retrieved profiles that began iterations with explicitly calculated AMSU emissivity, make smaller adjustments to both original temperature and moisture profiles. It is important to realize that larger adjustments to the *a priori* specific humidity are often not advantageous as shown by the fixed emissivity case, where the larger adjustment give a higher RMS value (as shown in Figure 3.17b). Specifically for these cases at the ARM-SGP site, the NOGAPS analysis is well conditioned and the initial errors are relatively low. Large adjustments made to the *a priori* may hurt the accuracy of the profile. Over areas where the initial conditions are not as well known, a well-defined emissivity is needed to improve the *a priori* profile as the lower level temperature and moisture have strong correlations to the emissivity of the surface as shown in Figure 5.15.

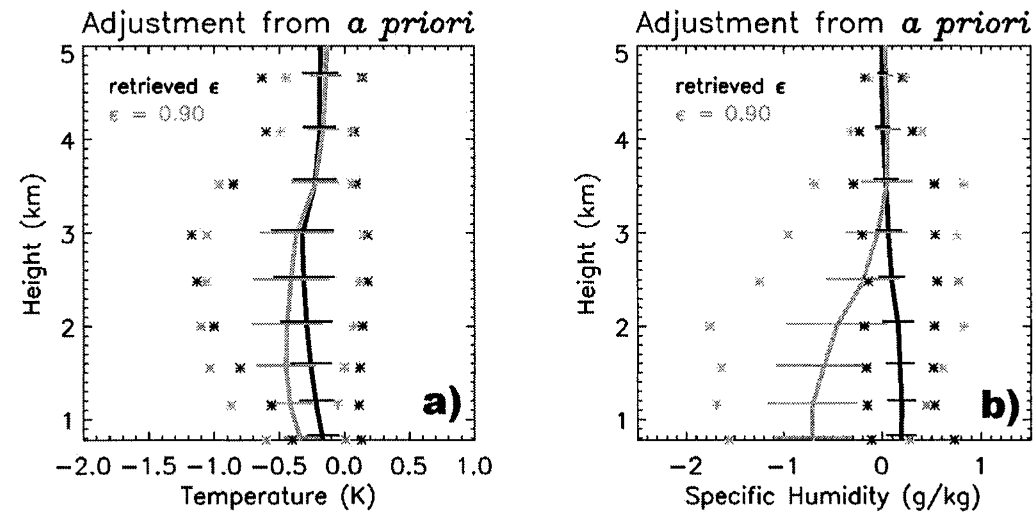

Figure 5.18: The average adjustment made to the *a priori* profile for 67 retrievals. Two cases are shown: a case beginning with explicitly retrieved AMSU emissivity (black), and a case beginning with fixed AMSU emissivity of 0.90 (gray). The average adjustments are indicated by a vertical line, ±1 standard deviation by horizontal lines, and min and max values by asterisks. Shown are the adjustments made to *a priori* a) temperature and b) specific humidity.

6. Conclusions

6.1 Summary of Results

The results from the direct retrieval of microwave land emissivity have shown an ability to retrieve a stable estimate of emissivity. Typical standard deviations are 5% of the mean value over the summertime months. Error budget analysis suggests errors of up to 5% in some cases, while it is reasonable to assume errors of less than 2% for frequencies less than 85 GHz.

In the retrieval of the microwave emissivity, a Bi-Spectral Threshold (BST) cloud-screening procedure is used based on methodology of Jedlovec and Laws (2003). The BST cloud screen compared favorably with the state of the art MODIS cloud mask. When the BST cloud screen declared a half-degree box cloud free, the average cloud fraction detected by MODIS was 4%. A spatial distribution of the MODIS cloud that wasn't detected by the BST cloud-screen highlighted problem areas north of the Gulfs of California and Mexico.

A Geostationary Operational Environmental Satellite (GOES) infrared based Land Surface Temperature (LST) retrieval was performed. The land surface was given a spatially variant infrared emissivity created with a spectral library and soil and vegetation database. The GOES LST was compared with the MODIS LST product. The GOES LST were found to be cooler on average than the MODIS LST predominantly at nighttime hours. The MODIS LST consistently produces higher LST in the Sierras and

Rockies both day and night. Besides the mountain bias, the nighttime cool bias in the GOES LST is small and evenly distributed. During the daytime the warm bias in the MODIS LST grows, covering much of the western high plains and mountains; however, the MODIS LST becomes cooler than the GOES LST in the states north of the Gulf of Mexico.

Results of the microwave land emissivity are consistent with values found Jones (1997) over the central US. Also the histograms of microwave emissivity grouped by vegetation classification are consistent with those found by Prigent and Rossow (1997). The 85 GHz frequency exhibits the most spatial inhomogeneity. This is attributed to undetected thin cirrus and sub-pixel water bodies with a spatial distribution skewed to smaller fractional area in the half-degree grid. Many of the lower 85 GHz mean emissivity pixels can be tied to small lakes in the region north of the Gulf of Mexico where cloud contamination is also suspected.

The optimal estimation procedure was successful in retrieving 85 GHz emissivity without the 85 GHz observational input. The values typically are within 0.5% of the directly retrieved values for frequencies less than 85 GHz. At 85 GHz, the optimally estimated emissivities are up to 1% different than those that are directly retrieved. The largest differences occurred in the cases where the directly retrieved emissivity was multiple standard deviations from the mean value. The optimal estimation routine didn't allow the retrieved emissivities to stray very far from the mean. The use of optimal estimation to retrieve the 85 GHz emissivity using only the lower frequencies is a method with very few degrees of freedom, and should be used with extreme caution. It can provide an estimate if necessary, but the user should be well aware of its deficiencies and be familiar with the land region of interest. An alternate way of calculating 85 GHz emissivity would be to use an accurate forward microwave emissivity model. This would be an ideal solution to getting an estimate of microwave land emissivity in situations where the atmospheric transmission drops (<0.5). However, the choice of surface parameters to use in a forward emissivity model, and their initialization is still an area of active and ongoing research.

The Naval Research Laboratory (NRL) One-Dimensional Variational (1DVAR) retrieval was used to examine the sensitivity of atmospheric profiles to the microwave land emissivity over the Atmospheric Radiation Measurement (ARM) program Southern Great Plains (SGP) site. The sensitivity of the atmospheric profiles to the microwave land emissivity was largely described in the asymmetric averaging kernel, or **A** matrix. The **A** matrix is the observation contribution function weighted by the forward model sensitivity function. When examining the **A** matrix the large off diagonal elements in the emissivity column space indicate the temperature and moisture profiles, predominantly at low levels, are greatly dependent on the emissivity value. An accurate LST and first guess microwave land emissivity with appropriate characteristics will be needed to properly retrieve low level temperature and moisture profiles with the AMSU-A instrument.

6.2 Conclusions

The microwave emissivity standard deviation over high terrain in the western US, is less than or comparable to those over the rest of the CONUS region. Because emissivity varies as a function of incidence angle, greater standard deviations over the high complex terrain in the west could be expected, however it was not found in the results. The most noticeable effect of high complex terrain is a depression in the emissivity at the 19 GHz channels seen over central Colorado and the Salmon River Range (north-east of Boise, ID) that could be attributed to scattering by the bare ground. The retrieved 85 GHz emissivities show little polarization difference over these high terrain areas, this implies that the ground cover is sufficient to scatter the ground signal. This reduces many dependencies the 85 GHz emissivity has on the orientation of the terrain, which would manifest as higher standard deviations.

The difference between the GOES LST and MODIS LST, averaged over the CONUS, is smaller during the daytime. This domain averaged bias approaches zero because regional biases have opposite signs. During the daytime the western US predominantly has MODIS LST > GOES LST, while the southeastern US predominantly has GOES LST > MODIS LST. These two biases of opposite sign cancel out for an overall bias close to zero. The pattern of the daytime bias resembles a pattern of water vapor which is low in the western US and increases in the states north of the Gulf of Mexico. This could be due to inaccuracies in the RUC profiles, in the MODIS retrieval of the water vapor column, or a combination of both. Wan (2002) suggests that the infrared emissivities of arid and semi-arid terrain are overestimated in the classification-based infrared emissivity map (Snyder et al. 1998). Wan estimated this caused a 2.3 K underestimation in LST at a validation site in Nevada. Infrared emissivities retrieved in the MODIS day/night LST algorithm (Wan, 1999) have a strong underestimation seen in the southeastern US that appears to be a water vapor contamination feature. Further validation information from field projects, and satellite interferometers should help to better estimate the infrared emissivity, and produce improved LST products. The overestimation of arid and semi-arid infrared emissivities does not seem unreasonable, but validation data is still lacking. A simultaneous infrared/microwave emissivity and land surface temperature retrieval would aid in reducing errors in the LST and infrared/microwave emissivity products.

In this study, the emissivities retrieved from descending SSM/I passes were found to have a lower mean value than their ascending counterpart. Dew effects and nocturnal inversions were not found to have a significant impact on the descending emissivities. The explanation for the lower values was the interpolation of pre and post sunrise LST for an overpasses occurring near sunrise. The elevated post sunrise LST prematurely raises the LST to a value that is too warm, and the retrieval depresses the emissivity to match the microwave observations. This problem can be remedied in a few ways. The first would be to use a different interpolation scheme that accounts for the rising of the sun. Another option would be to retrieve the LST more frequently, reducing the interpolation error. A final option is to retrieve the LST using an infrared instrument flying on the same satellite bus as the microwave instrument. NOAA-15, NOAA-16, and NOAA-17 carry the AMSU along with the Advanced Very High Resolution Radiometer (AVHRR) and High Resolution Infrared Radiation Sounder (HIRS) either of these instruments could be used to retrieve LST. The DMSP satellites carry the SSM/I instrument along with the Operational Linescan System (OLS) that has an infrared window channel suitable for LST retrieval. The Tropical Rainfall Measuring Mission (TRMM) sensor package includes the conically scanning TRMM Microwave Imager (TMI), and the Visible and Infrared Radiometer System (VIRS), which could be used together for LST and microwave emissivity retrievals.

A One-Dimensional Variational (1DVAR) Retrieval was performed over the ARM-SGP site for July and August of 2001. The retrieval used the 15-channel AMSU-A satellite temperature profiling instrument. The 1DVAR system retrieved emissivity for the AMSU-A channels, and profiles of temperature and moisture at 43 levels. The system had on average 5 degrees of freedom and produced an answer with Gaussian error behavior, only when the first guess emissivities allowed effective simulation of the AMSU-A radiances. With the large number of variables being retrieved in this system, accurate first guess emissivities, temperature profiles, and moisture profiles, are necessary for a robust retrieval. For the 1DVAR retrieval case performed the accuracy of the temperature and moisture profiles was assumed. The sensitivity of the lowest levels in the temperature and moisture fields to emissivity, imply that as the estimate of microwave emissivity improves, gross trends in the low-level moisture and temperature can be detected using this retrieval system.

6.3 Future Work

The infrared land emissivity atlas could be improved with a larger spectral library containing a wider variety of vegetation samples, and the addition of seasonality. The John Hopkins University spectral reflectance library was an invaluable resource to this study, and has a large number of soil samples compared to relatively few vegetation samples. A spectral library with a large sampling of different types of vegetation, in both lush and senescent stages would give a better representation of the true infrared emissivity. To add seasonality to the infrared emissivity atlas Francis (2003) has used greenness parameters retrieved by the Advanced Very High Resolution Radiometer (AVHRR). A five-year climatology was built that documented the ranges of greenness. The current vegetative greenness state is used with the greenness range to determine how to blend lush and senescent vegetation samples from the spectral library. The infrared land emissivity atlas would also allow for improved cloud detection. A clear sky background infrared radiance can be modeled using the atlas and profiles of temperature and moisture, allowing for an improved cloud detection capability.

Azimuthal effects of emissivity over high terrain have not been shown to have a large impact over the CONUS domain at one-half degree scales. These effects are significant in regions such as the Himalayas and can be seen in loops of microwave imagery. Polarization differences from brightness temperatures over land are more stable than the brightness temperatures themselves. Loops of these polarization differences over the Himalayas reveal a contrast between ascending and descending passes. These are due to changes in the effective emissivity from the satellite field of view. Retrievals of emissivity over these complex terrain regimes can be used to understand changes in emissivity due to angle of incidence or the effective emitting surface due to blocking effects.

Eventually clouds will need to be added into the procedure. Rayleigh or small droplet clouds are the simplest (when void of any precipitation), these clouds do not effectively scatter microwave radiation, and still contain considerable signal from the surface. A more complex cloud identification scheme will need to be implemented to discriminate between the small droplet cloud and more complex cloud. The more complex clouds (precipitating and multi-layered) are increasingly difficult because there is rarely an accurate first guess, and their radiative signatures often are not unique. It is common that many combinations of complex clouds can produce the same radiative signature. To begin the small droplet clouds will have to be identified, and then cloud liquid water retrievals can be performed for these clouds.

Lower frequencies in the microwave (10 GHz or less) have weakly scattering vegetation layers, and low atmospheric attenuations. These can be used in models containing canopy properties, such as transmissivity and single scattering albedo to more effectively retrieve soil wetness. The Advanced Microwave Scanning Radiometer (AMSR) contains channels at 6.9 and 10.7 GHz, and currently flies aboard the NASA Aqua satellite. The TMI instrument with a 10.65 GHz channel has been flying since 1997, but has not been widely utilized for soil moisture research. Precipitation affects properties in both the vegetative canopy and the soil surface. Preliminary work was performed with 2 km daily rainfall summaries, and the directly retrieved emissivities. The 19 GHz emissivities over bare ground were found to have weak correlations to rainfall, less than –0.4, which maximized at 1-day lag. A higher time resolution rainfall data set would enhance these correlations, and lower frequencies would have a greater sensitivity to the soil surface. If both of these data are acquired more robust vegetation correlations could be established.

When clouds and/or precipitation obscure the surface, the microwave emissivity estimates will need to be maintained in a weather model. A persistence model, which drifts from the last good retrieval toward climatology, could give microwave emissivity estimates, but preferably an accurate microwave emissivity model would be used. These models need to be tested in an operational framework to see how close the microwave emissivity estimates are after a cloudy episode has passed. The forward models rely on empirical relations to relate surface reflectance to surface roughness parameters. These relations will likely have trouble in complex terrain regimes with greatly varying angles of incidence. Validation and calibration of these models using observationally retrieved emissivities will help these models to develop the natural variability necessary for improved use of satellite microwave data over land.

The correlations and covariances computed in this study may be immediately applicable to new sensors such as the Special Sensor Microwave Imager/Sounder (SSM/IS), and future sounders such as the Conical Microwave Imager Sounder (CMIS). The similarity of viewing geometry and frequency of channels on the SSM/IS and CMIS satellites allow for direct implementation of many of the correlations found in this study. In addition, a forward Microwave Emissivity Model (MEM) can relate the retrieved correlations to other frequencies and scan angles not on current satellites. Validation of an MEM over a large domain and time frame will give an idea of the accuracy of the MEM for different locations and situations. The ability of the MEM to simulate the emissivity for any frequency and any scan angle will allow a researcher to build correlations of retrieved emissivities to psuedo-channels on upcoming sensors to prepare for their launch and use.

7. References

Ackerman, S., Strabala, K., Menzel, P., Frey, R., Moeller, C., Gumley, L., Baum, B., Seeman, S. and H. Zhang, 2002: Discriminating Clear-Sky from Cloud with MODIS: Algorithm Theoretical Basis Document (MOD35) version 4.0. *University of Wisconsin at Madison.*

Alishouse, J., S. Snyder, J. Vongsathorn, and R. Ferraro, 1990a: Determination of oceanic total precipitable water from the SSM/I. *IEEE Trans. Geosci. Remote Sens.*, **28**, 811-816.

——, J., Snider, E. Westwater, C. Swift, C. Ruf, S. Snyder, J. Vongsathorn, and R. Ferraro, 1990b: Determination of cloud liquid water content using the SSM/I. *IEEE Trans. Geosci. Remote Sens.*, **28**, 817-822.

Baker, N.L., R. Daley, S. Swadley, J. Clark, E. Barker, J. Goerss, K. Sashegyi, 2001: The Assimilation of satellite observations with the NRL Atmospheric Variational Data Assimilation System (NAVDAS). Preprints, *11th Conference on Satellite Meteorology and Oceanography*, Madison, WI, 279-281.

Basist, A., N. Grody, T. Peterson, and C. Williams, 1998: Using the SSM/I to monitor land surface temperatures, snow wetness, and snow cover. *Journal of Applied Meteorology*, **37**, 888-911.

Bauer, P., and N. Grody, 1995: The potential of combining SSM/I and SSM/T2 measurements to improve the identification of snowcover and precipitation. *IEEE Trans. Geosci. Remote Sens.*, **33**, 252-261.

Benjamin, S.G., Brundage, K.J., and L.L. Morone, 1994: The Rapid Update Cycle. Part I: Analysis/model description. *NWS Technical Procedures Bulletin*, No. 416., NOAA/NWS, 16pp.

Benjamin, S. G., J. M. Brown, K.J. Brundage, B. E. Schwartz, T.G. Smirnova, T.L. Smith, and L. L. Morone, 1998: RUC-2 The Rapid Update Cycle Version 2. *NWS Technical Procedure Bulletin*, No. 448. NOAA/NWS, 18pp.

Benjamin, S.G., D. Devenyi, S. Weygandt, K.J. Brundage, J.M. Brown, G. Grell, D. Kim, B.E. Schwartz, T.G. Smirnova, and T.L. Smith: An Hourly Assimilation/Forecast Cycle: The RUC. *Monthly Weather Review (submitted 13 March 2003).*

Choudhury, B. J., T. Schmugge, A. Chang, and R. Newton, 1979: Effect of surface roughness on the microwave emission from soils. *J. Geophysical Res.*, **84**, 5699-5706.

——, and R. E. Golus, 1988: Estimating soil wetness using satellite data. *Int. J. Remote Sensing*, **9**, 1251 – 1257.

Cooper, S. J., T. S. L'Ecuyer, and G. L. Stephens, 2003: The impact of explicit cloud boundary information on ice cloud microphysical property retrievals from infrared radiances. *J. Geosphysical Res.*, **108-D3**, Citation No. 4107, 17pp.

Daley, R., and E. Barker, 2001: NAVDAS: Formulation and diagnostics. *Mon. Wea. Rev.*, **129**, 869-883.

——, R. and E. Barker, 2001: NAVDAS Source Book 2001. NRL/PU/7530, 01-441. 161 pp. *Available from the Naval Research Laboratory, Monterey, CA 93943-5502.*

Felde, G., and J. Pickle, 1995: Retrieval of 91 and 150 GHz Earth suface emissivities. *Journal of Geophysical Research*, **100**, 20855-20866.

Ferraro, R., F. Weng, N. Grody, and A. Basist, 1996. An eight year (1987-1994) Time Series of Rainfall, clouds, water vapor, snow cover, and sea ice derived from SSM/I measurements. *Bulletin of the American Meteorological Society*, **77**, 891-905.

Francis, P. N., 2003: The Development of an IR land surface emissivity atlas, and its comparison with MODIS/TERRA products. UK-Met Forecasting Research Tech. Report *2003-no.405,* 50pp.

Greenwald, T., G. Stephens, T. Vonder Haar, and D. Jackson, 1993: A physical retrieval of cloud liquid water over the global oceans using Special Sensor Microwave/Imager (SSM/I) observations. *Journal of Geophysical Research*, **98**, 18471-18488.

Greenwald, T., C. Combs, A. Jones, D. Randel, and T. Vonder Haar, 1999: Error estimates of spaceborne passive microwave retrievals of cloud liquid water over land. *IEEE Trans. On Geosci. and Remote Sens.*, **37**, 796-804.

Grody, N. C., 1976: remote Sensing of Atmospheric Water Contents from satellites using Microwave Radiometry. *IEEE Trans. Antennas Propag.* **AP-24**, 155-162.

Grody, N, J. Zhao, R. Ferraro, F. Weng, and R. Boers, 2001: Determination of precipitable water and cloud liquid water over oceans for the NOAA15 advanced microwave sounding unit. *Journal of Geophysical Research*, **106**, 2943-2953.

Hansen, M. C., R. S.DeFries, J. R. Townshend, and R. Sohlberg, 2000: Global land cover classification at 1km spatial resolution using a classification tree approach. *Int. J. Remote Sensing* **21**, No. 6 & 7, 1331-1364.

Hodur, R.M., 1997: The Naval Research Laboratory's Coupled Ocean/Atmosphere Mesoscale Prediction System (COAMPS). *Mon. Wea. Rev.*, **125**, 1414-1430.

Hollinger, J. P., 1971: Passive Microwave Measurements of Sea Surface Roughness. *IEEE Trans. On Geoscience Electronics*, **GE-9**, no. 3, pp. 165 – 169.

Hogan, T. F, and T. Rosmond, 1991: The Description of the Navy Operational Global Atmospheric Prediction System's Spectral Forecast Model. *Monthly Weather Review*, **119**, 1786-1815.

Hufford, G., and H. Liebe, 1989: MM-Wave Propagation in the Mesosphere. NTIA Report 89-249, 67p., (NTIS Order No.PB90-119868/AS).

Jedlovec, G., and K. Laws, 2003: GOES cloud detection at the Global Hydrology and Climate Center. *12th Conference on Satellite Meteorology and Oceanography*, AMS.

Jones, A, and T. H. Vonder Haar, 1997: Retrieval of microwave surface emittance over land using coincident microwave and infrared satellite measurements. *Journal of Geophysical Research*, **102**, 13609-13626.

Kidder, S., and T. Vonder Haar, 1995: Satellite Meteorology: An introduction. *Academic Press*, New York, NY, 466pp.

Kidwell, K, G. Goodrum, and W. Winston (Eds.), 2000: NOAA KLM User's Guide (available at http://www2.ncdc.noaa.gov/docs/klm/index.htm).

Kratz, D., 1995: The correlated k-distribution technique as applied to the AVHRR channels. *J. Quant. Spectrosc. Radiat. Transfer*, **53**, 501-517.

Lacis, A. A., W. C. Wang, and J. Hansen, 1979: *NASA Conf. Publ.*, **2076**, 309-314.

L'Ecuyer, T, and G. L. Stephens, 2001: An Estimation-Based Precipitation Retrieval Algorithm for Attenuating Radars. *Journal of Applied Meteorology*, **41**, 272-285.

Liebe, H., 1985: An updated model for millimeter-wave propagation in moist air. *Radio Science*, **20**, no. 5, pp. 1069-1089.

——, H., 1987: A contribution to modeling atmospheric mm-wave properties. FREQUENZ, **41**, no. 1/2, pp. 31-36.

——, H., and D. Layton, 1987: MM-wave Properties of the Atmosphere: Laboratory Studies and Propagation Modeling. NTIA Report 87-224, 80p., (NTIS Order No. PB88-164215/AF).

——, H., 1989: MPM89 - An atmospheric mm-wave propagation model. *Int. J. IR & MM Waves*, **10**, no.6, pp. 631-650.

——, H. , and T. Manabe, and G. Hufford, 1989: Mm-wave attenuation and delay rates due to fog/cloud conditions", *IEEE Trans. Ant. Prop.*, **37**, no. 12, pp. 1617-1623.

——, H., G. Hufford (ice), and T. Manabe, 1991: A model for the complex refractivity of water (ice) at frequencies below 1 THz. *Int. J. IR & MM Waves*, **12**, no. 7, 659-682.

——, H., P. Rosenkranz, and G. Hufford, 1992: Atmospheric 60-GHzoxygen spectrum: New laboratory measurements and line parameters. *J. Quant. Spectr. Rad. Transf.*, **48**, no. 5/6, pp. 629-643.

——, H. , G. Hufford, and M. Cotton, 1993: Propagation modeling of moist air and suspended water/ice particles at frequencies below 1000 GHz. Proc. AGARD Conf. Paper 3/1-10, Palma De Mallorca, Spain.

Liou, K. N., 1980: An Introduction to Atmospheric Radiation. *Academic Press Inc.*, New York, NY, 362pp.

Liou, K. N., 1992: Radiation and Cloud Processes in the Atmosphere. *Oxford University Press*, New York, NY, 487pp.

Ma, X. L., Z. Wan, C. C. Moeller, W. P. Menzel, and L. E. Gumley, 2002: Simultaneous retrieval of atmospheric profiles and land-surface temperature, and surface emissivity from Moderate Resolution Imaging Spectroradiometer thermal infrared data: extension of a two-step physical algorithm. *Applied Optics*, **41**, No. 20, 909-924.

Miller, D. A., and R. A. White, 1998: A Conterminous United States Multilayer Soil Characteristics Dataset for Regional Climate and Hydrology Modeling. *Earth Interactions*, **2**, no. 2, 26pp.

Neale, C., M. McFarland, and K. Chang, 1990: Land-surface-type classification using microwave brightness temperatures from the SSM/I. *IEEE Trans. Geosci. Remote Sens.*, **28**, 829-838.

Njoku, E. G., and P. E. O'Neill, 1982: Multifrequency microwave radiometer measurements of soil moisture. *IEEE Trans. Geosci. Remote Sens.*, **GE-20**, 468-475.

Planck, M., 1900: On an improvement of Wien's equation for the spectrum *Verhandl. Dtsch. Phys. Ges.*, **2**, 1 – 3.

Prigent, C., W. Rossow, and E. Matthews, 1997: Microwave land surface emissivities estimated from SSM/I observations. *Journal of Geophysical Research*, **102**, 21867-21890.

Roberts, R. E., Selby, J. E., and L. M. Biberman, 1976: Infrared continuum absorption by atmospheric water vapor in the 8-12 micron window. *Appl. Opt.*, **15**, 2085-2090.

Rodgers, C. D., 1976: Retrieval of Atmospheric Temperature and Composition from Remote Measurements of Thermal Radiation. *Reviews on Geophysics and Space Physics*, **14**, 609-624.

Rodgers, C. D., 2000: Inverse Methods for atmospheric sounding. *World Scientific Publishing*, River Edge, NJ. 238pp.

Rossow, W.B., and L.C. Garder, 1993: Cloud Detection Using Satellite Measurements of Infrared and Visible Radiances for ISCCP. *Journal of Climate*, **6**, 2341-2369.

Salisbury, J. W, and D. M. D'Aria, 1992: Emissivity of Terrestrial materials in the 8-14 μm atmospheric window. *Remote Sens. Environ.*, 42, 83-106.

Schmidt, U., and A. Khedim, 1991: In situ measurements of carbon dioxide in the winter arctic vortex and at midlatitudes: an indicator of the age of stratospheric air. *Geophysical Research Letters*, **18**, 763-766.

Schmugge, T., P. E. O'Neill, and J. R. Wang, 1986: Passive microwave soil moisture research. *IEEE Trans. Geosci. Remote Sens.*, **GE-24 no. 1**, 12-22.

Snyder, W. C, Z. Wan, Y. Zhang, and Y.Z. Feng, 1998: Classification-based emissivity for land surface temperature measurement from space. *Int. J. Remote Sensing*, **19** no. 14, 2753 – 2774.

Staelin, D. H., Kunzi, K. F., Pettyjohn, R. L., Poon, R.K.L., and R. W. Wilcox, 1976: Remote sensing of Atmospheric Water Vapor and Liquid Water with the Nimbus 5 Microwave Spectrometer. *J. Appl. Meteorol.* **15**, 1204-1214.

Stephens, G. L., 1994: Remote Sensing of the Lower Atmosphere: An Introduction. *Oxford University Press, New York, NY.* 523pp.

Stogryn, A., 1967: The Apparent Temperature of the Sea at Microwave Frequencies. *IEEE Trans. On Antennas and Propagation*, **AP-15**, no. 2, pp. 278-286.

Tjemkes, S. A., G. L. Stephens, and D. L. Jackson, 1991: Spaceborne observation of columnar water vapor: SSM/I observations and algorithm. *Journal of Geophysical Research*, **96**, 10941-10954.

Ulaby, F. T, and E. A. Wilson, 1985: Microwave attenuation properties of vegetation canopies. *IEEE Trans. Geosci. Remote Sens.*, **GE-23**, 746-753.

——, R. K. Moore, and A. K. Fung, 1986: Microwave remote sensing, active and passive, vol. III: From theory to applications. *Artech House, Massachusetts.*

Wan, Z., and J. Dozier, 1996: A Generalized split-window algorithm for retrieving land-surface temperature from space. *IEEE Trans. Geosci. and Remote Sens.*, **34**, 892-905.

——, Z. and Z. L. Li, 1997: A physics-based algorithm for retrieving land surface emissivity and temperature from EOS/MODIS data. *IEEE Trans. Geosci. and Remote Sens.*, **35**(4), 980-996.

——, 1999: MODIS land-surface temperature algorithm theoretical basis document (LST ATBD) version 3.3. *University of California at Santa Barbara.*

——, Y. Zhang, Q. Zhang, and Z. Li, 2002: Validation of land-surface temperature products retrieved from terra moderate resolution imaging spectroradiometer data. *Remote Sensing of Environment*, **83**, 163-180.

Wang, J. R., and T. J. Schmugge, 1980: An empirical model for the complex dielectric permittivity of soils as a function of water content. *IEEE Trans. Geosci. Remote Sens.*, **GE-18**, 288-295.

Weinreb, M.P.,M. Jamison, N. Fulton, Y. Chen, J.X. Johnson, J. Bremer, C. Smith, and J. Baucom, 1997: Operational calibration of Geostationary Operational Environmental Satellite-8 and -9 imagers and sounders. *Applied Optics, **36**,* pp 6895-6904.

Weng, R. Ferraro, and N. Grody, 1994: Global precipitation estimations using Defense Meteorological Satellite Program F10 and F11 special sensor microwave imager data. *Journal of Geophysical Research*, **99**, 14493-14502.

——, F., N. Grody, R. Ferraro, A. Basist, and D. Forsyth, 1997: Cloud liquid water climatology from the Special Sensor Microwave/Imager. *Journal of Climate*, **10**, 1086-1098.

——, F., and N. Grody, 1998: Physical retrieval of land surface temperature using the special sensor microwave imager. *Journal of Geophysical Research*, **103**, 8839-8848.

——, F., and N. Grody, 2001: A microwave land emissivity model. *Journal of Geophysical Research*, **106**, 20115-20123.

Wentz, F. J., 1988: *User's Manual SSM/I Antenna Temperature Tapes.* Remote sensing Systems Technical Report 032588, 1101 College Ave., Suite 220, Santa Rosa, CA, 22pp.

Wilber, A. C., D. P. Kratz, and S. K. Gupta, 1999: Surface Emissivity Maps for Use in Satellite Retrievals of Longwave Radiation. *NASA/TP-1999-209362*, 35pp.

Williams, C., A. Basist, T. Peterson, and N. Grody, 2000: Calibration and verification of land surface temperature anomalies derived from the SSM/I. *Bulletin of the American Meteorological Society*, **81**, 2141-2156.